Institut für Physik der Universität Basel

UNI
BASEL

Test and Evaluation of Silicon as Sensor Material for the CMS Pixel detector

Basel, June 1999

Test and Evaluation of Silicon as Sensor Material for the CMS Pixel detector

Inauguraldissertation
zur
Erlangung der Würde eines Doktors der Philosophie

vorgelegt der

Philosophisch-Naturwissenschaftlichen Fakultät
der Universität Basel

von
Beat Henrich
aus Allschwil

Basel im Juni 1999

Genehmigt von der Philosophisch-Naturwissenschaftlichen Fakultät auf Antrag der Herren Professor Dr. Ludwig Tauscher und Dr. Roland Horisberger

Basel, den 8.6.1999

Prof. Dr. Stefan M. Schmid
Dekan

To
Katharina, Sirkka and Mirja

For we are the local embodiment of a cosmos grown to self-awareness. We have begun to contemplate our origins, starstuff pondering the stars; organized assemblages of 10^{18} atoms considering the evolution of atoms; tracing the long journey by which, here [on earth] at last, consciousness arose.

Carl Sagan
Cosmos 1981

ABSTRACT

For several years semiconductor detectors have been appreciated as tools not only for optical applications but also for the measurement of nuclear radiation. The interest in these detectors is still rising and two main reasons explain this development. Semiconductor materials have striking properties which make them very useful for fast and precise position and energy measurement. On the other hand new technologies and new ideas for detector concepts open a wide range of practical applications.

Silicon detectors play a leading role as position sensitive sensor material for high energy physics applications. They were involved in many discoveries made in recent experiments such as the discovery of the top quark. For future collider experiments they have become indispensable. ATLAS and CMS, the two multipurpose experiments at LHC will use huge numbers of silicon as tracker devices.

Because of their high spatial resolution and their low occupancies, pixel detectors are the ideal devices to be operated close to the interaction point. The high particle fluxes in this region cause severe radiation damage degrading the detector performance which has implication on both, the sensor material and the readout electronics.

Because of the growing number of pixels with increasing sensitive area this sensor concept is not suited for large scale application. Therefore, the outer tracking radii are equipped with silicon micro strip detectors.

The greatest challenge in the design of the pixel detector system is the radiation hardness of all components and the extremely large number of pixels (3.5×10^7) to be handled in a high rate environment. Sensor and readout chips must be robust enough to endure the first six years of LHC operation without inacceptable degradation of their performance.

This work presents measurements on a prototype sensor with an array of 8×32 pixels. A newly developed method capable to determine the space charge region of partial depleted sensors is introduced. This method uses minimum ionising particles transversing the sensor under a shallow angle. The grazing particles probe the sensor at certain depths and allow the measurement of the depletion depth profile based on simple geometric calculations.

The pixel sensor prototypes were irradiated with fluences of 1.4, 6.3 and $9\times10^{14}/\text{cm}^2$ which are the doses anticipated for the different layers of the silicon pixel detector. Pions were used since they represent the biggest portion of ionising radiation near the interaction point of CMS. Afterwards they were periodically tested using the grazing angle method to investigate the annealing behaviour. The conditions under which the sensors are stored agree with the temperature environment met at LHC.

For better understanding of the experimental data a numerical simulation was created including the models which are identified to cause this behaviour. These generated events show good accordance with the experimentally observed effects.

Both, experiment and simulation have contributed to a better understanding of effects which occur in silicon under radiation. Although this thesis was elaborated in the context of an application for high energy physics experiments its results are also considerable for solid state physics and their applications.

ZUSAMMENFASSUNG

Halbleiter werden vermehrt nicht nur zu optischen Zwecken sondern auch zum Nachweis nuklearer Strahlung eingesetzt. Dabei liegt der Grund für das stetig wachsende Interesse an solchen Sensoren in der hohen Geschwindigkeit mit der das Signal bei den Ausleseverstärkern anliegt und in der hohen Ortsauflösung. Zudem ergänzen und erweitern laufend neue Ideen und Detektorkonzepte das Spektrum der Anwendungen.

Silizium übenimmt dabei als Sensor zur Ortsbestimmung in Hochenergie Physik Experimenten eine Führungsrolle. An Entdeckungen wie der des Top-Quark waren sie massgeblich beteiligt und sind daher aus neu geplanten Hochenergie Experimenten kaum noch wegzudenken.

Die beiden grossen Experimente ATLAS und CMS planen den Einsatz solcher Detektoren im grossen Stil. Silizium Mikrostreifen Detektoren decken dabei Regionen mit mittlerem Abstand zum Wechselwirkungspunkt ab während Pixel Detektoren idealerweise in Regionen mit hoher Teilchendichte eingesetzt werden.

Aufgrund der hohen Ortsauflösung und der niedrigen Totzeit, eignen sich Pixel Detektoren besonders für einen Einsatz nahe dem Kollisionspunkt. Der allerdings in diesem Bereich hohe Anteil an ionisierenden Teilchen führt zu starker Strahlenbelastung. Diese hat wiederum Leistungseinbussen sowohl bei den Sensoren als auch in der Ausleseelektronik zur Folge.

Da sich die bildpunktartigen Pixel Detektoren kaum zur Abdeckung grosser Flächen eignen werden sie zu grösseren Radien hin von Silizium Mikrostreifen Detektoren abgelöst. Die grösste Herausforderung für ein Pixel Detektor System liegt jedoch in der ausserordentlich hohen Strahlenbelastung mit der sowohl der Sensor wie auch die Ausleseelektonik verträglich sein müssen.

Anvisiert ist ein dauerhafter Betrieb von bis zu sechs Jahren wobei besonders für die innerste Lage bei einem Radius von 4.5 cm damit gerechnet wird, dass die von LHC angestrebte Luminosität von $10^{34}\text{cm}^{-2}\text{s}^{-1}$ erst nach 2-3 Jahren erreicht sein wird. Dies hat eine etwas niedrigere Strahlenbelastung als zunächst angenommen zur Folge.

Im Rahmen dieser Arbeit werden Messungen an Pixel Sensor Prototypen vorgestellt, die mit unterschiedlichen Dosisleistungen ionisierender Teilchen bestrahlt wurden. Die hier beschriebene und neu entwickelte Methode ermöglicht eine gezielte Untersuchung von unvollständig oder nur teilweise depletierten Sensoren. Dies geschieht mittels minimal ionosierenden Teilchen, die unter einem sehr flachen Winkel den Sensor durchqueren. Die erzeugten Ladungsträger enthalten wichtige Informationen über den Zustand ihres Entstehungsortes. Auf diese Weise kann ein sogenanntes Depletionstiefen Profil des Sensors erstellt werden.

Die Höhe der verschiedenen Dosisleistungen von 1.4, 6.3 und 9×10^{14}pionen/cm^2 entsprechen der aufgenommenen Dosis die sich im Laufe eines sechsjährigen Betriebs bei LHC in den verschiedenen Abständen zum Wechselwirkungspunkt aufakkumulieren.

Nach Bestrahlung werden die Prototypen in periodischer Folge einem Langzeittest unterzogen wobei der Ausheilungsprozess das sogenannte Annealing unter LHC treuen Bedingungen untersucht wird.

Zusätzlich wurde zum besseren Verständnis der experimentellen Beobachtung eine numerische Simulation entwickelt die das Experiment nachstellt. Die verwendeten Modelle zur Beschreibung der einzelnen Beobachtungen haben sich bei direktem Vergleich mit dem Experiment bestätigt.

Sowohl das Experiment als auch die detailierte Simulation haben einen wesentlichen Beitrag zum besseren Verständnis von Strahlenschäden in Silizium geleistet. Obwohl sich diese Arbeit an einer speziellen Anwendung in der Hochenergiepysik orientiert, lassen sich die Ergebnisse durchaus in die Gebiete der Festkörper Forschung übertragen. Sie tragen auch dazu bei, die fundierten Kentnisse über die Vorgänge in Halbleitern zu erweitern.

CONTENTS

1 INTRODUCTION

The study of the very nature of elementary particles and forces is presently pursued at LEP (CERN), Tevatron (Fermilab), SLC (SLAC), HERA (Desy) and various lower energy facilities in operation or under construction. While these studies confirm the Standard Model (SM) with increasing precision, the windows to newer physics and for the discovery of the Higgs boson remain narrow. New facilities are necessary in order to explore physics at a higher man scale.

Therefore, CERN has decided to build the Large Hadron Collider (LHC). This project was approved by CERN in 1994 and the machine will bring protons into head-on collisions at a centre-of-mass energy of 14 TeV with a luminosity of 10^{34} cm^2s^{-1}. It will allow scientists to penetrate into the structure of matter and recreate the conditions prevailing in the universe just 10^{-12} seconds after the Big Bang when the temperature was 10^{16} degrees.

Tracking detectors employed in experiments at the LHC will have to meet tremendous requirements. On the one hand it is called for highest precision in tracking information, on the other hand an immense event rate (40 MHz or one bunch crossing each 25 ns) demands for a fast signal processing. In complete contrast to these requirements detectors and electronics are under permanent particle bombardment which causes severe radiation damage leading to constant degradation of the performance.

1.1 Outline and structure

In order to keep costs low it is required that the CMS pixel detector has to endure an operational time of at least six years and survives fluences of up to 6×10^{14} hadrons per cm^2 ($\sim$20 Mrad)[1] providing sufficient signal charge throughout this period. At the time of the CMS Technical Proposal the level of knowledge proposed three candidates which promised sufficient radiation hardness: Gallium-arsenide, diamond and silicon. This work will present a detailed investigation of silicon as suitable sensor material for the CMS-pixel detector. It is also a useful contribution to a better understanding and characterisation of radiation induced effects in semiconductors.

In parallel, other groups ([1] and [2]) worked on the materials mentioned in order to investigate the same requirements. The most suitable and viable candidate will be the baseline material for the CMS-pixel detector.

This work is structured in nine sections:

Part one (section 2) debates the necessity for a pixel detector and its technical realisation within the CMS experiment. Section 3 gives a formal introduction of important detector properties and the change of parameters due to radiation induced damage. The design of irradiation test structures and the discussion of the layout concept is the content of section 4. The next part (see section 5) introduces the grazing angle method and discusses the advantages over conventional measurement methods. This is followed by section 6 where the experimental results are presented. Understandably it is not possible to carry out tests which are completely identical to LHC conditions. But the exterior conditions under which the detectors are kept during the tests are in agreement with the situation at LHC. All important and required measurements such as leakage current, depletion depth and charge collection efficiency are subject of this long term study.

In section 7 numerical studies are performed which aim at understanding the observed effects. Section 8 directly refers to section 6. Important results and consequences as an output of the simulation are shown and compared to the experimental outcome. Concluding remarks and a compilation of the results of this study are given in section 9. Here possible extensions of the present work are discussed.

1.2 Historical motivation

Decades of intense experimental and theoretical efforts have provided knowledge about the constituents of matter and the forces acting between them. Electric and magnetic forces were understood to be of the same origin and described by the classical electromagnetic theory in the

1. This is the expected fluence anticipated in the first six years of LHC at a radius of 7cm

nineteenth century. The success of quantum electrodynamics and its formulation in the language of the locally gauge invariant field theory in the end of 1940's inspired theorists to describe the weak forces with the same method. This led to the spectacularly successful electroweak theory. Here, the forces and their mediators, a massless photon and massive Z and W bosons look very different. The differences in masses were explained by the spontaneous symmetry breaking which leads to a unification of these two forces. Adding the third group of fundamental processes, the strong interaction of quarks and gluons described by the gauge theory of quantum chromodynamics, we have the Standard Model description of fundamental particles and interactions.

This consistent model was confirmed with high precision by many experiments, and no deviations from its predictions were found so far. The search for the Higgs, the only empirically missing entry of the Standard Model, is therefore the main task for future collider experiments such as the Compact Muon Solenoid (CMS) aiming at a deeper level of understanding for the physics described by the Standard Model.

The Standard Model:

Matter is made of quarks and leptons. These constituents are arranged in three families of quarks and leptons with a light neutrino. Our world is constructed from the constituents of the first family, the up- and the down-quarks, the electron, and the electron neutrino and their anti-particles. Knowledge of the two other families (s-quark, c-quark, muon and muon neutrino...) stems from cosmic ray and, in particular, from accelerator-based research. The existence of the heaviest quark, the top-quark has recently been proved in experiments carried out at Fermilab, which operates to date the most energetic particle collider [3] in the world. Based on cosmological evidence on helium abundance, and, more significantly, on precision measurements at the Large Electron Positron (LEP) collider at CERN and the SLAC Linear Collider (SLC) at Stanford, indicate that there are only three light neutrino species and hence only three families of constituents.

In parallel, the theoretical framework which describes the interactions between these particles, was constructed. The Standard Model of the strong and electroweak interactions has been confronted with experiments in atomic, nuclear and particle physics. Many measurements yield an accuracy of $\sim 0.1\%$.

The principle of gauge invariance has been the guide to the discovery of the SM. This principle can be considered as a generalisation of gauge invariance in classical electrodynamics and of the phase invariance of a quantum mechanical wave function $\Psi \rightarrow \Psi' = e^{-i\alpha}\Psi$. It is an invariance under transformations in an internal space, in which particles carry quantum numbers (e.g. spin, colour,...) specific to this space. Requiring invariance generates associated fields (gauge fields) and particles (gauge bosons). The set of these transformations forms a group of quantum numbers associated with the specific interaction. The appropriate internal symmetries have been identified and are the foundation of the Standard Model: a unitary group U(1) is related to the electro magnetic interaction, the special unitary group SU(2) describes the electroweak force, and a third, SU(3) symmetry is associated with the strong interaction. The Lagrangian of the SM has a SU(3)×SU(2)×U(1) symmetry [4].

However, these symmetry properties represent only the first element of the correct description. From experiment we know that this symmetry is not exact but broken: quarks and leptons have different masses. Within the frame work of the SM a technical solution has been devised (Weinberg-Salam-Glashow theory) to generate the masses of the bosons. This mechanism produces correct results, although a fundamental understanding or justification is lacking. A new scalar field is introduced, which is assured to permeate the vacuum. Its interaction with particles generates the masses dynamically.

The ground state of the vacuum gets a non-zero field value $\phi = v \cdot e^{i\varphi}$ and a vacuum expectation value v. Physically, the vacuum has to have a unique value with a specific value of phase which cannot be chosen arbitrarily at each space-time point: a non-zero expectation value breaks the local gauge invariance.

Nature shows other examples of broken symmetries. Super conductivity is a famous one, to which this concept was first applied [5]. It guided particle physicists such as P. Higgs and others [6] and has become known as the *Higgs mechanism* in the Standard Model. It is this new interaction between the (coherent) system of scalar fields ϕ with the gauge bosons and fermions that gives rise to effective particle masses. This interaction is proportional to $\langle\phi\rangle$ and to the coupling constants. It relates therefore, e.g., the masses of the W and Z bosons to the electroweak mixing angle θ_W: $M_W = M_Z \; cos \; \theta_W$, a relation which is experimentally confirmed.

The Higgs mechanism has an other observable consequence which would manifest by the existence of at least one neutral scalar particle, the Higgs boson, of unknown mass which has to be larger than 65 GeV/c^2 [7].

To date the SM provides a useful description of the observable high energy physics. But no answers are provided to many fundamental questions such as:

- Why are there three generations of quarks and leptons?
- What is the purpose of three independent symmetry groups?
- How can gravity be included?

It is the aim of the LHC programme to address these questions.

2 LHC AND THE CMS EXPERIMENT

The LHC is in preparation at CERN. Proton-proton collisions at energies of up to 14 TeV will probe the laws of the fundamental interactions at effective energies of 1 TeV or higher. At these energies, the Standard Model predicts the observation of new experimental signatures. It is not excluded that new observations with the LHC will lead towards a more global theory.

Already in the early planning of the Large Electron Positron collider (LEP) it was recognised that the large, circular tunnel might house a new machine at a later stage. A super-conducting, high-energy proton collider was discussed as a rational research tool to follow the LEP era [8].

Ten years later, the LHC has been approved as the next machine, enlarging the synergetic network of CERN machines (figure 1). The existing facilities provide the basis for a diverse physics programme, catering the research interests of approximately 5000 physicists. Different particles are available, accelerated to a wide spectrum of energies. Protons and anti-protons as low as a few MeV are used at LEAR; hadron and lepton beams in the 100 to few hundred GeV range are produced in the SPS; LEP operates at $\sqrt{s} \approx 90$ GeV, increasing to ≈ 180 GeV; heavy-ion beams with a total energy up to 30 TeV have recently been obtained.

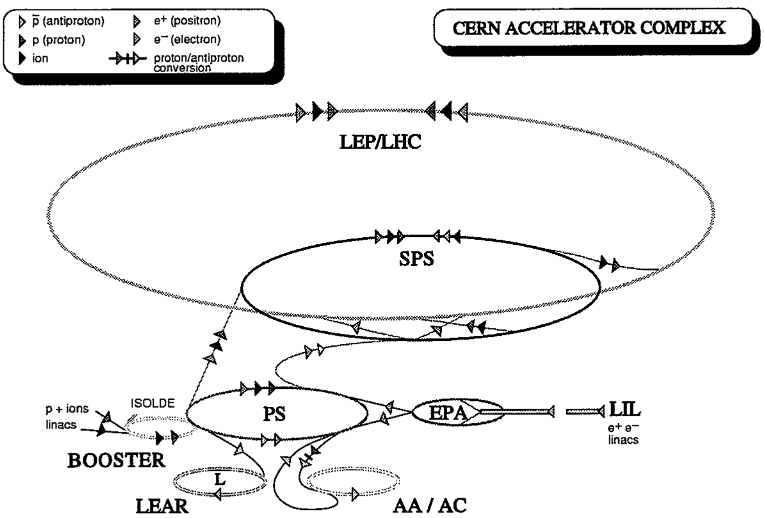

Figure 1: The CERN network of interlinked accelerators and colliders, providing the basis for a very diverse research programme and for a cost-effective addition of the LHC machine.

The LHC machine parameters

Within the available tunnel of 26.7 km circumference, two thirds can be effectively filled with the magnetic guiding fields. The achievable beam momenta are p [TeV/c] $\sim$ 0.83 B [T]. Superconducting magnets with fields $B \sim 8.3$ T are therefore necessary to reach the target of $\sqrt{s} \sim 14$ TeV. The main parameters of the LHC machine are summarised in table 1. The LHC magnet systems represents one of the largest applications of super-conductivity. A total of 1250 dipole magnets, each 14.2 m long and 400 quadrupoles, each 3 m long, will be distributed around the 26.7 km long tunnel. A large number of additional magnets (correctors, low-β insertions,...) will be required, raising the total number of super-conducting magnets to approximately 10'000!

2.1 The CMS experiment

The CMS detector has been designed to detect the diverse signatures of new physics at the Large Hadron Collider. It will do so by identifying and precisely measuring positions and energies of muons, electrons, and jets over a large energy range. Experience has shown that robust tracking and detailed vertex reconstruction within a strong magnetic field are powerful tools to reach these objectives. The detector described maintains the design goals defined in 1992 in the Evian meeting [9].

Already the name of the experiment expresses the concern about muon spectroscopy. This

Parameters	pp	Pb Ions
Operational energy [TeV]	14	1148
Dipole field (operating) [T]	8.4	8.4
Luminosity [$cm^{-2}s^{-1}$]	10^{34}	10^{27}
Bunch interval [m/ns]	7.5/25	40.5/135
Particles per bunch	10^{11}	10^{8}
Particles per beam	4.7×10^{14}	4.7×10^{8}
Number of experiments	2	1

Table 1: Main LHC parameters for pp and Pb Ion collision.

emphasis has its reason in the muon itself which only loses energy by electromagnetic interaction with matter. Therefore such particles are conveniently identified behind massive absorbers. As a consequence **muon detection systems** (muon calorimeters) are arranged as the outermost detectors and dominate such an experimental apparatus in size and weight. In CMS the muon detector has to fulfil three basic tasks: muon identification, momentum measurement and trigger. It consists of four muon stations interleaved with the iron return yoke plates which serve as absorbers. The muon stations are based on a system of several hundred chambers of drift tubes which are aligned as concentric cylinders in the barrel region and as disks in the end cap regions.

The core of the CMS detector is a large **super-conducting solenoid** generating a uniform magnetic field of 4 Tesla. It has a length of 13 m and an inner diameter of 5.9 m. The magnetic flux is returned via a 1.8 m thick saturated iron yoke instrumented with muon stations. The choice of a strong magnetic field leads to a compact design for the muon spectrometer without compromising the momentum resolution up to rapidities of η =2.5. Here, η is the pseudorapidity which is defined as $\eta = -\ln\ \tan\ \vartheta/2$, where ϑ denotes the angle between the beam axis and the direction of the produced particle. It is often used in this context because it is a handy variable to approximate the rapidity if the mass and momentum of a particle are not known. The inner coil diameter is large enough to accommodate the tracker and the calorimeters. Simultaneously, the magnet is used as the principal structural element to support all other barrel detector components.

Hermetic **hadronic calorimeters** surround the intersection region up to $\mid \eta \mid$ = 4.7 allowing to tag forward jets and measurement of missing transverse energy. The primary task of the hadron calorimeter is to measure the energies of hadrons in jets, which occur in most decays of heavy particles. Such information is mainly important for Higgs searches and particle detection via missing energy. This detector consists of about 3'400 plastic scintillators between copper absorbers. The active area of one element is 0.087×0.087 (in radians). The expected energy resolution is $\sigma_E/E = 65\%/\sqrt{E} + 5\%$ [E in GeV].

A high resolution crystal **electro-magnetic calorimeter**, designed to detect the two photon decay of an intermediate mass Higgs, is located inside the coil. It allows precise energy and angular measurements of photons and electrons from reaction processes such as $H \rightarrow \gamma\gamma$ or $H \rightarrow ZZ \rightarrow 2e^+2e^-$ processes. A number of 109'008 tungstate lead crystals ($PbWO_4$) assure an angular resolution of $\sigma_\theta/E = 50mrad/\sqrt{E}$ [E in GeV]. The energy resolution resolution is expected to be $\sigma_E/E = 3.5\%/\sqrt{E} + 0.36\%$.

The **very forward calorimeter** covers the pseudorapidity range of $3.0 \leq \mid \eta \mid \leq 5.0$ and is located ± 11m from the interaction point. The study of longitudinal intermediate boson scattering will require the detection of forward or backward directed jets. This study will become very important if the SM Higgs does not exist or if it is extremely massive. Two options are considered, either parallel plates of gas chambers interleaved with iron absorbers or scintillating quartz fibres surrounded by iron or copper absorbers.

The inner **tracking system** is dedicated to measure all charged tracks with a momentum resolution of $\Delta p/p \approx 0.1\ p_T$ (p_T in TeV) in the range $\mid \eta \mid < 2.5$. Particles with high transverse momentum up to $p_T \approx 2$TeV (defined as $p_T = \sqrt{(p_x^2 + p_y^2)}$) are of special interest. Its subdetectors consist of several layers of micro strip gas chambers (MSCG's), silicon strip detectors and silicon pixel detectors. Each is composed of barrel regions and wheel shaped end cap regions. A more more detailed description is given in the following section.

Figure 2 gives a three dimensional view of the CMS detector and the positioning of the described detector components.

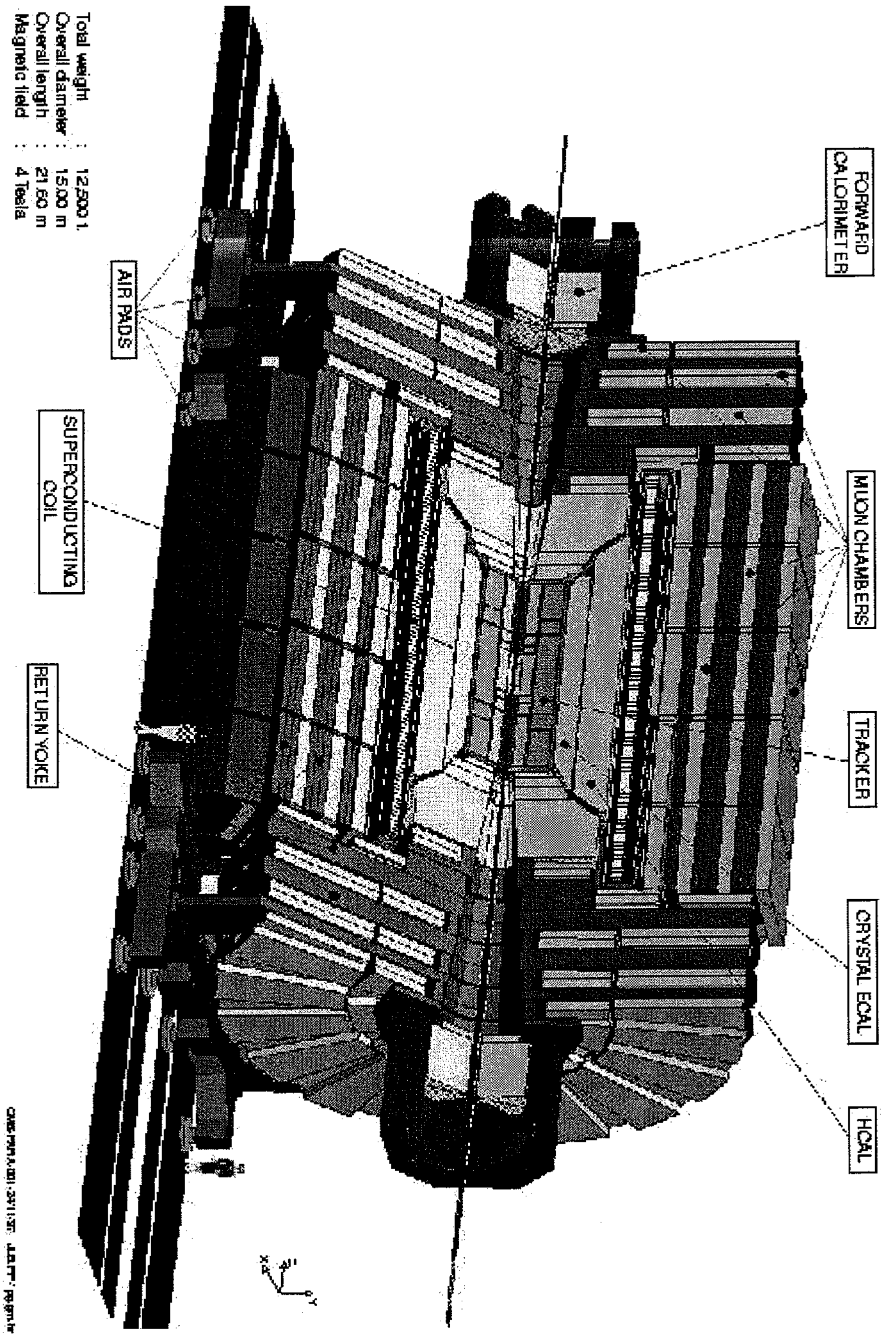

Figure 2: A three dimensional view into the CMS detector.

2.2 Physics objectives and the CMS tracker

Robust tracking and detailed vertex reconstruction play an essential role for an experiment designed to address the full range of physics which can be accessed at the LHC. Therefore the tracker must satisfy a number of performance requirements listed below.

The tracker should provide good momentum measurement for energetic leptons since these show clean experimental signals that indicate the decay of involved gauge bosons which, for their part, could originate in a Higgs boson. These measurements are combined with track segments reconstructed in the outer muon system to further extend the kinematic region. This will place stringent requirements on the alignment of the tracker relative to the muon chambers. For the same reason the multiple scattering due to leptonic bremsstrahlung must be kept to a minimum. This has consequences for the material involved such as the mechanical support, cooling and power supply. Therefore, the radiation length of the material used is an important selection criteria.

Efficient isolated lepton track reconstruction is the main task of the tracking detectors. Points measured close to the primary vertex significantly reduce the combinatorial background. For example it is required to suppress $t\bar{t}$ and $Zb\bar{b}$ backgrounds to a level which allows observation of $H \rightarrow ZZ^* \rightarrow 4l^{\pm}$ and $H \rightarrow ZZ \rightarrow 4l^{\pm}$ for the full theoretically predicted mass range between $120 \leq m_H \leq 800$ GeV.

The symmetries C (particle-antiparticle interchange) and P (space inversion) hold for strong and electromagnetic interactions. After the discovery of large C and P violation in the weak interaction, it appeared that the product CP was a conserved symmetry. In 1964 CP violation was observed in K^0 decays at a level given by the parameter $\epsilon \approx 2.3 \times 10^{-3}$. Larger CP-violation effects are anticipated in B^0 decays. Therefore, no less important than to suppress background is the ability to tag and reconstruct jets in detail, and identify hadrons (especially B-hadrons) within these jets. These will open a wide spectrum for new physics, as top quark physics and give new fundamental insight in CP violation. The ability to identify tracks originating from multiple vertices and the capability to reconstruct a variety of decay chains as well as the accurate determination of the time resolved B decay are required. The challenge lies in the measurement of the difference in selected decay rates of b- and $\bar{b}$-hadrons, which needs the identification of the initial flavour of the decaying hadron. In CMS, the most promising decay channels to detect and analyse are $B_d^0 \rightarrow J/\psi K_s^0$ and $B_d^0 \rightarrow \pi^+\pi^-$, which have small branching ratios but clean signatures. The decay asymmetry in the former decay is proportional to $\sin 2\beta$, while the latter comprise information on $\sin 2\alpha$ which are two angles from the unitary triangle. While α measures the direct CP-violation, in β the $B_d^0 - \bar{B}_d^0$ mixing is contained.

In addition, a broad channel of plausible new physics has to be included such as decay chains pertinent to a possible SUSY Higgs sector which would end in τ leptons.

The CMS tracker components

Silicon pixels are the ideal detectors to comply with the demands for the tracking device extending as close as possible to the interaction point. Due to the extremely high particle fluxes in this region only pixel sensor devices will deliver true space point information with high resolution. The pixel size of 150×150 μm is a compromise between the need for highest spatial resolution and lowest occupancy and the minimum space required by a readout channel of the electronic chip. The pixel system will have two barrel layers at the radii of 7 cm and 11cm. Two end layers (end caps or end disks) are placed on each side of the barrel. For the initial low luminosity phase , the lower particle density allows the barrel layers to be placed closer to the beam line at radii of 4 cm and 7 cm, respectively leading to better secondary vertex resolution.

These layers are composed of modular detector units, consisting of a thin segmented sensor plate bump bonded to highly integrated readout chips. This bump bonding technique (see figure 7) allows a direct connection of each pixel on the sensor to its associated readout circuit on the readout chip. In this configuration the pixel system will unite around 30×10^6 sensitive pixels and adequate data reduction on the readout level is demanded. Because of charge sharing between the pixels, supported by the Lorentz effect a resolution of 15μm in both cylinder coordinates $r - \varphi$ and z, respectively is expected. Since the number of pixels scales with the square of the sensitive area, pixel systems become inapplicable for larger detection regions.

High spatial precision and time resolution combined with adequate radiation hardness is also a characteristic of silicon strip detectors and makes them an ideal sensor for the intermediate

(a)

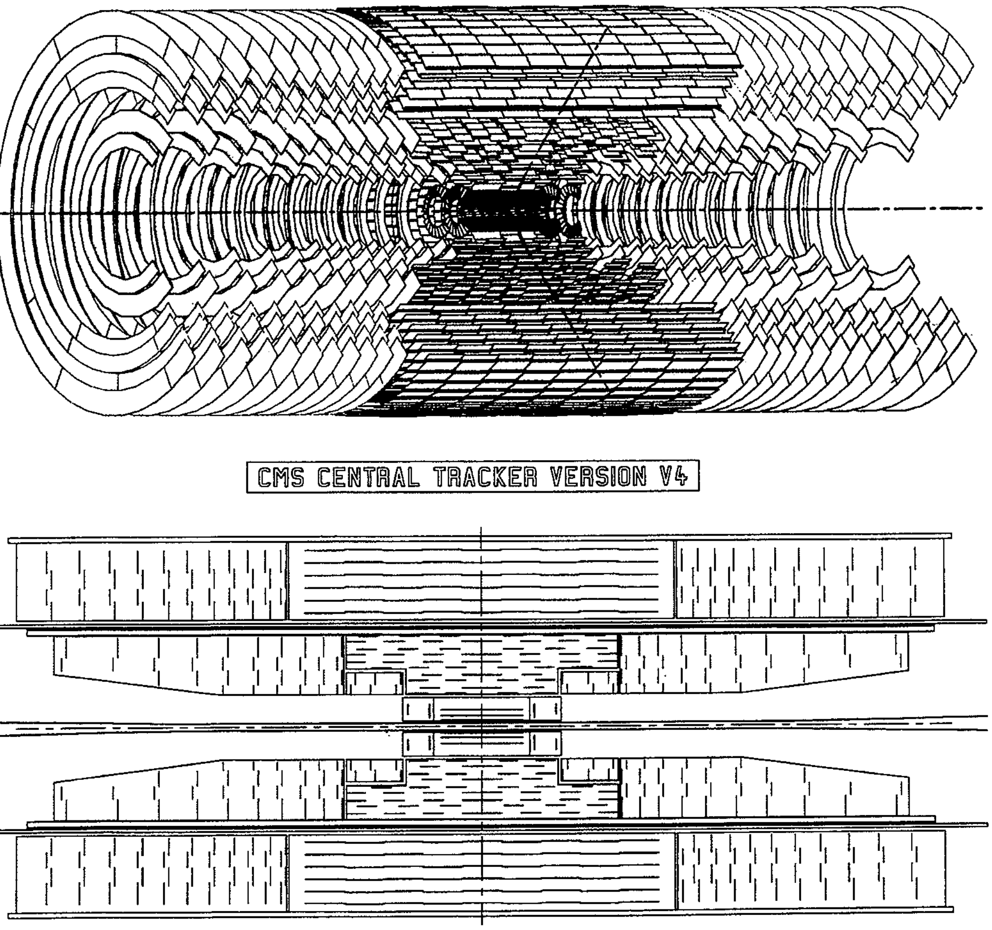

(b)

Figure 3: A three dimensional view of the CMS inner tracking detectors. (a) Perspective view; (b) side view. The overall length is 6 m; the outer diameter is 2.4 m. It is displayed how the modules in the barrel section (darkened) are grouped in concentric layers.

tracking region. The Silicon Strip Tracker (SST) consists of approximately 70 m^2 of instrumented micro strip detectors and is composed of a barrel region and end cap regions on both sides of the barrel. The barrel region consists of five cylindrical layers followed by six mini disks on each side. Each cap region consists of ten disks. A radial region between 22 cm and 60 cm is covered with the barrel part. All barrel layers are equipped with rectangular detectors and provide $r - \varphi$ information. In order to improve the resolution, layer 1, 2 and 5 are double sided with a small angle stereo geometry. Unlike the pixel detector, the sensors are tilted by 9° in order to compensate the Lorentz effect. The end caps consist of twenty disks encompassing concentric rings of wedge-shaped detectors. Correspondingly, the inner and outer radii of the end cap disks are also instrumented with double sided layers employing a stereo geometry for the $z - \varphi$ and radial measurement. The pitch of strips ranges from 61 μm to 244 μm and therefore the resolution varies around 15 μm reaching the digital limit ($\sigma \approx$pitch/$\sqrt{12}$) for the larger pitches where most of the charge is collected on a single strip.

The outer tracking layers employ micro strip gas chambers (MSGC). Fast charge collection from the thin gas volume ensures good time resolution. Good spatial resolution in the less congested outer regions is provided by detectors with a pitch that is coarser than that of the silicon strip detectors (200 μm compared to 50 μm). The MSCG tracker has been designed to provide an average number of 6 hits per track. Typical distances between two sensing electrodes (anode strips) are 200 μm. A charge spread over more than one strip, because of diffusion, allows (as in the silicon tracker) the use of interpolating algorithms to achieve a position resolution much better than the one dictated by the readout pitch. The main advantage compared to the inner silicon tracker is that the MSCG's allow to cover larger areas with a reasonable number of electronic channels. A main disadvantage is the speed of primary charge collection that cannot be easily reduced below the LHC bunch crossings. For the MSCG's six barrel layers and eleven end disks on each side are planned. As with the silicon strip detector some layers are double sided in order to improve the spatial resolution. Namely the layers 1, 4 and 6 of the barrel and the inner and the outer radii of the end caps are double sided. The resolution is expected to be between 35 μm and 100 μm, depending on the specific pitch of the layer.

Because of similarities in signal sizes, detector capacitances and the front end readout both, MSCG and SST, can use the same electronics which is developed in separate R&D groups at CERN (APV6 [13]).

2.3 A pixel-vertex detector for CMS

At LHC there is a bunch crossing every 25 ns with 20 – 25 simultaneous p-p collisions (σ_z=5.3 cm). This means roughly 10^9 collisions per second and each collision produces nearly 600 charged particles. Due to the extremely high particle fluxes and the small distances from the collision point, only pixel devices provide tolerable occupancies and true space point information with high resolution.

Conventional B hadron physics, including CP-violation, B_s-oscillations, rare B-decays and top quark physics will begin immediately after LHC startup. With increasing luminosities the pixels sensors will greatly help in pattern recognition of the many tracks present in one bunch crossing.

Due to the true lifetime of the B's and their kinetic energies, the decay vertices are about 0.5 mm away from the primary vertex. These are distances that can not be measured with present tracking devices. In order to allow an efficient tagging of B's as well as other long-lived objects (charmed mesons, τ), the tracking must extend as close towards the reaction vertex as possible.

The pixel detectors will confirm or reject track segments proposed by the outer tracker layers. Once a track has been successfully followed to the pixel layers, the two pixel hits will be crucial to extrapolate this track to the vertex with high precision. Therefore the main problem in tracking, that of pattern recognition, can be solved with pixel detectors. At a luminosity of 10^{34} cm^{-2}s^{-1} interesting events will be superimposed on a background of about 500 soft charged tracks within the rapidity range considered, originating from $\sim$ 15 minimum bias events which occur in the same bunch crossing. Only small cell sizes and occupancies below 1% achieved with the pixel detector (taking into account the large number of detector channels) can help to solve the pattern recognition problem.

2.3.1 Historical discourse of planar technology and micro strip detectors

Semiconductors have a long history in the detection of ionising radiation (eg. Ge detectors for the γ detection). In comparison to scintillating material they have better energy resolution (factor 10-50 higher). As tracking devices, semiconductors are relatively recent. Precise segmenting is needed which could only be achieved with a reliable structuring process.

The discovery of the charm quark in 1974 triggered a flurry of activity aimed at improving the tracking precision by an order of magnitude. Even photographic emulsion, an almost forgotten technique, was rediscovered. It was unique in producing the necessary tracking precision, but otherwise incompatible with the requirements of most modern experiments which are based on electronic detection systems. What was called for was a system similar to nuclear emulsions, equipped with electronic readout. Amongst the many ideas which were pursued (liquids, high pressure gases, etc.), the most successful were still solid state detectors, but based on silicon crystals instead of photographic emulsion. Silicon micro strips were among the first of these new high precision detectors, and have blossomed into a major industry, used in many experiments around the world.

In 1979 J. Kemmer reported the successful fabrication of low noise radiation detectors using the planar process which was a breakthrough for segmented (micro strip) detectors [18].

In 1983 structured semiconductors already achieved good position resolution in particle physics experiments and were tested and used by a CERN-Munich collaboration [10]. A schematic view of this prototype strip detector is shown in figure 4. It was designed on n-doped silicon with a

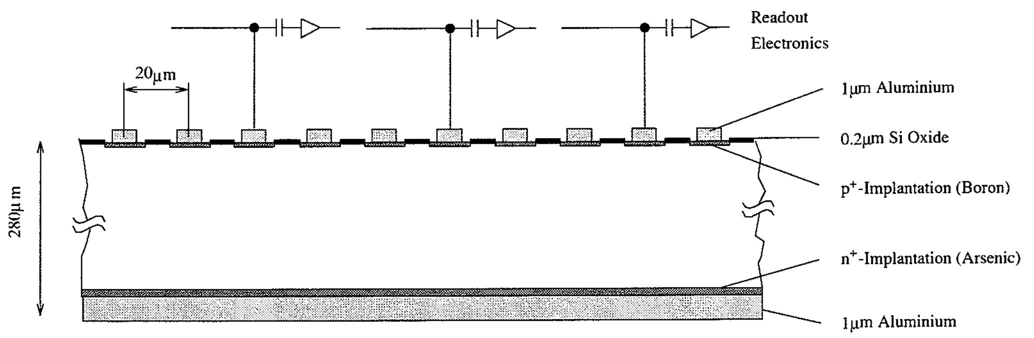

Figure 4: Schematic layout of the first working micro strip detector.

resistivity of 2 kΩ. The wafer with a diameter of 50 mm and a thickness of 280 μm was on one side covered with aluminium. The other side was doped with boron in order to produce p-type strips in the n-type silicon. These strips were 12 μm×36 mm wide with a pitch of 20 μm. Every third strip was readout by a charge sensitive amplifier. Because of the capacitive coupling between the charge collecting strips a position resolution of 4.5 μm was obtained. An improvement could be achieved if every strip was connected to an amplifier and Belau et al. calculated a resolution of 2.8 μm.

2.3.2 Pixel detectors

Attempts have been made to develop monolithic pixel detectors. These are sensors which combine signal collection and amplification in one sensor. For application at LHC most effort is focused on the 'flip chip' hybrid approach. Here, diode matrix and readout electronic chips are produced on separate substrates with matching geometries. These substrates can be connected using bump bonding techniques.

This method does not place severe demands on the sensor but rather on the electronics and connection techniques. Each pixel has its own dedicated amplification and discrimination stage and will hold the information until the event trigger arrives. Usually pixels without signal information are skipped over by the readout circuit which reduces data flow by orders of magnitudes.

Charged-Coupled Devices

CCD's were the first operating pixel detectors in high energy physics experiments delivering a real two dimensional space information. A CCD typically has a matrix-metallisation and an implantation. Potential barriers can be created separating and isolating the columns of pixels by applying a suitable voltage. Within one row the pixel charge could be shifted to the neighbouring pixel and thereby sequentially readout. The working schematics is shown in figure 5. Although the relative charge loss during the transfer is less than 10^{-4} it takes time to readout the entire device. Conventional CCD's have a read out time of 10s. Increasing the clocking speed (2MHz) provides a read out time of 15 ms for the same device [11]. Developments made to date show that this clock frequency is still not on the limit and that there is scope for improvement. But CCD's will fail to become a serious alternative to hybrid pixel detectors in high-energy physics experiments for two reasons: Many processing steps are necessary to fabricate such a device and the yield of large arrays is inadequate which makes CCD's expensive. Furthermore this complicated device is susceptible to radiation damage and a defect in a single pixel cell leads to the loss of the information accumulated in the whole row. By definition CCD's are 'dump pixel' devices. A pixel which receives a signal charge has no connection to the outside. The charge packets must be shifted sequentially to one or more output nodes on the device. The CCD's used up to now have an area of $\sim$1 cm^2 and they are equipped with one output node. With current technology, devices of ten

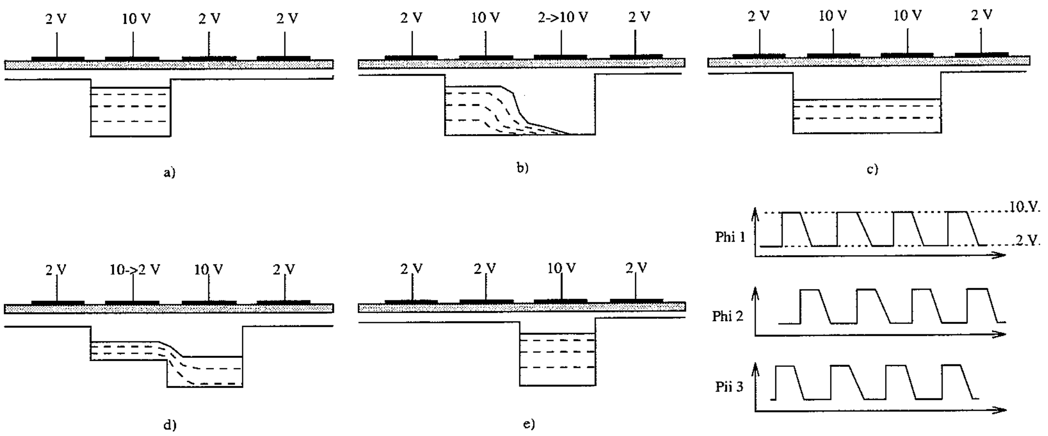

Figure 5: Working principle of a charged-coupled device.

times this area with up to eight output nodes are available, allowing designs of new tracking systems with much larger area coverage and fewer devices. One advantage of the CCD technology is the potential for extremely small node capacitances (<0.01 pF) and hence low equivalent noise charge.

Altogether there appears to be a degree of complementarity between the applicability of CCD's and other high precision tracking devices. If the particle fluxes allow, as in e^+e^- linear colliders and some fixed target experiments, CCD's which provide unambiguous measurement of space points, are probably optimal. At higher hit rates the readout is not finished within one bunch crossing. Since the charge collection remains active particle induced signals will mix up with the shifted charges. Hence, for higher fluxes silicon micro strips or hybrid pixel detectors should be considered. For large area coverage (say $> 1\text{m}^2$) micro strips are currently the only option. As an example of a successfully realised CCD-based high precision tracking device the SLD vertex detector at SLAC [12] should be mentioned.

Although this is a successful prove for a large scale application of CCD's their technological status to date does not meet the demands such as radiation hardness, readout speed or data reduction.

Hybrid pixel detector

The working principle shown in the following, represents the only sound application of pixel detectors for the LHC scenario. The structuring of the sensor into pixels is quite easy but the difficulty lies in accessing and amplifying these sensor signals.

The silicon pixel detector will need its associated amplifying circuit. The two dimensional segmentation of the sensor requires a similarly designed equivalent on the electronics side. In order to reduce the overall pixel number and create sufficient space for the analog readout cell (also pixel unit cell, PUC) a pixel size of $125\times125\ \mu\text{m}^2$ was suggested in the Technical Proposal [14]. New insight into the performance after irradiation, the improvement in resolution due to magnetic field effects (as it will be show in this work) and hit occupancy simulations allowed an enlargement of the original pixel size to $150\times150\ \mu\text{m}^2$. Nevertheless, the still large number of pixel channels requires autonomous hit detection in each PUC and storing of hits during the first level trigger latency on the chip. This must be achieved on the very limited chip area available and with the reduced intrinsic performance of a radiation hard process.

This readout chip designed to connect each sensitive pixel to its own amplifying circuit is a new technology. A schematic view of the pixel readout is shown in figure 6.

Two pixel unit cell (PUC) columns form a double column, which represent an independent readout unit. It is controlled by a circuit sitting in the column periphery and local bus lines connect all PUC's of a double column with this periphery. The circuit of each PUC can naturally be separated into two functional blocks. The analog block amplifies the tiny signal charge from the

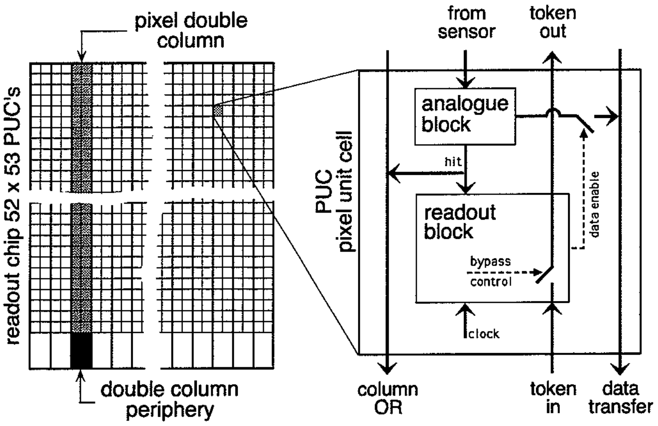

Figure 6: A schematic view of the pixel readout system.

sensor. If the signal is above a tunable threshold, the periphery is notified via one of the bus lines. The column periphery registers the associated bunch-crossing number (time stamping) and sends a token signal up and down the double column bypassing empty pixels. In the readout block of the hit pixel the token signal initiates the transfer of pixel address and analog signal, which are stored in a data buffer located in the periphery, waiting to be confirmed by the first level trigger. The confirmed time-stamps with their associated signals and addresses are transmitted directly from the periphery through analog optical links to the front end driver in the counting room, where digitisation is performed.

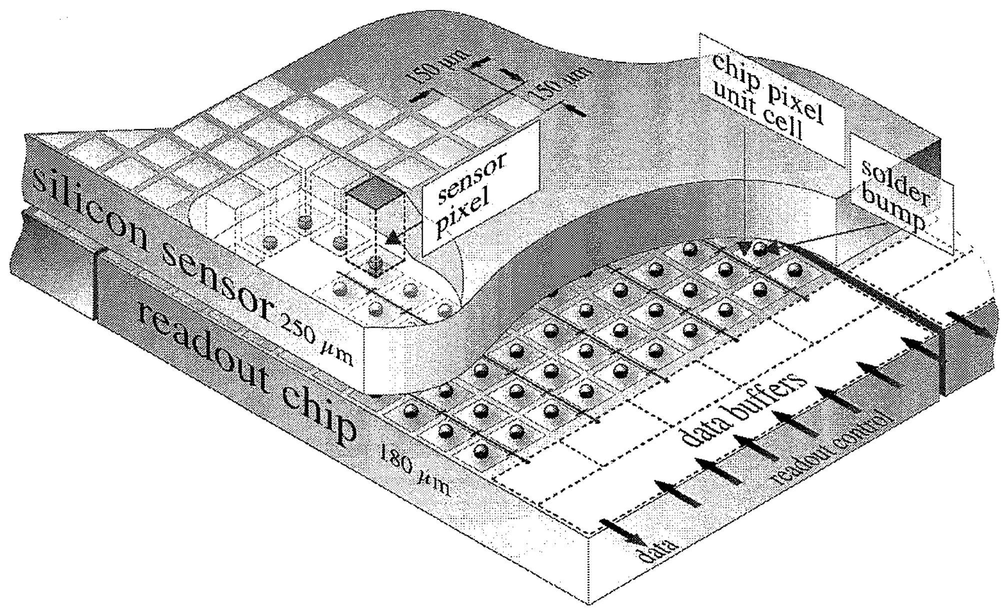

Figure 7: Schematic view of a pixel detector element. Each sensor pixel is connected via a solder bump to a pixel electronics cell on the readout chip, where the signal is amplified. The hits are stored in the data buffers where they wait for trigger confirmation.

There are several reasons for preferring an analog to a digital or binary readout system. One of them is related to an improvement in position resolution. Charge sharing between two or more pixels will be frequent as a consequence of non-normal incidence, magnetic field effects and energy loss fluctuations. In case of the pixels analog readout allows to extend the pixel size without loosing to much position information and therefore reduce the overall number of pixels. Another argument for analog readout is possible gain in overall performance. In contrast to an analog complex a digital system will lead to a smaller volume of data to be transferred, but adds other potential difficulties. A simple yes/no answer for example needs a very stable overall threshold condition for every single pixel. Since the two competing LHC experiments ATLAS and CMS hold different opinions on this subject, miscarriage or success will show which concept will survive for this application.

Moreover a connection technique between sensor and read-out chip is needed. Bump bonding is the only relevant technique to date. A schematic view of this bump bond connection forming a pixel detector hybrid is shown in fugure 7. Commercial vendors have been studying this problem for more than 30 years and there are a number of acceptable solutions that have been developed for industrial markets. But the bumps have to fulfil a number of important criteria:

- Stray capacitance is being added to the input of the electronics by the connection and therefore it is important to minimise these area.
- Minimisation of the bond connection resistance.
- Maximisation of the mechanical strength of the bond.

A successful start has been made to date developing a technique for an in-house bump bonding at the Paul Scherrer Institute [16].

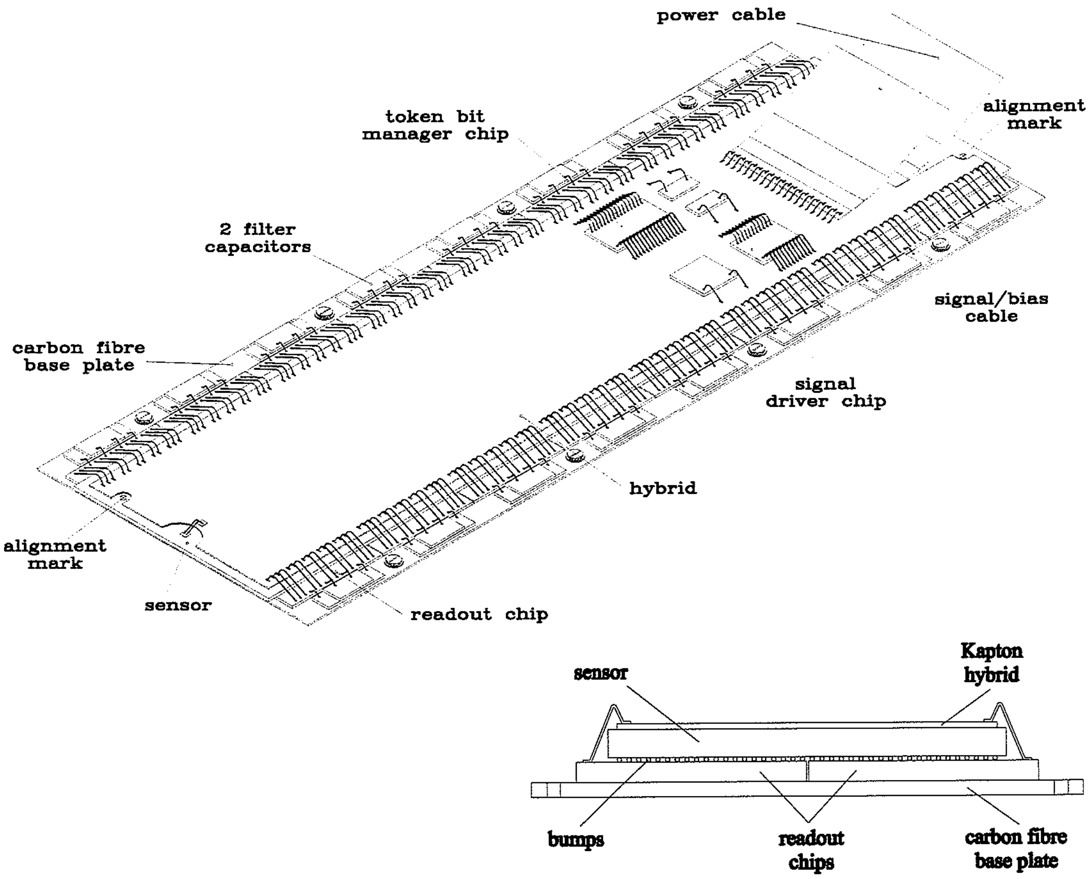

Figure 8: View of a 1.6 cm×6.4 cm pixel barrel module with 16 bump-bonded readout chips. The vertical scale of the insert is raised by a factor of 5.

A final barrel module with roughly 44'000 pixels and an area of 1.6 cm×6.4 cm is shown in figure 8. It hosts 2×8 readout chips bump-bonded to the sensor substrate. A thin hybrid circuit is glued on top of the module. On the hybrid, clock and control signals are distributed to the readout chips and vice versa the pixel signals from triggered events.

3 PHYSICS OF SILICON DETECTORS

This chapter does not pretend to be a complete introduction into semiconductor physics[2]. But it will treat all the important topics that are considered in the following investigations.

It starts with a general introduction into some aspects and particularities of semiconductors and gives an overview of some important terminologies. The second part will treat radiation induced changes of some important semiconductor properties in more detail.

3.1 Basic semiconductor physics

In order to understand the physics of semiconductor devices it is instructive to consider first the atomic bonding. One characteristic of silicon and other semiconductors is their crystal structure. The atoms within the crystal are arranged in a typical periodic order known as lattice. For every symmetric lattice a unit cell can be found which is representative for the entire lattice. Silicon and germanium have a diamond lattice structure as shown in figure 9 and belong to the cubic-crystal family. This characteristic lattice has its origin in the covalent bonding of the four electrons in the outer orbit where each atom shares its valence electrons with its four neighbours.

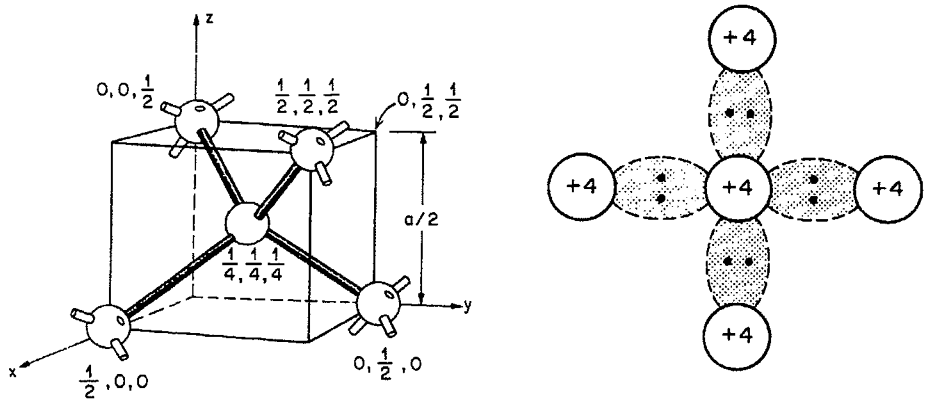

Figure 9: Diamond lattice.

For an isolated atom, the electrons of the atom can only have discrete energy levels. When we bring N atoms together to form a crystal, the N-fold degenerate energy level will split into N separate but closely spaced levels due to atomic interactions. This results in an essentially continuous band of energies. The detailed energy band structure of crystalline solids can be calculated. It is one of the most important results of the application of quantum mechanics to the description of electrons in a solid. Further decrease of the spacing causes the band originating from different discrete levels to lose their identities and merge, forming a single band. When the distance between atoms approaches the equilibrium interatomic spacing of the diamond lattice (with a lattice constant of 54.3 nm), this band splits again into two bands. These bands are separated by a region which designates energies that the electrons in the solid cannot occupy. This region is called forbidden gap, or band gap E_g. The upper band is called conduction band, while the lower band is called the valence band. The theoretical representation of these bands is confusing and barely

2. The interested reader may be referred to some comprehensive literature which treats this subject in a clear way like [19] and [20] and many others...

band like. But to delineate these energy levels in a band diagram is very helpful and illustrative. A full energy band cannot conduct and neither can an empty one.

At finite temperatures electrons and holes are subject to continuous thermal agitation and therefore can be excited from the valence band to the conduction band. We can now postulate the intrinsic semiconductor where the impurities are small compared to the thermally generated electrons and holes. If we now want to obtain the electron density in an intrinsic semiconductor we first have to evaluate the electron density in an incremental energy range dE. The density $n(E)$ is given by the product of allowed energy states per unit volume $N(E)$ and by the probability of occupying that energy range $F(E)$. Integrating $n(E)$ from the bottom of the conduction band (E_C=0, for simplicity) to the top of the conduction band E_{top} we get the electron density of allowed energy states per unit volume:

$$\mathrm{n} = \int_0^{E_{top}} n(E)\mathrm{d}E = \int_0^{E_{top}} N(E)F(E)\mathrm{d}E. \tag{3.1}$$

The probability that an electronic state with the energy E is occupied by an electron is given by the Fermi-Dirac distribution function

$$F(E) = \frac{1}{1 + e^{(E-E_F)/kT}}, \tag{3.2}$$

where k is the Boltzmann constant, T is the absolute temperature in Kelvin and E_F is the Fermi level[3]. Using equations (3.2) and (3.1) the densities of the electrons and of the holes can be calculated

$$\mathrm{n} = N_C \exp -\frac{E_C - E_F}{kT} \tag{3.3}$$

$$\mathrm{p} = N_V \exp -\frac{E_F - E_V}{kT}. \tag{3.4}$$

The lowest energy state in the conduction band is called E_C while E_V denotes the highest energy state in the valence band. The effective density of states in the valence band is N_V and N_C is the effective density of states in the conduction band. In case of equilibrium the electron density and the hole density are equal: $p=n=n_i$, with n_i the intrinsic carrier density. For intrinsic silicon the Fermi level is close to the band gap. This has the consequence, that at room temperature the concentration of free carriers is very low (approximately every 10^{12}th atom is ionised). This number of free charge carriers can be increased if silicon is doped with impurities. The semiconductor becomes extrinsic and further impurity energy levels are introduced. Depending on the number of valence electrons the impurity atom bears, it is called donator (five valence electrons, such as phosphorus) or acceptor (three valence electrons, e.g boron). The intrinsic silicon becomes n-type if a considerable number of donators is introduced. If the same is done with acceptors, the silicon becomes p-type.

Most semiconductor devices, however, incorporate both p- and n-type silicon and it is the junction between these regions that leads to their useful electrical characteristics. If p-type and n-type silicon are fused the large carrier concentration gradients at the junction causes charge carrier diffusion. The free electrons diffuse into the p-type region and the holes drift into the n-doped silicon. Thus an electric field will be built up, preventing further flow of the carriers. The responsible potential is called the built in voltage V_{bi} leading to a deformation of the conduction and valence bands. In addition a charge free region at the junction, the depletion region, emerges. The electric field and potential distribution across the depletion region are shown in figure 10. This deformation can be increased by applying an external voltage (V_{bias}) which amplifies the bending and generates an enlarged space charge region (depletion region).

Conventional silicon detectors used in high energy physics experiments as tracking devices are segmented p-n junction diodes operated at external bias voltage. This forms a sensitive region

3. This is the energy at which the probability of occupation is exactly one half.

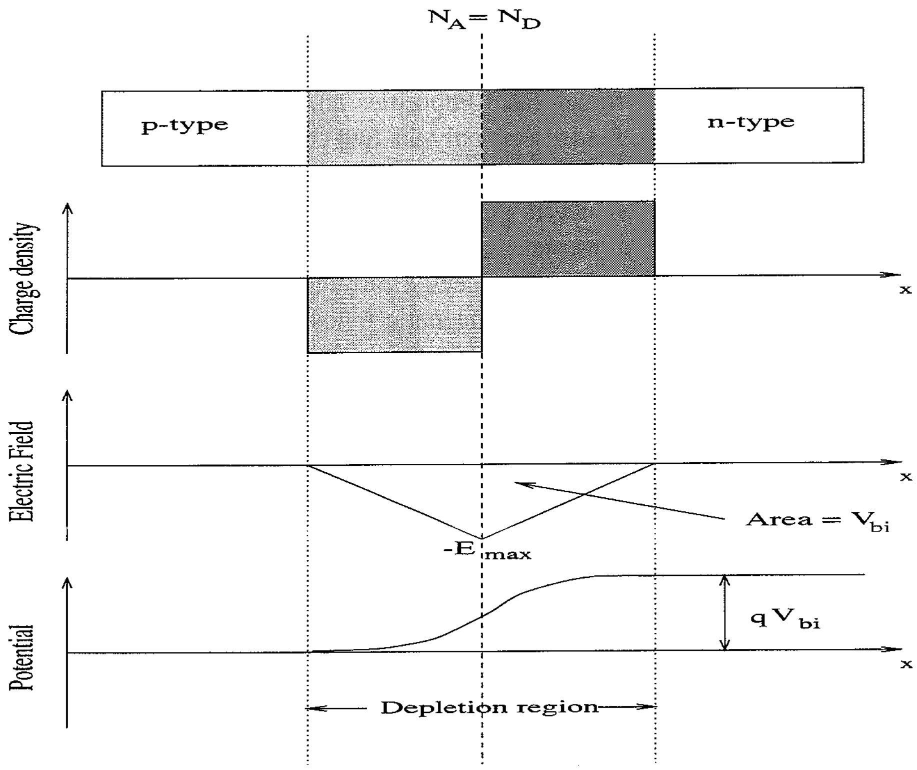

Figure 10: The p-n junction in equilibrium

depleted of mobile charge and sets up an electric field that sweeps charge liberated by ionising particles to the collecting electrodes.

Applying reverse bias voltage to a p-n junction extends the depletion region whose width d is a function of the applied voltage. As an example commonly used silicon detectors are based on a junction between a highly p-doped (only a few μm thick) layer and a low doped bulk of n-type silicon a device, also known as one-sided abrupt junction. Because of the different impurity concentrations of acceptors (N_{A}) and donors (N_{D}) with $N_{\text{A}} \gg N_{\text{D}}$, the depletion region extends chiefly into the n-side rather than into the p-side. An externally applied field V_{bias} in reverse direction increases the extension of the depletion region

$$d = \sqrt{\frac{2\epsilon(V_{\text{bias}} - V_{\text{bi}})}{qN_{\text{D}}}}. \tag{3.5}$$

The dielectric constant for silicon is $\epsilon = 11.9 \cdot \epsilon_0$ (≈ 1 pF/cm). The built in voltage is $V_{\text{bi}} \approx 0.8$ V for typical silicon detectors. An exact derivation of equation (3.5) can be found in [19] page 70 ff.

The concentration of ionised donors in the depletion zone is characterised by the effective doping concentration which is defined as

$$N_{\text{eff}} = N_{\text{D}} - N_{\text{A}}. \tag{3.6}$$

Using equation (3.5) it is found that N_{eff} is related to the bias voltage and the depletion depth by

$$N_{\text{eff}} = \frac{2\epsilon}{qd^2} V_{\text{bias}}. \tag{3.7}$$

Practical values for V_{bias} are frequently found to be an order of magnitude larger than V_{bi} which is therefore usually neglected. It will be seen that N_{eff} is a valuable measure for radiation induced damage. Likewise, equation (3.7) can be used to calculate the voltage which is used to extend the depletion zone over the full detector thickness.

3.1.1 Charge transport

In silicon detectors two ways of motion are distinguished: drift and diffusion. While the latter is not limited to specific particles (also impurities and crystal imperfections can diffuse), drift caused by an external electric field affects only the free charged particles in the semiconductor lattice. These two transport mechanisms are subject of this section.

Charge transport in semiconductors is very similar to transport phenomenon known from the kinetic gas theory. If carrier movement into a specific direction is observed, despite of the mechanism which is responsible for this movement, a current can be measured. In semiconductors often external influences such as electric or magnetic fields cause a charge drift into a specific direction.

Drift

If a small electric field is applied to a semiconductor, each carrier will experience a force $F = -q\vec{E}$ and is accelerated along the field. Because of phonon scatterings with the lattice and with impurities the charge will lose momentum. Macroscopically, a drift with constant velocity is observed. The momentum applied to a carrier between two collisions is given by $p_{\mathrm{drift}} = -q\vec{E}\tau$ and the momentum gained is $p = m^*\vec{v}_{\mathrm{drift}}$. Here, m^* is the effective mass of the carrier in the lattice and τ is the mean free time between two scattering events also denoted as relaxation time. Therefore, the drift velocity can be obtained by equating

$$-q\vec{E}\tau = m^*\vec{v}_{\mathrm{drift}} \tag{3.8}$$

$$\vec{v}_{\mathrm{drift}} = -\left(\frac{q\tau}{m^*}\right)\vec{E} = \mu_{\mathrm{e,h}}\,\vec{E}. \tag{3.9}$$

Equation (3.9) states that the drift velocity is proportional to the applied electric field. The proportionality factor is called electron (μ_{e}) and hole mobility (μ_{h}), respectively [21]

$$\mu_{\mathrm{e}} = 1350\ \mathrm{cm^2V^{-1}s^{-1}}$$

$$\mu_{\mathrm{h}} = 450\ \mathrm{cm^2V^{-1}s^{-1}}.$$

Equation (3.9) implies that a carrier can be accelerated as fast as one likes by increasing the electric field. Unfortunately this is not the case and equation (3.9) is not valid for high electric fields.

Hot electron problem

Within a high electric field, free charge carriers (electrons or holes) gain energy from this field. Since the carriers must remain in the band structure of the semiconductor this energy has to be mediated to the lattice through increased carrier-phonon scattering. This effect becomes important if the energy gained from the field is of the same order of magnitude as the thermal energy of the carriers (when the drift velocity $\mu \cdot \vec{E}$ becomes greater than the thermal velocity $\approx \sqrt{kT/m^*}$). Since this behaviour is similar to an increase of the carrier temperature the carriers are said to be hot (hot electron effect (see e.g. Ferry in [22])). Due to the increased phonon scattering the mobility does not remain constant but decreases with increasing field strength. The expected energy increase goes into heating up the lattice rather than into the kinetic energy of the carrier. Then, equation (3.9) is no longer valid because the drift velocity does no longer increases linearly with the field. At very high electric fields, the velocity almost saturates, increasing very slightly for increasing electric fields. An analytic expression based on an empirical model for the mobility dependence on doping density and electric field strength is derived in reference [25]

$$\mu = \left\{\mu_{\mathrm{min}} + \frac{\mu_{\mathrm{max}} - \mu_{\mathrm{min}}}{1 + \left(\frac{N_{\mathrm{eff}}}{N_{\mathrm{ref}}}\right)^{\alpha}}\right\} \cdot \left\{\frac{1}{\left(1 + \left(\frac{\vec{E}}{E_{\mathrm{c}}}\right)^{\beta}\right)^{1+1/\beta}}\right\} \quad . \tag{3.10}$$

The first term in equation (3.10) describes the doping dependency of the mobility whereas the second stands for the field dependency and E_c is a function of doping given by

$$E_c = \frac{v_m}{\mu_{min} + \frac{\mu_{max}-\mu_{min}}{1+\left(\frac{N_{eff}}{N_{ref}}\right)^\alpha}} \tag{3.11}$$

Here, N_{ref} is a normalisation parameter, as well as α. The factor $\beta = 1$ is valid for holes and $\beta = 2$ for electrons where v_m is a constant related to the maximal saturation velocity. The mobility in intrinsic silicon is μ_{max} and μ_{min} stands for the mobility saturation value at very high doping.

However, if the doping variation is so small that the mobility can be assumed to be independent ($N_{eff} \leq 10^{16}\,\text{cm}^{-3}$) the field dependence and the temperature are the only remaining scaling parameters. Again, there are empirical expressions for the mobility and the velocity [25] given by

$$\mu = \frac{\mu_0}{\left(1+\left(\frac{E}{E_c}\right)^\beta\right)^{1/\beta}} \quad \text{and} \quad v = v_m \cdot \frac{E/E_c}{\left(1+\left(\frac{E}{E_c}\right)^\beta\right)^{1/\beta}} \tag{3.12}$$

with $\mu_0 = v_m/E_c$. Using the equations (3.12) the velocities and mobilities of electrons and holes, respectively can be calculated which is visualised in the graphs of figure 11

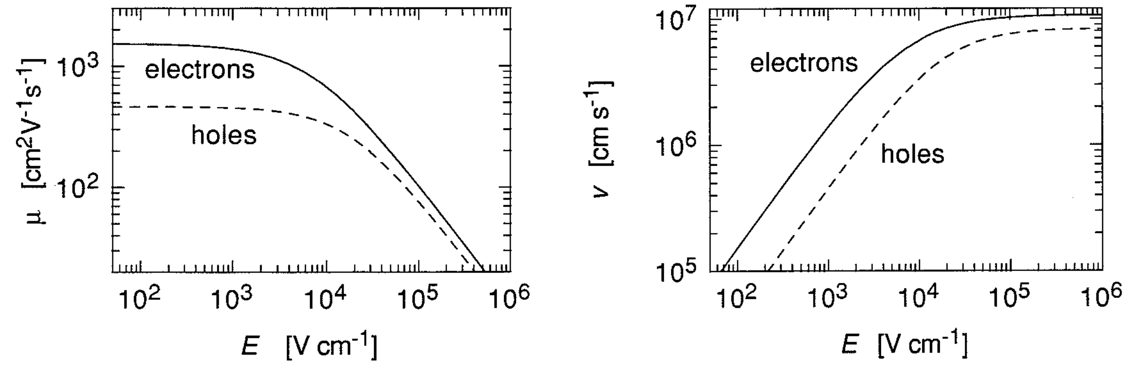

Figure 11: Left: mobility, right: drift velocity vs electric field equated for electrons and holes in silicon according to equations (3.12); $T = 300\,\text{K}$, $N_{a,d} \leq 10^{16}\,\text{cm}^{-3}$.

Furthermore complexity increases if in addition a magnetic field comes into play. It was shown (see A.C. Smith in [22], [23], [24]) that transport of electrons and holes in semiconductors in electric and magnetic fields can be described relatively well by a single classical (vector-) equation for each particle. One parameterisation can be found in [23]

$$m^* \cdot \frac{d^2\vec{r}}{dt^2} = q \cdot \frac{\mu_H}{\mu} \cdot \frac{d\vec{r}}{dt} \times \vec{B} + q \cdot \vec{E} + \frac{q}{\mu} \cdot \frac{d\vec{r}}{dt} \quad , \tag{3.13}$$

where $\vec{r}$ is the position vector of the electron or hole and $\vec{B}$ ($\vec{E}$) the magnetic (electric) field, respectively. The mobility μ is introduced in equation (3.10) and μ_H is the Hall mobility (see equation (3.34)).

Diffusion

Another transport mechanism well known in the kinetic gas theory is diffusion. If there is a spatial variation of carrier concentration in the semiconductor material, the carriers tend to move from a region of high concentration to a region of low concentration. This diffusion, first described by Nernst in the kinetic gas theory was extended by Einstein relating the mobility of electrons and holes to the diffusion coefficient D_n

$$D_n = \frac{kT}{q}\mu. \tag{3.14}$$

The nearly Gaussian distribution for electrons and holes by diffusion is explained in the theory of the Brownian motion. A correlation between the standard deviation and the diffusion coefficient is given by [26]

$$\sigma = \sqrt{2Dt}, \tag{3.15}$$

where t is the drift time. Diffusion is also active in the depletion region where drift governs. Using equation (3.15) the spread of a charge cloud can be calculated.

In the neutral regions outside the depleted region there is no significant electric field and the carriers move only by diffusion. If electron-hole pairs are generated in the undepleted region there is a finite chance that some of the carriers reach the depletion region before they recombine causing diffusion current.

3.1.2 *Electric field distribution*

It was shown in section 3.1.1 that the electric field $\vec{E}$ is defined as the force acting on a unit of positive charge. Figure 12 shows the electric field distribution on the example of the one-sided abrupt junction mentioned on page 17 with a p$^+$-implant in n-bulk material. For one dimension

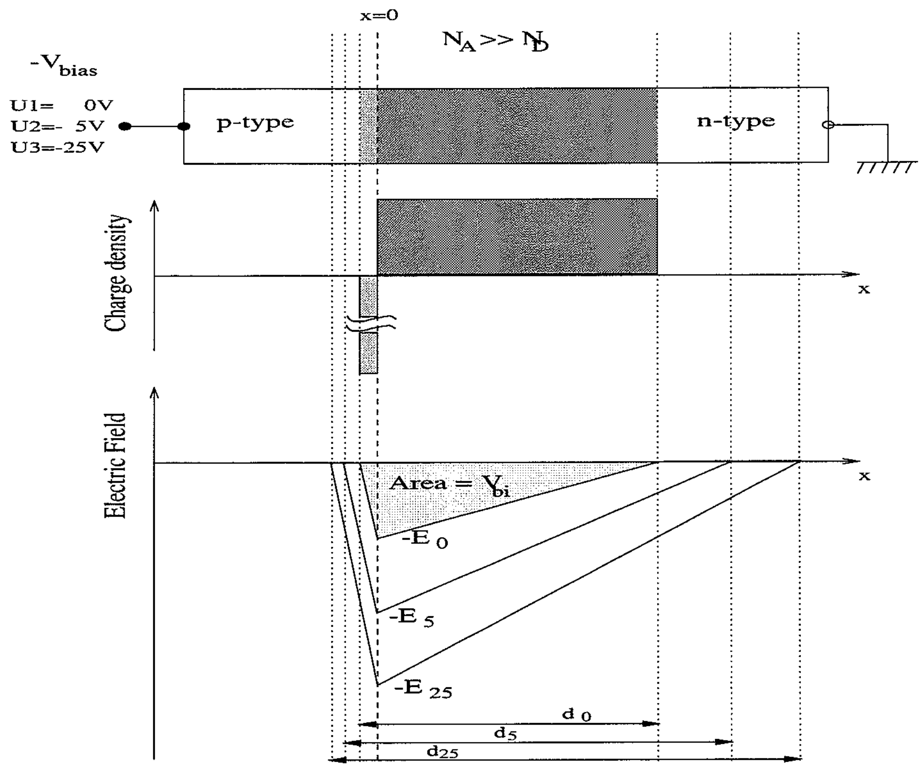

Figure 12: One-sided abrupt junction with $N_\mathrm{A} \gg N_\mathrm{D}$ under different reverse bias with the corresponding electric field distribution.

the electrostatic potential is

$$\vec{E} = -\frac{d\phi}{dx}. \tag{3.16}$$

For high p$^+$-doping, the growth of the space charge region into the region of high doping is negligible small compared to the growth towards the n-side. According to the simple development of $\vec{E}$ along the depletion depth it can be approximated with a straight line. From figure 12 it can be seen that the electric field is maximal for $x = 0$. Taking this into consideration the electric field strength in x can be calculated as

$$E(x) = \frac{2V_\mathrm{bias}}{d}\left(1 - \frac{x}{d}\right). \tag{3.17}$$

Here, it is assumed, that V_{bias} is the depletion voltage used to fully deplete the detector with the thickness d. This model satisfies the description of the electric field of simple devices such as junction diodes or surface barrier detectors. In case of more complex devices as for example strip or pixel detectors the field lines are not parallel throughout the entire detector. Near the surface the field lines are focused towards the charge collecting implants. Simulations show that this bending is dependent of the size of the implants and the space (gap) between them [27]. In case of radiation induced damage it is observed that these effects are amplified because of an increase of the oxide charges and due to underdepletion (see sections 3.2.1 and 6.7). Figure 13 shows the

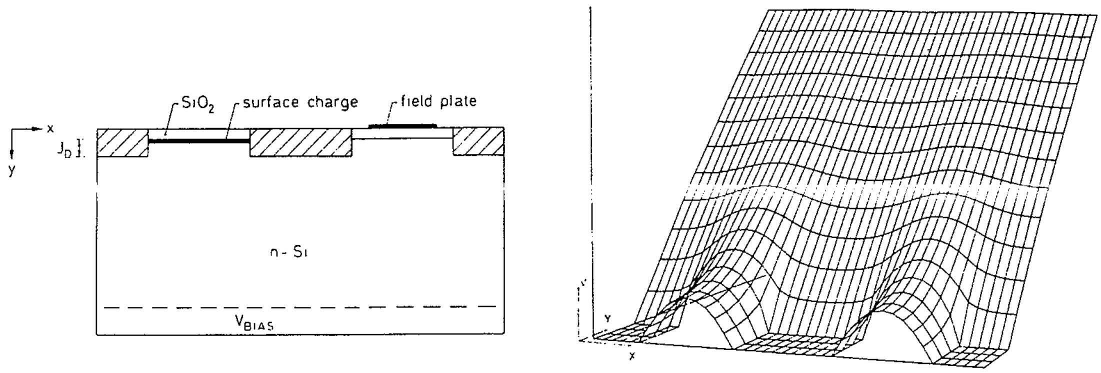

Figure 13: Left: Model of the strip detector. Either calculated with surface charge accumulation or with a field plate. Right: calculated potential distribution. The elevation between two strips stands for smaller field strengths (from [27]). This elevation increases with increasing oxide charge.

potential distribution of a two dimensional model. The field pattern was calculated by solving the two dimensional Poisson equation for the potential distribution of the defined area. In this case a charge carrier following this potential is inevitably either flushed to the left or to the right strip and diffusion is ineffective. The potential elevations between the strips become higher if the oxide charge increases.

3.1.3 Leakage current

The leakage current (sometimes named reverse current or dark current) is always present in a reverse biased semiconductor. Imperfections within the semiconductor such as lattice defects can introduce energy levels into the forbidden gap. Some of these energy levels act as combination and recombination centres for the transition of electrons and holes between the conduction and valence bands. The theory of such processes taking place trough combination recombination centres acting in the intermediate energy level has been worked out by Hall, and by Shockley and Read [28]. Four processes take place at such a centre:

- Capture of an electron,
- emission of an electron,
- the capture of a hole
- and the emission of a hole.

Because of reduction of the carrier concentration in the space charge region, only the emission processes are important.

Under equilibrium conditions electron-hole pairs are generated continuously everywhere within the semiconductor. In the absence of an applied voltage, the electron-hole pairs recombine and therefore no current flow results. However, if a reverse bias voltage is applied the electron-hole pairs, once generated, will be separated and their probability of recombination is diminished. Usually one distinguishes the various contributions to the reverse current by the region of the semiconductor where an electron-hole pair was generated. If an electron-hole pair is generated within the reverse-biased depletion region the resulting current component is referred as generation current. Charge created in the neutral regions is often called diffusion current.

In the following only the current created in the depletion zone (generation current) is of interest. Only those centres whose energy levels are close to the Fermi level E_F contribute significantly to the generation rate.

One electron-hole pair generated provides one electronic charge to the external circuit. Thus, the magnitude of the current due to generation within the depletion region will be given by [20]

$$I_{gen} = \frac{n_i}{2\tau_0} q d A_J, \tag{3.18}$$

where A_J is the cross-sectional area of the p-n junction. It can be seen that n_i is the number of generated electrons and τ_0 is the corresponding effective lifetime of the carrier within the reverse biased depletion region. The generation current is dependent on the magnitude of the applied reverse bias voltage. At higher bias voltages the depletion depth is larger, more generation centres are included and the generation region increases proportionally with d.

In case of radiation damage the number of generation centres grows. Thus the generation current increases dramatically. High currents can lead to thermal runaway and unstable operational conditions. Empirically the change of leakage current due to irradiation can be written as [29]

$$\Delta I_{gen} = \alpha\phi. \tag{3.19}$$

The damage constant α depends on the type of device irradiated and on the radiation itself. The bulk generation current is given by

$$I(T) \sim T^2 \exp - \left(\frac{E_g}{2kT}\right), \tag{3.20}$$

where $E_g = 1.121$ eV is the band gap of silicon. Therefore cooling becomes inevitable.

3.1.4 Junction breakdown

It is known that all diodes will conduct in the reverse direction if a sufficiently large reverse voltage is applied. This phenomenon is called junction breakdown and will destroy the detector. This breakdown occurs, when the maximum field in the depletion region $\vec{E}_{max}$ reaches the critical field $\vec{E}_{crit}$. For a one-sided step junction, the maximum field with the critical field using can be calculated using equation (3.5)

$$E_{max} = 2\frac{V_{bias} + V_{bi}}{d} = \sqrt{\frac{2V_{bias}N_{eff}}{\epsilon}} = E_{crit}. \tag{3.21}$$

Finally, V_{bias} is defined as the breakdown voltage V_{BV} of the junction.

$$V_{BV} = \frac{\epsilon E_{crit}}{2qN_{eff}} \tag{3.22}$$

This shows that the breakdown voltage is inversely proportional to the impurity concentration for a constant critical field. The simple fact that the breakdown voltage will decrease with increasing impurity concentration has the consequence of smaller signals due to partial depletion.

3.2 Radiation effects

Silicon detectors such as tracking detectors are typically used very close to the interaction point. Because of increasing energies and higher luminosities of the future collider experiments they are exposed to ever growing fluences causing severe damages and degradation in detector performance. Thus radiation effects in semiconductors have become a field of intense investigations. High energetic particles interact with a semiconductor on different ways.

- Along a particle track electron-hole pairs are produced by *transient ionisation.* An externally applied electric field separates these pairs before they recombine and brings them to the charge collecting electrodes. Particle detection with semiconductors is based on this effect.

- *Long term ionisation* concerns the insulation layer of a semiconductor. Ionised atoms do not return to their initial states and the electrons and holes which are produced in this layer are fixed causing charged regions. This long term ionisation is responsible for surface damage (see section 3.2.1).
- High energy particles are also responsible for *displacements*. These are dislocations of atoms from their normal sites in the lattice, producing less ordered structures, with long term effects on the detector properties. The number of displacements determines the degradation of the bulk (see section 3.2.2).

Generally, charged particles lose part of their energy by ionisation when traversing matter. The energy loss which is not due to ionisation (non ionising energy loss, abbreviated with NIEL) is for high energetic charged particles mainly based on Rutherford scattering. In contrast neutrons lose their energy manly due to elastic scattering with atomic nuclei. The dependency of the energy and of the type of the incident particle is given in figure 14. It shows that towards higher energies the proton, pion and neutron damage factors $D(E)$ are within the same order of magnitude.

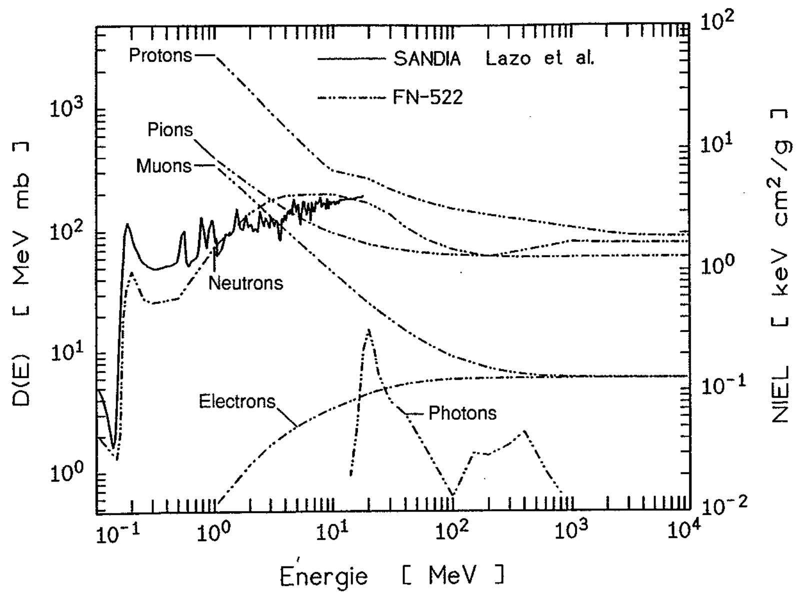

Figure 14: Non ionising energy loss calculated (dash-dotted lines) for different particles at different energies. The correlation between the damage factor $D(E)$ and NIEL is given in [33].

In silicon this scattering causes lattice displacements which, together with the involved defect mechanisms are made responsible for a number of performance degradations of the detector:

- Increase of the bulk leakage current leading to increased noise and power dissipation.
- Build up of an effective p-doping, which requires ever increasing depletion voltages.
- Charge trapping in the depletion region.
- After initial annealing a reverse annealing occurs where initially electrically inactive defects become active during several months after irradiation, thereby increasing the effective doping even more.
- Reverse annealing is temperature dependent and can be controlled by keeping the detectors at appropriate temperatures below 0°C. Continuous cooling is needed all the time once operation of the LHC has started. This also helps in reducing the leakage current.

Simulations have shown that the lifetime of an inner silicon detector at a LHC experiment is not limited by the neutron fluences. For a distance of $\sim$7 cm from the interaction point and an integrated luminosity of 5×10^5 pb^{-1} (corresponding to the first six years of LHC operation) the neutron flux is expected to be of the order of 10.8×10^{13}cm^{-2}. The fluence of charged pions is almost an order of magnitude larger (71.8×10^{13}cm^{-2} see [15] A8). This is the reason why this work is focusing on the investigation of pion induced radiation damage.

3.2.1 *Surface damage*

Surface damage plays a minor role for silicon pixel sensors but it is usually the most important damage mechanism for electronic chip components. Radiation induced charge up of the oxide reduces the transconductance of the transistor and shifts the threshold voltage of the gate.

Every silicon sensor is coated with a small oxide (generally SiO_2) layer during the passivation step of detector production. Depending on the process a certain amount of fixed oxide charges is already introduced during this step.

Surface damage concerns damages induced in this layer and the interface to the silicon. Basically, the above mentioned interactions between high energetic particles and matter of the oxide are the same as in the bulk but with different consequences. Displacements occur in the same way but are of minor influence. With irradiation the oxide layer gets positively charged. This is caused because of the charge generated by the passage of an ionising particle. The free electrons and holes created in the oxide are driven by the electric field towards the oxide-silicon interface and metal electrode, respectively. The mobility for electrons in the oxide ($\mu^{\mathrm{e}}_{\mathrm{SiO_2}}$ ~20 cm^2/Vs) is much larger than for holes ($\mu^{\mathrm{h}}_{\mathrm{SiO_2}}$ ~2×10^{-5}cm^2/Vs). Therefore, the probability for the electrons to be trapped or to recombine is very small compared to the holes. The concentration of trapped holes grows progressively increasing the intrinsic positive charge in the oxide. In conjunction with that, interface states are created at the SiO_2-Si interface. These states are additional energy levels in the silicon and influence the generation current properties of the detector.

Furthermore, the presence of fixed positive oxide charges leads to an accumulation of free electrons below the surface. It is expected that this leads to inhomogeneities of the electric field strength at the edges of two neighbouring implants [30].

3.2.2 *Bulk damage and type inversion*

The study of a detailed defect mechanism is still subject of investigations to date. Although understanding of the origin of silicon bulk damage has improved microscopic models still owe a full description of all the observed effects. In particular, a theoretical explanation for the observed correlation between the leakage current and the effective doping concentration could help to define the possibilities for detector hardening.

As mentioned, bulk damage in silicon results from particle induced lattice displacement throughout the entire crystal. Energetic electrons and photons can lead to single displacements and therefore cause bulk damage. But it is the heavier particles such as pions, protons and fast neutrons which are the dominant source of bulk damage since they transfer much more energy to the atoms. The macroscopic effects caused by this damage are a strong increase in the reverse current of the device and also changes in the effective resistivity of the substrate. Under reverse bias voltage the detector behaves as if the substrate is becoming less n-type as the dose increases, reaching a point defined as type inversion where the substrate is essentially intrinsic. Continuing beyond this point the detector behaves as if the bulk is becoming increasingly p-type like.

The microscopic defects generated by displacements are lattice vacancies (V) and silicon interstitial atoms (I). Both of them can move at room temperature, with different mobilities. Some of the displaced atoms carry a high recoil energy, producing a cascade of interactions such as new displacements or secondary recoil atoms. Each of these terminates in a damage cluster containing a high density of interstitial and vacancy pairs as well as significant disorder. In these clusters with high concentrations of vacancies and interstitials direct recombination occurs, leading to partial reordering. Measurements show that vacancies and interstitials are very mobile [31] and those escaping initial recombination diffuse through the crystal reacting with other defects and impurity atoms, particularly oxygen and carbon. Moreover there seems to be evidence that vacancies join forming divacancies (V_2) and higher orders of vacancies. They are not mobile and remain trapped representing good candidates responsible for the observed donor removal [32] and form stable defect complexes.

All defect complexes can be grouped into two categories: shallow and deep level defects. The energies of the shallow levels are found closer to the energy of the band edges. In silicon shallow acceptors and donors, such as boron and phosphorus, are used to dope the material. Deep levels can exist in different charge states depending on conditions in the material and the behaviour of the trap as a donor or acceptor. A device model [31] which includes a single acceptor level at the middle of the energy gap described successfully the evolution of $N_{\rm eff}$ with the fluence.

Another hypothesis is the donor removal by creation of vacancy-phosphorus complexes, and the generation of shallow acceptors [34]. But the removal rate was measured to be much lower than predicted.

An empirical macroscopic parametrisation for the dependency between the fluence and $N_{\rm eff}$ is given by [33]

$$N_{\rm eff}(\Phi) = N_{\rm D,0}\, e^{c_{\rm D}\Phi} - N_{\rm A,0}\, e^{c_{\rm A}\Phi} - b\Phi, \qquad (3.23)$$

where the first and the second term describe a donor (acceptor) removal from the starting donor concentration $N_{\rm D,0}$ (initial acceptor concentration $N_{\rm A,0}$) with the removal rates $c_{\rm D}$ ($c_{\rm A}$). The radiation induced increase of acceptors is parametrised by b. The change of $N_{\rm eff}$ with dependence on the neutron fluence is shown in figure 15. The points show measurements of different materials from different vendors (SINTEF and Micron). The dashed line corresponds to the calculation using equation (3.23).

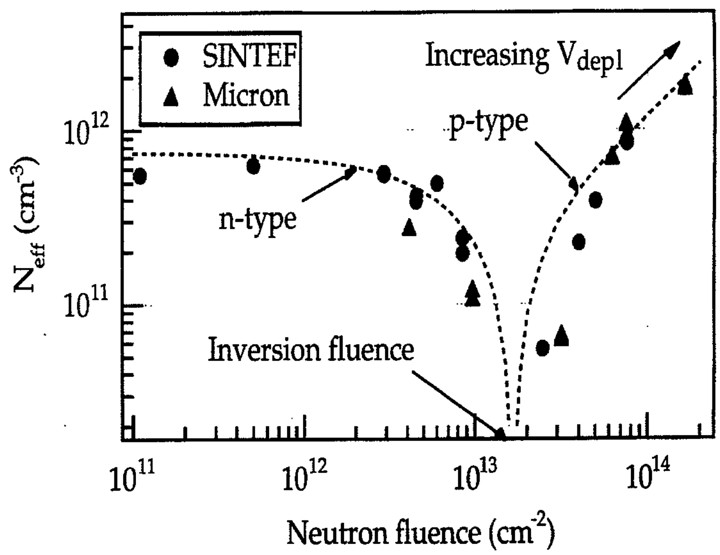

Figure 15: The effective doping concentration $N_{\rm eff}$ as a function of the neutron fluence. The data points show the measurements on two high resistive n-type materials. The dashed line represents the calculation performed using equation (3.23).

Type inversion does, however, not have implications on the detector performance and it is not a serious point of failure; in most respects the device behaves as if the junction has moved to the n^+-junction side. This is why the CMS pixel sensors start with n^+-pixels in n-bulk (see section 4). Actually the increase of $N_{\rm eff}$ is responsible for lifetime restrictions of a silicon sensor leading to an increase of the bias voltage and the leakage current. The sensor lifetime ends when it can no longer sustain the increased bias voltage.

Trapping

Radiation generated energy levels show responsible for a significant increase of the leakage current. In contrast, charge collection is disturbed by shallow energy levels [33]. These trapping centres reduce the number of emitted electron-hole pairs. The capture radius of these levels is big enough that they absorb free carriers from the valence or conduction band. This can be quantitatively described by [35]

$$\frac{\Delta Q}{Q} = \frac{a\, t_{\mathrm{c}}}{\tau}, \tag{3.24}$$

with τ as the trapping time and $a = w/2d$, where w is the actual carrier drift length. Equation (3.24) is based on the assumption that the time until the trapped carrier is reemitted is much longer than the effective charge collection time t_{c}. It may be modified to describe trapping at higher fluences. Reference [36] reports on current pulse shape studies where they observed a linear dependency between the charge loss and the pulse width except for bias voltages below full depletion.

Using an analytical relationship for the dependence of carrier mobility on the electric field, the charge collection time can be calculated. The calculation then includes the formalism of induced current shapes and is found to be

$$t_{\mathrm{c}}^{\mathrm{e}} = \frac{d}{V_{\mathrm{s}}} + \tau_{\mathrm{e}} \ln \frac{E(x_{\mathrm{i}})}{E(x_{\mathrm{f}})} \tag{3.25}$$

and

$$t_{\mathrm{c}}^{\mathrm{h}} = \frac{d}{V_{\mathrm{s}}} + \tau_{\mathrm{h}} \ln \frac{E(x_{\mathrm{i}})}{E(x_{\mathrm{f}})}, \tag{3.26}$$

for the mobility relationship from [37], where

$$\tau_{\mathrm{e,h}} = \frac{\epsilon}{q \mu_{\mathrm{e,h}} N_{\mathrm{eff}}}. \tag{3.27}$$

The indexes i and f refer to the initial and final values of the charge carrier position. The measurements of [36] show good agreement with the calculated collection time of equation (3.27).

A similar observation is given in [34]. The linear correlation between the trapping and the fluence is approximated

$$1/\tau \approx \gamma \phi, \tag{3.28}$$

with $\gamma_{\mathrm{h}} = 2.7 \times 10^{-7}$ cm^2/s and $\gamma_{\mathrm{e}} = 1.2 \times 10^{-6}$ cm^2/s as slope parameters.

Annealing and long term behaviour

An interesting effect is the partial self recovery from radiation induced damage. After irradiation N_{eff} changes as a function of time. Two phases can be distinguished.

Immediately after irradiation N_{eff} decreases until a minimum is reached. The time scale of this beneficial annealing is dependent on the temperature under which the irradiated sensor is kept. If heated to 80°C most of the beneficial annealing is finished within 4 minutes [38]. If kept around 0°C this annealing can extend to more than a year (see section 6).

After this minimum N_{eff} starts to rise again. An effect that can be related to the microscopic model creating deep acceptor levels. This reverse or anti-annealing can be mainly suppressed at low temperatures below about 5°C [39]. Generally, it is a mechanism much slower than the observed beneficial annealing but the changes on N_{eff} are much larger.

3.3 The Lorentz effect

The CMS pixel detector group has decided to use an analog readout of the pixel sensors which benefit of charge sharing effects. The pixel cell size of (150 μm)^2 is therefore quite large. In this respect a large Lorenz drift angle is of great interest. It is caused by a magnetic field (4 Tesla at CMS) perpendicular to the drift direction of the charge carriers.

A general equation of motion for charge carriers in an electric field and under the influence of a magnetic field was quoted in equation (3.13).

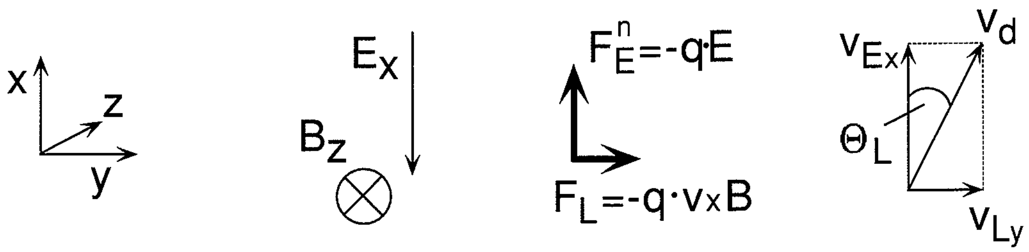

Figure 16: Graphical interpretation of the relation between the charge carrier velocity and the magnetic field.

Here, the necessary background for a carrier drifting in an electric field E_x and a magnetic field B_z will be presented. In figure 16 a model is used to give an idea crude of the effect which is subject to the Lorentz angle measurement in appendix B. According to figure 16 the Lorentz force acts on every charge carrier with a velocity component perpendicular to the magnetic field with

$$\vec{F}_{\mathrm{L}} = -q\vec{v} \times \vec{B}. \tag{3.29}$$

This force gives the carrier a new direction ($\mathrm{v_d}$) and the angle between the initial and the resulting direction is

$$\tan \Theta_L = \frac{v_y}{v_x}. \tag{3.30}$$

The value for the velocity along the direction of the electric field is given in equation (3.9). Assuming that an electron is deflected its velocity v_y with respect to the magnetic field can be derived from equation (3.29)

$$v_y = -\frac{q\mu_e E_x B_z \tau}{m^*}. \tag{3.31}$$

The two equations (3.29) and (3.31) used in equation (3.30) lead to

$$\tan \theta_{\mathrm{L}} = -\left(\frac{q\tau}{m^*}\right) B_z \tag{3.32}$$

$$\tan \theta_{\mathrm{L}} = \mu_{\mathrm{H}} \vec{B}. \tag{3.33}$$

Equation (3.33) is the general relation between the applied magnetic field and the Lorentz angle θ_{L}. The proportionality factor μ_{H} is the Hall mobility which is related to the drift mobility via

$$\mu_{\mathrm{H}}^{\mathrm{e,h}} = r_{\mathrm{H}}\, \mu_{\mathrm{e,h}}. \tag{3.34}$$

The hall factor r_{H} is a dimensionless value determined to be [21]

$$r_{\mathrm{H}}^{\mathrm{e}} = 1.15$$
$$r_{\mathrm{H}}^{\mathrm{h}} = 0.72,$$

for electrons and holes. Reference [40] gives a comprehensive presentation of this subject.

4 PIXEL DEVICE DESIGN FOR IRRADIATION STUDIES

Motivated by the Technical Design Report [15] a pixel device was prototyped aiming at various uncertainties. Numerous open questions such as resolution or the use of high (5-20 kΩcm)[4] or low (100-500 Ωcm) resistivity bulk material are to be addressed. Initially low resistive material was expected to be more radiation hard. General radiation effects and their consequences to detector performance should be studied on the pixel level. Although no unexpected discoveries are assumed, little practical knowledge with large pixel arrays was reported except for the CCD's.

This section describes the four different designs of a pixel array provided for front end VLSI (very low scale integration) readout electronics. The problems to overcome when accessing large arrays of pixels have been discussed earlier. Therefore the devices designed are limited to 256 pixels, divided in two groups of 128 pixels. They are accessible via bond pads which are placed on both ends of the detector (figure 17).

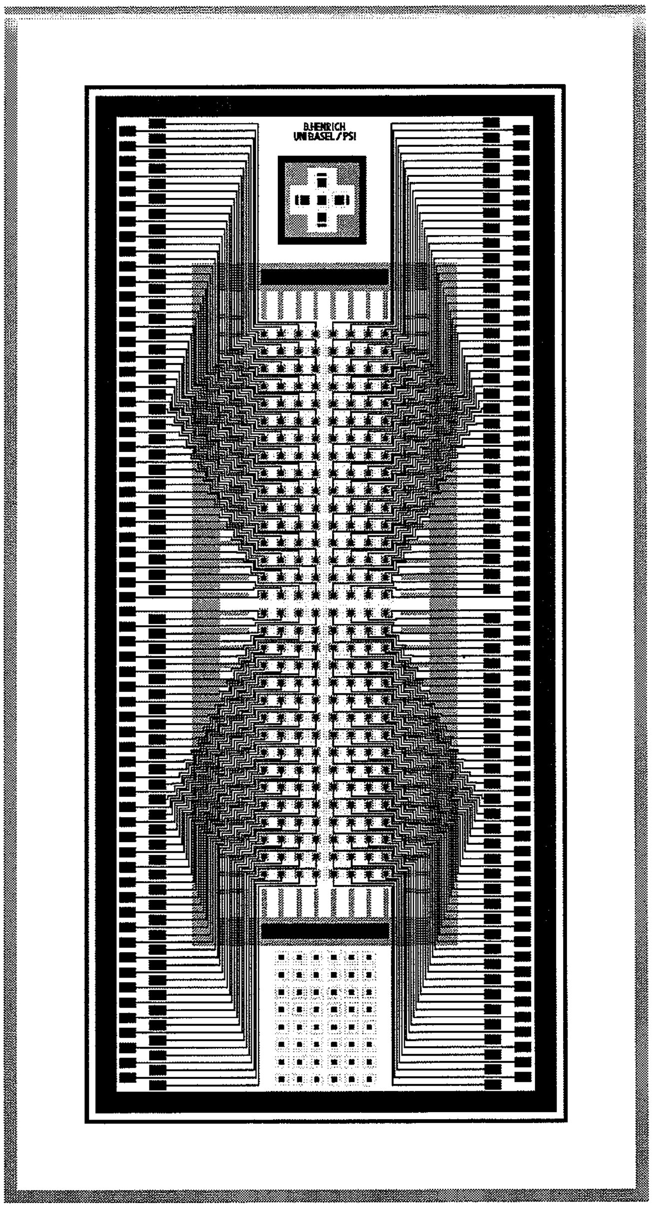

Figure 17: The full layout showing the n-side of the *normal* device

In 1996, prototype pixel designs were submitted on a wafer in a shared submission with the

4. In high resistivity material typically one impurity atom is found per 10^{11} silicon atoms.

silicon strip detector group of CMS [41]. Several n-silicon wafers with high and low resistivities were processed and cut at the Centre Suisse d'Electronique et de Microtechnologie (CSEM). The full layout showing the n-side of the *regular* device is displayed in figure 17.

The two-sided process allowed the implementation of n^+-pixel[5] diodes in n-type silicon which is the preferred method. Due to radiation effects the initially n-type material becomes p-type. Type inversion will occur after a few months of LHC operation, even if anticipated that the full design luminosity is not reached in the first two years. In order to increase the lifetime, running with partial depletion must be accepted which is more suitable for a n^+-pixel readout. After type inversion the depletion region will be on the n-pixel side. This method is also motivated by charge sharing due to the Lorentz effect which is expected to be three times larger for electrons than for holes.

The cell size of $125 \times 125\ \mu m^2$ for the pixels was outlined by the Technical Design Report. In contrast, the size of the n^+-pixel implant was an open parameter and gave room for variations. For the operation of such a detector a p^+-implant on the backside of the sensor is needed which forms the p-n junction before type inversion. By applying a negative bias voltage on the p-side, the depletion region starts from there.

Therefore a double sided process is required which needs more process steps and has a perceptible effect on the price. But it is also needed because of the guard-ring structures for which on the p-side special precautions have to be taken. Diode and other sensor structures must always be surrounded by one or multiple implant rings. The sawing edges represent a region of lattice displacements and high disorder which usually conduct. If the depletion region extends towards these edges an immense increase of the leakage current is measured. Therefore, a multiple guard ring structure of which the innermost ring is on ground potential collects this current and ensures that the potential (because of the applied bias voltage) drops to zero. For the CMS pixel this is required because the cutting edge has to be at the same potential as the n-side and especially at the potential of the readout chips. Without this measure, a potential difference between sensor edge and overlapping readout chip (typically 15-20 μm above the sensor surface) could result in discharges across the gap. The use of p-doped wafers as starting material has been dropped because of this problem although it would allow single sided processing.

a)

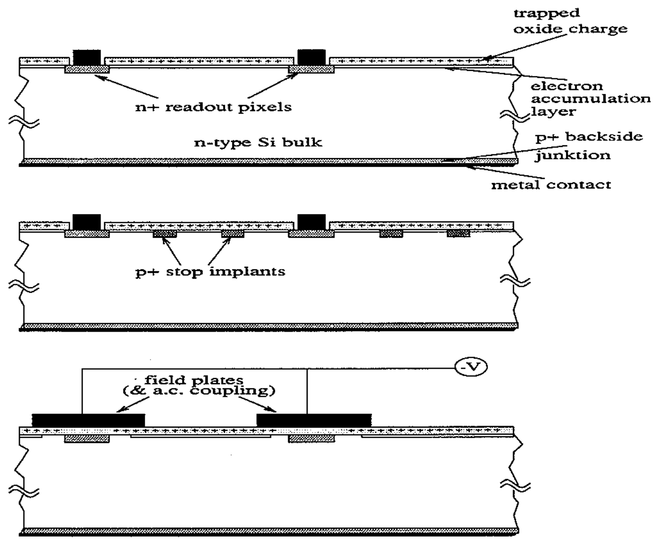

b)

c)

Figure 18: The use of field plates and p^+-stops to break the accumulation layer and provide good interpixel isolation. In a) the origin of the electron accumulation layer is explained. The figures b) and c) represent how this problem can be overcome.

Further precautions have to be taken on the n-side. The omnipresent positive oxide charge

5. Typical doses applied by ion implantation are $5 \times 10^{16}/cm^2$ for boron (n^+) and and $5 \times 10^{15}/cm^2$ for phosphorus (p^+) doping

(section 3.2.1) at the Si-SiO_2 interface leads to a shallow accumulation layer of electrons. If the space charge region from the p-side extends towards the n^+-pixels this layer acts as conductor. The interstrip resistance is of the order of a few kOhms. In figure 18 this process and the two possibilities to overcome this problem are illustrated.

The accumulation layer can be interrupted by an additional p^+-implant ring (p^+-stop) surrounding each pixel individually (figure 18b)). Another option shown in figure 18c) is the introduction of field plates [42]. A suitable voltage applied to the field plates pushes the electrons from the surface. Both methods have their advantages and disadvantages. For technical reasons and based on measurements (see section 6) for the CMS pixel detector the p^+-stop ring method is preferred.

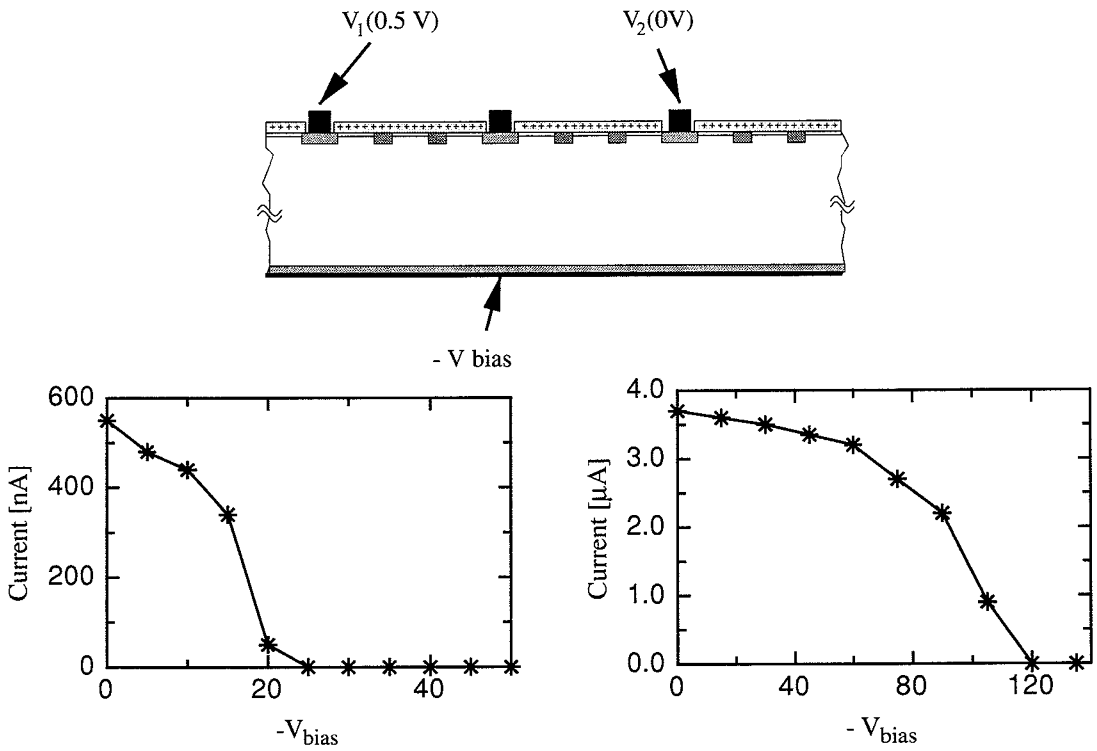

Figure 19: Interpixel current measured between V_1 (=0.5 V) and V_2 (=0 V) as a function of bias voltage (sketch above). The two graphs represent the measurement on two samples with initially low resistivity (on the left) and high resistivity (on the right) material.

Figure 19 shows the current measured between two pixels (potential difference 0.5 V) in dependence of the applied bias voltage. The current drops to zero when the depletion region has reached the n-side. The scale of the axes and the drop of the current at the different bias voltages is explained by the different resistivities of the bulk material. It is reported that the floating p^+-stop rings begin to take up voltage different to that of the n^+-implants once the depletion region has reached the n-side. This voltage increases linearly with the bias voltage [43]. After type inversion the p^+-stop is no longer determined by reachthrough and is essentially an ohmic contact to the bulk. No difference is observed between a common p^+-stop grid and individual p^+-stop rings after irradiation [44].

When planing the layout of a micro structure a catalogue of design rules characteristic for each detector manufacturer has to be taken into consideration. A design rule can be understood as a safety margin and violation has usually serious consequences on the yield. If, for example two parallel strips have too small spacing, short-circuits can occur with a certain probability. This handicap has additional implications on the design of a sensor and is also responsible for the final appearance as shown in figure 17. The layout of the pixel prototype sensors comply with the design rules of CSEM.

4.1 Description of pixel design parameters

Before each design is described individually some common particularities are mentioned. Most of the space is used for the metal rooting. In order to access each pixel they are arranged in eight rows with columns of 32 pixels. The attached metal lines end in bond pads on two sides of the detector suitable for front end, 128-channel wide, readout chips.

The active area of the pixel array is 1×4 mm^2 (compared to the over-all space of 4×8 mm^2). In order to ensure that the outermost pixels senses the same potential as the others the whole array is enclosed by a generous n^+-ring with teeth extending to them (see figure 21). Under bias this ring must be contacted to the same potential as the included pixels. This guarantees a uniform distribution of the space charge region over the pixels which becomes crucial in case of irradiation.

Contents of the following sections are closer descriptions of the individual designs. A brief overview of the four different structures is given:

- Regular device, including knowhow and advices from reference [45].
- Staggered-regular device, where one half of the pixels are staggered like the bricks in a wall. This detector is provided for resolution studies.
- Test device with variations in p^+-stop design and in the n^+-pixel implants.
- *Strixel*-device, stripped pixels following the ATLAS pixel design (also dedicated to beam test studies).

4.1.1 The regular design

One attribute of the regular design is its uniformity. All 256 pixels have the same width of implants. This width is chosen according to the experience and knowledge of references [45] and [46]. It is a conservative sensor in order to optimise the known influences of the design parameters to the performance. Rather than the pitch (centre to centre distance of two pixels) the gap is the determining parameter. A detector segmented into pixels can be regarded as a single plane detector with disturbances formed by the gaps where higher bias voltage reduce these disturbances. It is also the gap which determines the potential and electric field distribution. As a general rule: by projecting the gap length into the substrate the electric field lines become equal and uniform to those of a large plane [27]. Large gaps have the advantage of smaller interpixel capacitance and the detector has an improved position resolution (because of slightly longer collection times). Detectors with small gaps have better charge collection efficiency (they show larger signals). The gap (60 μm) of this design is therefore of the same order as the width of the n^+-implant (65 μm).

Here, the n^+-pixel is surrounded by an individual p^+-stop ring whose width is well within the design rules in order to avoid short cuts between these two implants.

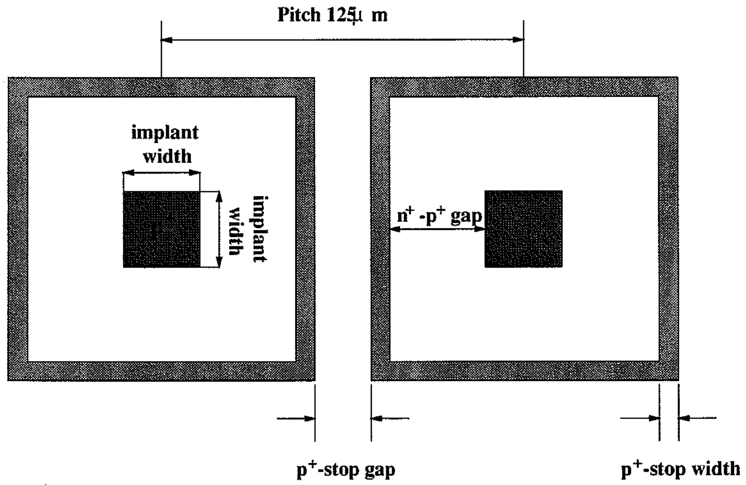

Figure 20: Explanation of the design parameter expressions.

Table 2 summarises the main design parameters. The implant width is the broadness of the n^+-pixel. With p^+-stop width the broadness of the insulating ring is described while n^+-p^+ gap denotes the space between the pixel and its p^+-stop ring. Finally, p^+-stop gap defines the void between two adjacent insulator rings. The meaning of the design parameter expressions is explained in figure 20.

Implant width	p^+-stop width	n^+-p^+ gap	p^+-stop gap
65×65 μm^2	10 μm	15 μm	10 μm

Table 2: Main design parameters for the regular device. The meaning of the names cited in the table are described in the text.

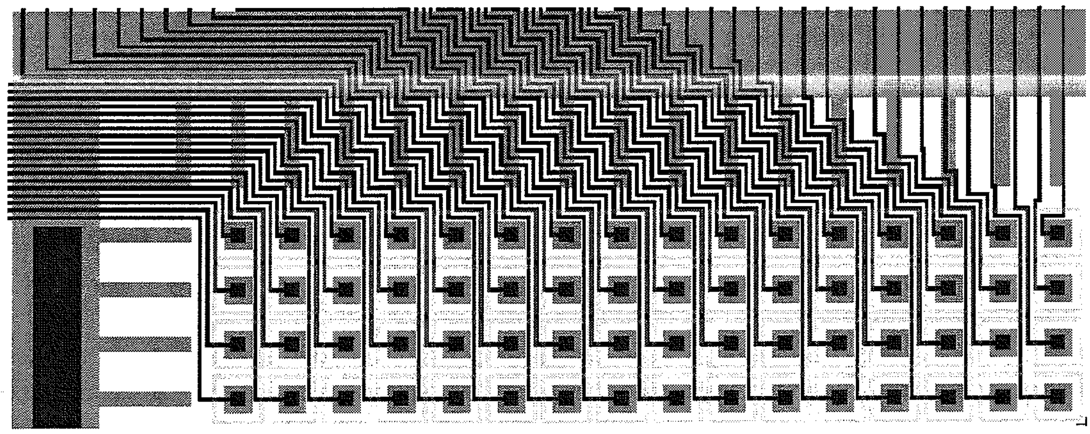

Figure 21: Upper edge of the detector with the black metal layer while the dark grey denotes the n^+. The p^+ layer is described by the light grey pattern. The array is surrounded by a n^+-ring with extending teeth towards the pixels.

Figure 21 gives a detailed view of one edge of the pixel array. The black lines are the metal layer with the rooting of the pixel signals to the bondpads. Dark grey areas stand for n^+-implants while the p^+-implants appear in lighter grey. The surrounding n^+-implant with its extending teeth can be seen well in this figure.

The measurements and results described in section 6 are achieved using sensor prototypes with the regular design.

4.1.2 The staggered/unstaggered design

In this design the implant width is slightly enlarged to 75×75 μm^2. It is mainly dedicated for resolution studies distinguishable in two different regions. In one area the pixels are arranged regularly as before (section 4.1.1). In the other region the odd rows of pixels are staggered by half the pixel size. In the detail view of figure 22 it can be seen that every other pixel column but one contains seven instead of eight pixels with one connection floating.

This design was used in a CMS beam test to investigate resolution differences arising from the staggered and the unstaggered regions [47]. The conclusion from this beam test is that in the staggered region in fact a slightly improved spatial resolution is observed. Because of the staggering the collected charge is more often distributed among three pixels leading to an improved determination of the initial impact position.

Implant width	p^+-stop width	n^+-p^+ gap	p^+-stop gap
75×75 μm^2	5 μm	15 μm	10 μm

Table 3: Design parameters for the staggered/unstaggered device.

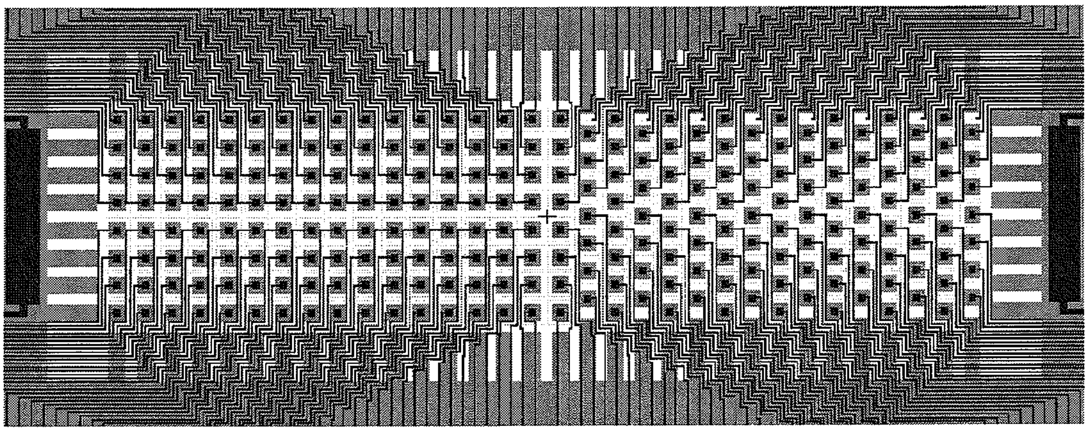

Figure 22: Detail view of the staggered/unstaggered sensor showing the transition between the two regions.

The reduced signal due to radiation effects (reduced space charge region and trapping) charge spread over more than two pixels is not strived for since the signal could drop below the readout threshold. In addition this staggered design would mean an extra expenditure for the readout chip architecture. Therefore, further studies on this design are no longer pursued.

4.1.3 The test design

This device is used to test differences in the performance due to variations in the design parameters. Figure 23 is a map containing the regions with different designs whose parameters are summarised in table 4.

On the right half of figure 23 it is distinguished between four sections of 8×4 pixels with different n^+ widths varying between $25 \times 25\ \mu m^2$ and $95 \times 95\ \mu m^2$. Therefore the gap between two neighbouring pixels changes as well.

The left half of the device has two sections with 8×4 pixels (n^+-p^+-p well and p^+-stop grid) and a region subdivided into sections of 4×4 pixels (p^+-stop variations 1-4). The n^+ width remains constant and only the distance to the p^+-stop ring (n^+-p^+ gap) and the width of the ring itself is changed. The parameters are listed in table 4.

In the section p^+-stop grid the pixels have a common grid-like p^+-implant. Although no differences are observed in the performance of irradiated silicon strip detectors using separated and individual p^+-stop rings [43] an influence on the interpixel capacitance is expected [15].

The n^+-p^+-p region is a test section to investigate an unconventional design which is traced back to an idea for a novel tracking device [48].

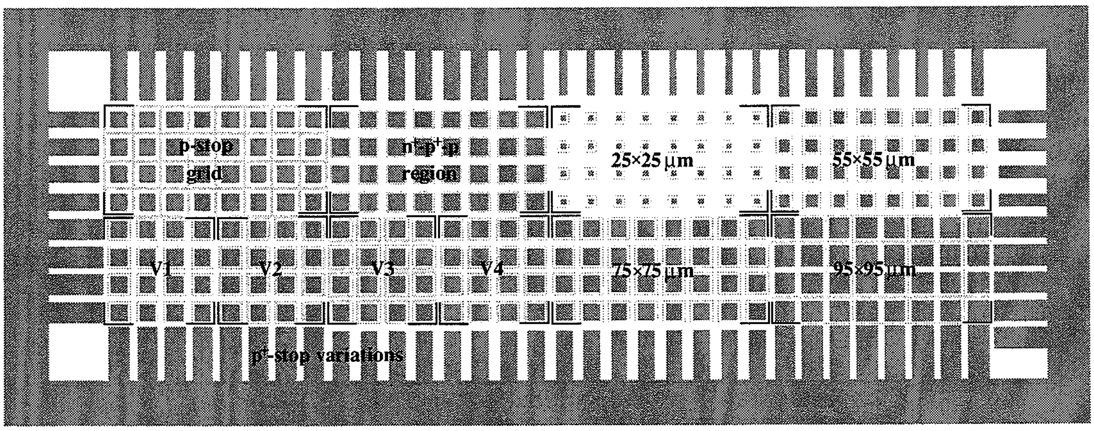

Figure 23: Map of the regions with different design parameters. The metallisation mask is removed on this layout.

Design region according to figure 23	Implant width	p^+-stop width	n^+-p^+ gap	p^+-stop gap
25 μm region	25×25 μm^2	5 μm	10 μm	70 μm
55 μm region	55×55 μm^2	5 μm	10 μm	40 μm
75 μm region	75×75 μm^2	5 μm	10 μm	20 μm
95 μm region	95×95 μm^2	3 μm	10 μm	4 μm
p^+-stop V1	75×75 μm^2	10 μm	5 μm	20 μm
p^+-stop V2	75×75 μm^2	10 μm	10 μm	10 μm
p^+-stop V3	75×75 μm^2	12 μm	5 μm	16 μm
p^+-stop V4	75×75 μm^2	5 μm	10 μm	20 μm
n^+-p^+-p structure	75×75 μm^2	85×85 μm^2	no gap	30 μm
p^+-stop grid	75×75 μm^2	10 μm	20 μm	no gap

Table 4: Listing of the design parameter variations according to the map given in figure 23.

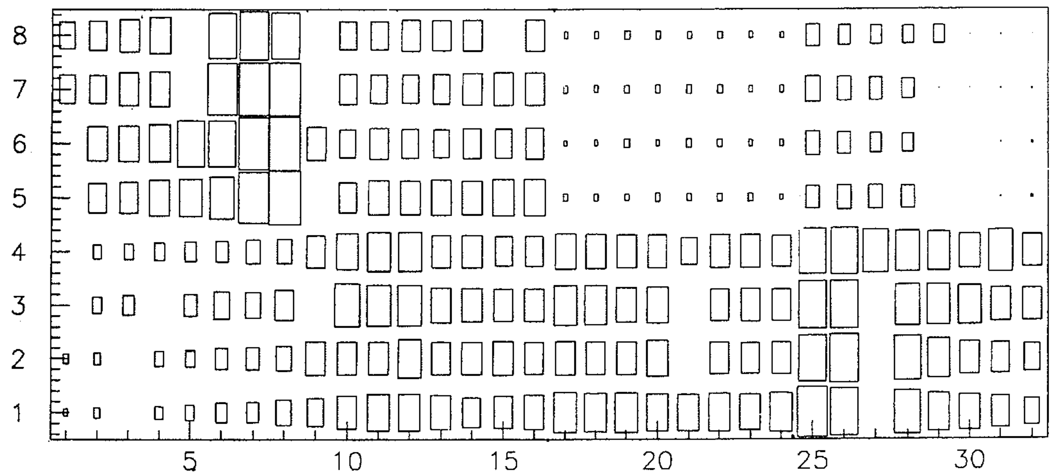

Figure 24: Acceptance or charge collection efficiency of the various regions described in table 4. The missing pixels are short cuts. The missing region in the upper right edge of the picture is a disconnection due to a scratch on the surface cutting the metal lines.

In a beam test with the grazing angle method (see section 5) this device was uniformly illuminated in order to investigate the effects of different design parameters on the performance (such as charge collection efficiency).

Comparing the pulse heights which are expressed by the widths of the boxes in figure 24 one finds that the design parameters indeed have an effect on the charge collection efficiency. The regions in figure 24 are related to the regions outlined in the map of figure 23. As predicted the best charge collection efficiency is achieved with the largest n^+-implants; vice versa the worst with the smallest pixels (25×25 μm^2). On the section with the implant size of 55×55 μm^2 some pixels are missing. A scratch on the sensor surface has disconnected them from the readout. The general observed narrowing of the boxes in the diagram is not induced by the implant variations. This slight focusing of the roads towards the end of the rows is caused by the trigger diodes. Coincidences in the trigger diodes are obviously more frequently created by particle impacts located in the middle of the sensor.

More subtle is the interpretation of the effects observed on the left of figure 24. The acceptance of the pixels insulated by the p^+-stop grid is good while the pixels from the n^+-p^+-p section show less signal. The p^+-stop variations also show different effects on the charge collection efficiency depending on the design.

4.1.4 The strixel design

The fourth device is motivated by the pixel architecture of the ATLAS pixel detector. With a pixel size of 50 μm (in r φ)×300 μm (in z) and a digital readout ATLAS pursues a philosophy different from the CMS pixel detector. In the project phase of the detector this geometry was also in discussion as an option for the end cap configuration.

On this structure, like on the device shown in section 4.1.2 a staggered and an unstaggered region are at disposal. Although the stripped pixel (strixel) geometry of 27 μm (r φ)×216 μm (in z) differs from the ATLAS design the achieved resolution can be extrapolated and compared to the one achieved with the staggered/unstaggered pitch pursued by CMS. Besides position resolution, signal to noise, leakage current, interpixel capacitance and the overall performance after irradiation are of particular interest. The design parameters are listed in table 5 and a detail of the transition between the staggered to the unstaggered region can be seen in figure 25.

Implant width	p^+-stop width	n^+-p^+-implant gap	p^+-stop gap
27×216 μm^2	5 μm	10 μm	5/6 μm

Table 5: Design parameters of the strixel device

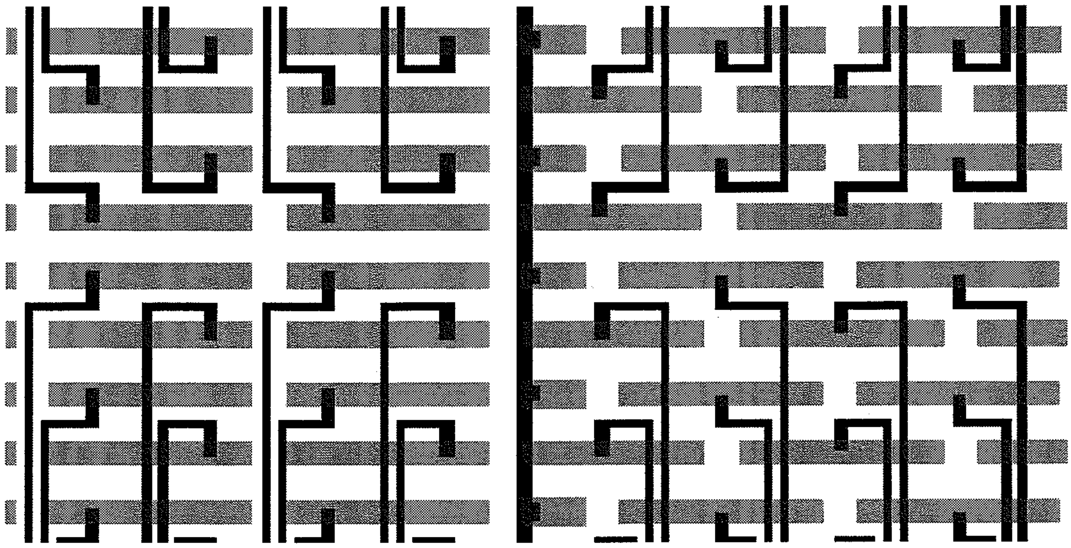

Figure 25: Detail view of the transition between the staggered and the unstaggered region. In order to avoid empty spaces, additional implants which are connected to the guard ring are inserted.

In tests, violations of the design rules were observed leading to a partial loss of pixels in the staggered region. This structure was not tested any further because the main focus is on the investigation of squared pixels which is the preferred geometry for the CMS pixel detector.

4.2 Structures for the characterisation of the pixel performance

Figure 26 shows various test arrays which are additionally enclosed on the sensors. Most of the structures are pixels equal in design and represent an excerpt the of sensor pixel array. One central pixel is surrounded by its four adjacent pixels provided with metal pads for being scrutinised with a probe station.

These structures aim at important information about interpixel resistivities, pixel leakage current and interpixel capacitance. Unfortunately the irradiated sensors which are subject to long term studies could not be removed from their support frames without being destroyed. Therefore tests on these structures were not further performed.

Before irradiation, the left test structure from the centre of figure 19 was used to measure the interpixel resistance as function of the applied bias voltage (see figure 19. On the right of

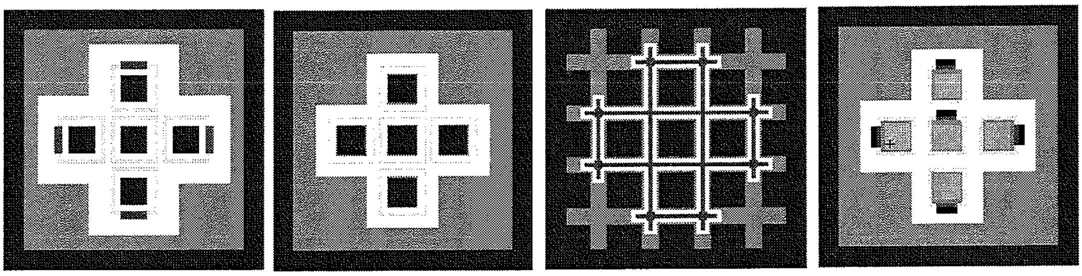

Figure 26: Test structures for measuring the detector performance.

figure 26 a n^+-p^+-p-well is shown which could be used for testing the idea of a self amplifying pixel structure. Therefore, an additional contact provides the connection to the p^+-implant.

The from the centre of figure 26 the right structure and the left test array provide measurements to determine differences between individual p^+-stop rings and a common p^+-stop grid design.

5 PERFORMANCE OF IRRADIATED PIXEL DETECTORS

One important parameter characterising the radiation damage caused in silicon detectors is the effective doping concentration N_{eff}. Knowing the reverse bias voltage V_{bias} needed to fully deplete the detector with a thickness d, the effective doping concentration it is determined by equation (3.7).

The capacitance voltage (C-V) measurement is the standard technique to measure the depletion voltage. It works even if full depletion of the total detector thickness fails because of junction breakdown. The capacitance per unit area is given by $C = \epsilon/d$ [19]. The capacitance reaches its minimum, when the detector is fully depleted. To determine the depletion voltage the C-V curve can be fitted to a power law relation $C = aV^b$ extrapolating the minimum capacitance. Before irradiation the profiles of the C-V curves are independent of the measurement frequency. After irradiation a strong frequency dependence is observed [49]. The defect states produced have long charging and discharging times and cannot respond to the ac-signal of the capacitance meter at high frequencies [36]. Therefore the slope of the C-V measurement cannot unreservedly be used to extract the doping concentration.

The problems to determine the depletion depth of irradiated detectors unambiguously led to a new measurement method. In the following it is called the grazing angle method. (Although this method works with any detector segmented into pixels, the test sensors described in section 4 with 8×32 pixels are ideal devices.)

5.1 Basic idea and concept of the grazing angle method

The principle of this idea is most likely comparable to measurements probing the depletion depth using a LED light spot or an α-source. Both techniques place an amount of energy at certain depths of the n- and p-side, respectively, and analyse the charge collected at the strips (or pixels). A disadvantage of the method using the α-source is that the amount of charge created is not reliably predictable. The LED method fails to be a real 'three dimensional light spot' probing the detector at different depths. The creation of electron-hole pairs falls exponentially with increasing depth and is dependent on the wavelength.

The grazing angle method uses minimum ionising particles (MIP's) which transverse the detector under a very shallow angle producing a large amount of electrons and holes along its trajectories. The presence of a strong electric field prohibits a recombination and forces the electron-hole pairs to drift into different directions along the field-lines to the surface. Because of the segmentation on the n-side, the collected charge of each pixel corresponds to a certain detector depth in which the charge was created. In other words, the particle track graze through the sensor. Knowing the tilting angle and the effective path length (given by the row of pixels that show a signal) the width of the depletion region can be obtained [50].

Under LHC conditions, type inversion and therefore operation of a partial depleted sensor becomes inevitable. A reasonable equilibrium between depletion depth and bias voltage has to be determined. On the one hand a maximum depletion depth is strived in order to achieve maximal signal heights. On the other hand too high bias voltages cause junction breakdown destroying the detector. The grazing angle method measures this correlation in a safe bias range determining the effective depletion voltage by extrapolation. One important result is that the pixel sensors at CMS will be operated at 300 V. The breakdown voltage must be in excess of 500 V for detectors irradiated finally with up to 6×10^{14} hadrons/cm^2 in order to avoid micro discharges.

The pixel sensor prototype described in section 4.1.1 is an ideal device for tests with tilted tracks. Minimum ionising pions of 450 MeV/c are used to penetrate the sensor at a small angle ($\sim 8°$). Hence, the pion transversing rows of pixels acts like a 'three dimensional light spot' probing the detector at different depths (in steps of 17.5 μm/pixel by a grazing angle of 8°).

Figure 27 shows the schematic of a pion transversing the test detector in the unirradiated (left) and in the irradiated case (right) with the corresponding expected signals (upper curves). In the unirradiated case signal generated at the very end of the transversing particle is expected

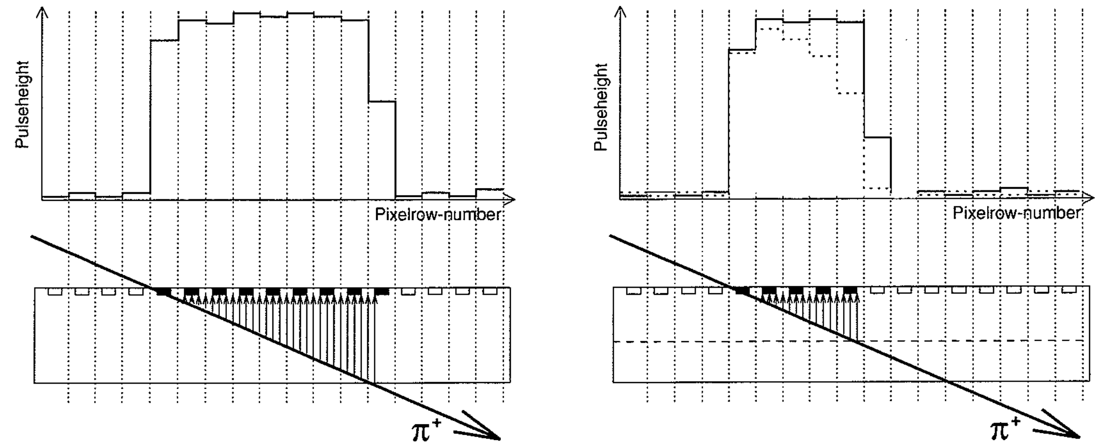

Figure 27: Minimum ionising pions of 450 MeV/c graze the pixels at an angle of 8° (the two bottom figures). Left: expected signal response for an unirradiated device. Right: signal response expected for an irradiated device. The outer curve corresponds to the idealistic case without trapping and the grey curve shows the signal anticipating trapping effects.

to be collected at the pixels. Knowing the exact thickness of the sensor the grazing angle of the particle can be determined by the length of the pixel row (forming a street) which show a signal. In the irradiated case a similar behaviour is expected with less pixel in the row showing a signal. Anticipating the effect of charge trapping an additional charge loss occurs towards the end of the street.

The indisputable advantage of this method is the simple trigonometric relationship between the street length (pixels with signal) and the depletion depth. Apart from that, this method is still reliable if the sensor is degraded by radiation damage. In addition effects such as the charge loss due to a reduced space charge region and charge trapping become distinguishable.

5.2 Measurement setup description

This section provides a detailed overview of the equipment and electronics applied for this grazing angle method. Figure 28 shows a schematic of the setup used. Power, steering and readout

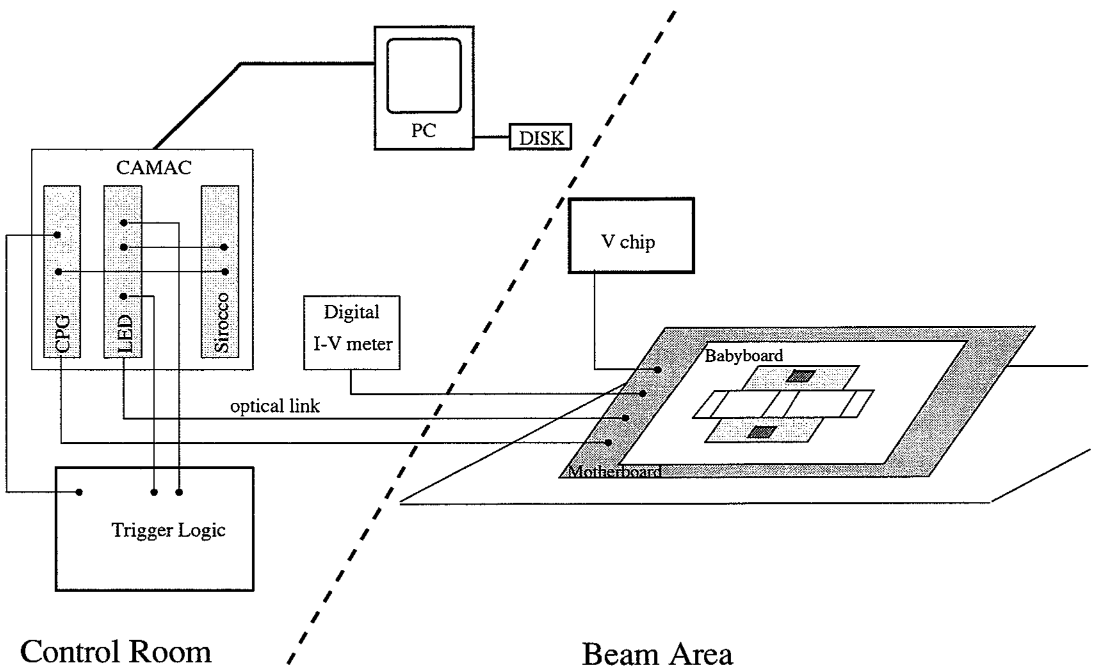

Figure 28: Schematic view of the experimental setup as described in the text.

signals come in long cables from the shed housing the electronics rack where all the signals for the readout chips and the trigger logic are generated. Data storage and code generation is done with the same computer. A CAMAC rack is used as an interface between the readout electronics and the computer. It contains a SIROCCO[6] for receiving and digitisation of the analog data. A CPG[7] generates the digital control sequences for the readout chips. The LED converter transforms the optical analog data back into electrical pulses.

The sequencer (CPG) is loaded (from the computer via fast bus) with a control program and communicates through a specific bit-pattern with the two APC's[8]. This pattern has two loops: a data taking loop and a readout loop. The readout loop runs continuously with a CPG clock frequency of 20 MHz and enables the APC's to amplify the charge from the pixels and integrate over a time of 1 μs. If no trigger signal is received, the data is erased. In case of a trigger the readout loop is activated. Subsequently, the integrated signals of all 256 channels are transferred to the SIROCCO. The bit-pattern code addressing the switches on the readout chip is generated on the computer using a conversion program. Both, SIROCCO and CPG are addressed, initialised and loaded by computer generated codes. It is a highly adaptable system which enables to perform changes on the readout process even during runtime periods.

The motherboard houses the necessary electronics (see section 5.3) and the pluggable pixel sensors attached with its readout electronics (baby board). It is placed on the platform of a beam scanner tripod tilted by a small angle. The beam scanner is remotely movable along two axes and by scanning for the maximum counting rate on the trigger diodes, the optimum position within the pion beam ($\sim$5 cm in diameter) is easy to determine. A vertical and a horizontal scan of the beam profile can be found in figure 38.

Cooling is needed in order to reduce the leakage current and to suppress the reverse annealing. A polystyrene box is equipped with two Peltier elements. Their cool side is dispensed trough aluminium sheets into the box while the hot side is water cooled. Temperatures of less than -5°C could be achieved even while the electronics inside is running. The cold air dispensed by the aluminium is dispersed by convection only. Sometimes ice was formed and the lid of the cooling box get stuck. As prevention a shallow flow of Nitrogen into the box generates a humidity free atmosphere and slight overpressure. This cooling principle is very robust and maintenance-free.

The baby board

A delicate issue is the location of the trigger diodes. In order to achieve a high hit efficiency they should be placed as close as possible to the detector with a minimum overlap. For variable grazing angles they should be adjustable. Figure 29 shows the solution of this problem. The sensor, almost

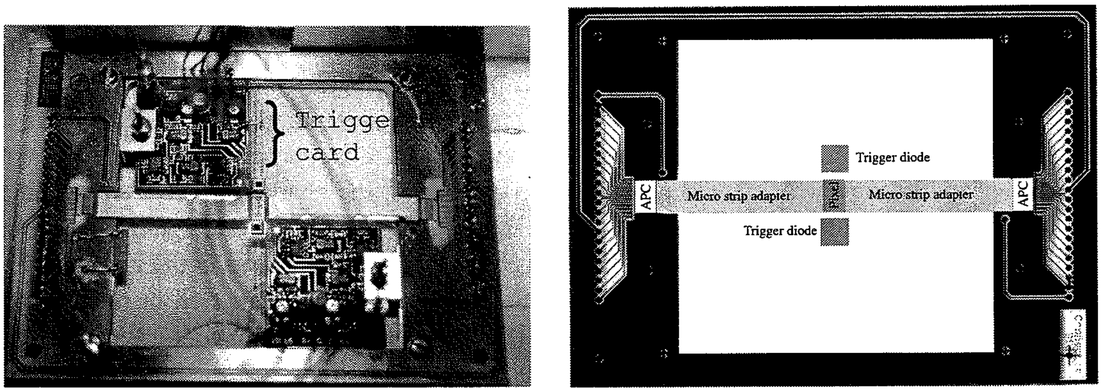

Figure 29: Left: Picture of the entire baby board situated within the polystyrene box. Right: PCB-layout with the signal supply for the APC128's and symbolic inscription of the micro strip placing and the test detector.

6. **Si**licon **R**ead **O**ut **C**AMAC **C**ontroler
7. CAMAC **P**attern **G**enerator, programmable digital bit generator
8. **A**nalog **P**ipeline **C**hip with 128 amplifying channels [52]

levitating, is glued between two ceramic micro strip adapters. On the ceramic, small gold strips bonded to the pixels conduct the signals to the APC chips on a PCB (baby) board. This method of construction is chosen because the readout chips are non-radiation hard. In that way the readout chips can be shielded against radiation (even readout is possible) while the sensor is irradiated. The trigger cards with the diodes are installed on an aluminium frame such that they are tunable in hight. The frame can be easily attached to the baby board ensuring additional stability.

The such prepared baby board finds place in the cooling box plugged via feedthrough connectors to the motherboard. This compact technique with plug and unpluggable baby boards facilitates the replacement of several test detectors during a beam test period.

5.3 Read out electronics

Because of the complexity of the system a detailed description of the electronics is given in the following. The motherboard represents the interface between the steering signals from the control room and the readout chip. An electrically separated circuit processes the incoming steering signals in order to prevent disturbing noise pickup. The APC readout chip is a development dedicated for the micro strip vertex detector of the H1 experiment at HERA (electron-proton collider at DESY). It was developed at PSI where the knowhow on the chip is still situated. The choice for this readout chip is therefore obvious. The trigger cards house a circuit which was designed for measurements on test diodes [51]. It was slightly modified for this purpose.

5.3.1 The motherboard

The motherboard comprises all the necessary electronics to process the digital steering signals and the analog/digital power supplies which are needed to operate the two readout chips. It is a design of the electronics group in Basel. The layout of the circuit is shown in figure 88 in appendix A. In this application twelve digital steering signals are used to operate the APC128. These signals are processed in opto-couplers which electrically separate the signals from the CPG and refreshes them for the readout chips.

The analog power supply (V_{ana}) is needed to drive the 128 analog preamplifiers on the APC. It is usually restricted to 40 mA (at 1.9 V) but optionally a current of up to 80 mA is possible. The digital power (V_{dig} 0-5 V) supplies the digital pipeline and the sequential readout circuitry. In order to extract the inevitable noise background from the bias voltage supply a simple RC-filter on the motherboard is installed.

5.3.2 The readout chip APC128

For the HERA micro strip vertex detector a specialised readout chip, the APC128 (128 channels) [55], was fabricated in order to have a dead-time free readout even at a bunch crossing rate of 10.4 MHz. Due to trigger delays of the experiment an analogue event pipeline was designed to store the last 32 hits. This pipeline following a charge sensitive preamplifier is realised in the form of switched capacitors that memorise the output voltage. One peculiarity of this chip is the self-reading architecture which is the possibility to disconnect the charge sensitive preamplifiers from the detector signal and re-read its own output signals stored in any of the pipeline capacitors. But this peculiar characteristic as well as the event buffering were not used in the readout of the setup described here. The basic concept of the chip is schematically illustrated in figure 30. Its capabilities are rather misused in this application. All its pipeline capabilities are disabled. And instead of the pipeline capacities (Cp) the latch capacitor (Cl) is used to store the integrated charge. Therefore all the transistor signals that control the pipeline shift register ($S\phi1$, $S\phi2$, SEB and SBI) can be neglected.

Only during the proton irradiation a full readout of all 32 buffers is performed. The rise of the signals originating from the pixels are sampled by the pipeline capacitors. In this configuration the APC is used as a pulse form recorder (see section 5.4 and figure 36).

Each channel consists of a charge sensitive preamplifier. The pipeline capacitors immediately after the amplifiers can be addressed and made ready for data storage or readout by a static

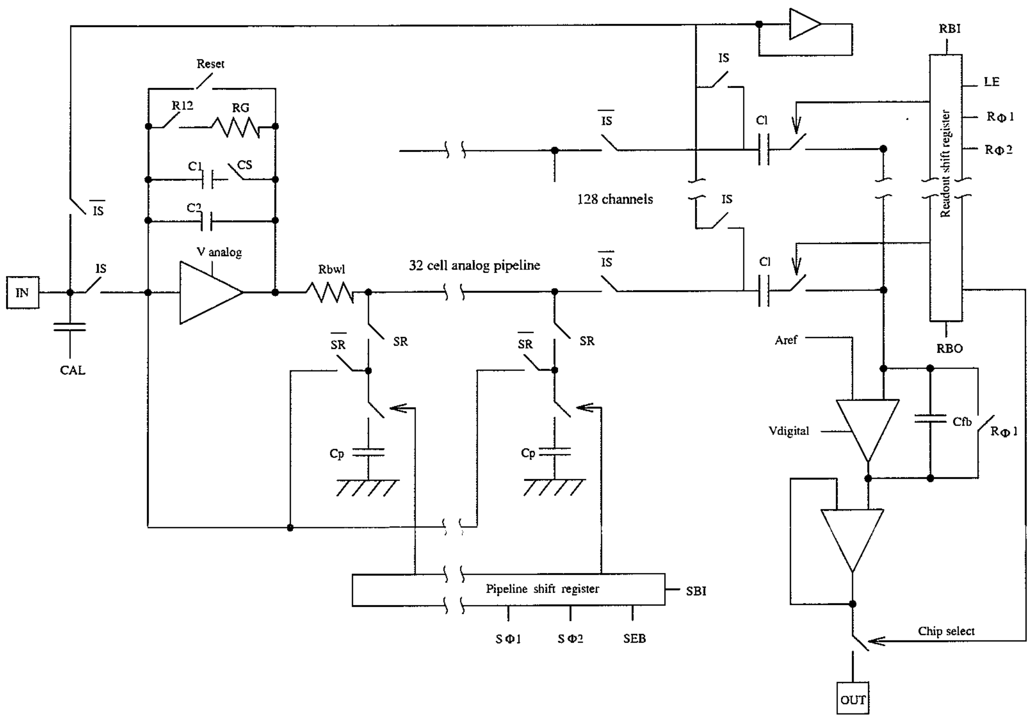

Figure 30: The wiring of the APC128.

shift register. This shift register switched capacitors can be connected for a short time period to the output node of the charge sensitive amplifier and therefore memorise the amplifier output voltage. Besides this sequential connection, the latch enable signal (LE) initiates the latch operation where all these capacitors can be connected or disconnected in common.

During data recording the pipeline is overwritten circularly and the capacitors are filled with new charge. The sequential readout of all channel signals (either of one specific pipeline buffer or of all 32 pipeline buffers) on a chip is done through the latch capacitors (Cl). The here described (and mainly utilised) setup only uses the latch capacities for storing the charge. Therefore the latch operation is performed as soon as the trigger is confirmed disconnecting all capacitors (Cl) and freezing the stored charge. The stored charge is readout directly through the channel shift register without being redirected to the preamplifiers.

In its original configuration the latch capacitor has a threefold function. First, it is needed to decouple the dc working points of the preamplifier from the readout amplifier since they are powered by different voltages. Second, the latch capacitor offers the possibility to subtract any two buffers of the same pipeline before the readout will be performed. Finally, the latch capacitor, together with the readout amplifier, form an additional gain stage before the signals leave the chip. The readout is then done sequentially because the channel readout shift register connects only one channel at a time to a single readout amplifier. This amplifier and the shift register switches are powered by the digital supply voltage (V_{dig}) while only the preamplifiers are supplied with a different voltage (V_{ana}). Ideally, the preamplifier should be fast, have a good noise performance and dissipate little power in order to show good performance. These are requirements which are almost mutually exclusive. In the case of the APC preamplifier a power consumption as low as possible is the main focus which is realised by choosing a single gain stage consisting of an n-FET and a p-FET with both gates connected as input and their gains connected as output (push-pull inverter).

Additional to the sensor a built-in capacitance (CAL) can be used to generate a charge pulse for the preamplifiers in order to calibrate the absolute signal height and for testing the functionality of the chip. This feature is used to obtain the results presented in sections 6.4 and 6.5, respectively.

5.3.3 Trigger diode electronics, logic and timing

The trigger diodes have a size of 2×2 mm^2 and a thickness of 370 μm. Their overlap in size compared to the pixel sensor array causes triggered readout without events. An apparent disadvantage which becomes very useful in the off-line analysis. Because of temporal changing noise pick up and other disturbances in the readout electronics, these zero hit events could be used to update the pedestal values (see section 6.1).

For amplification of the diode signal the same preamplifier stage is used as on the APC128 design. The output of this preamplifier is then connected to an operational amplifier (OPA640) used to drive the readout. This stage is followed by another amplifier (OPA621) which increases the signal by a factor of ten. In order to send the trigger signal through an optical fibre to the data acquisition system a voltage-current conversion is performed using the technique described in [73].

Figure 31 shows the the schematic of the wiring and of the card-layout can be seen.

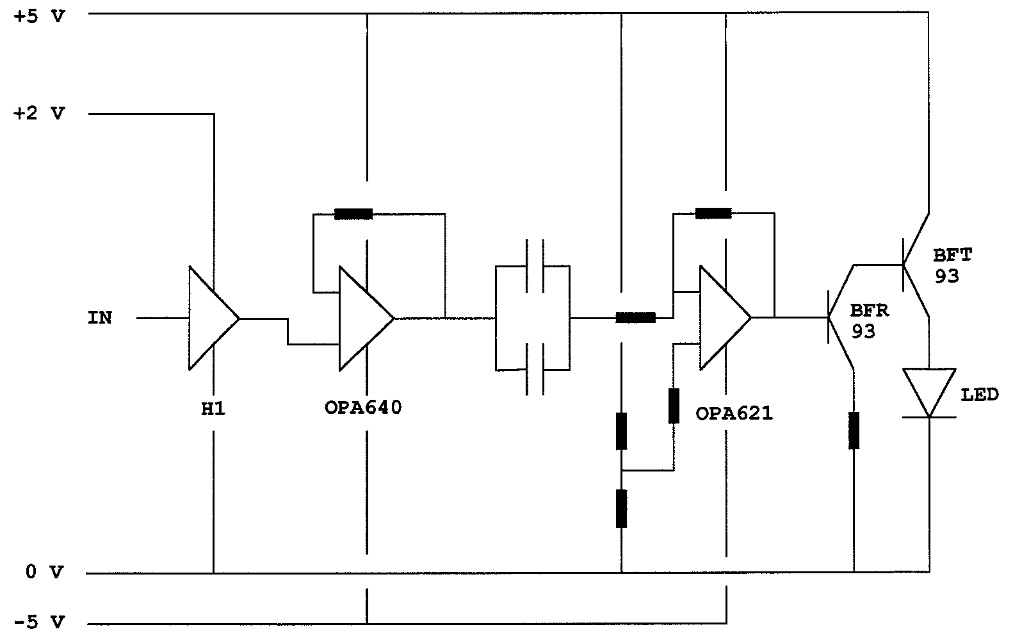

Figure 31: Circuit diagram of the trigger card electronics.

In order to verify the behaviour of the trigger electronics they were initially tested with α-particles (4.48 MeV) from an $^{241}_{95}$Am-source and with a $^{90}_{38}$Sr-source emitting β-particles. The β's with a mean energy of 0.54 MeV traverse the diode and generate a typical Landau distribution while the α's are stopped in the detector and produce a Gaussian shaped signal (see figures 32). Because of the long distance between experimental area and control room, the optical transmission

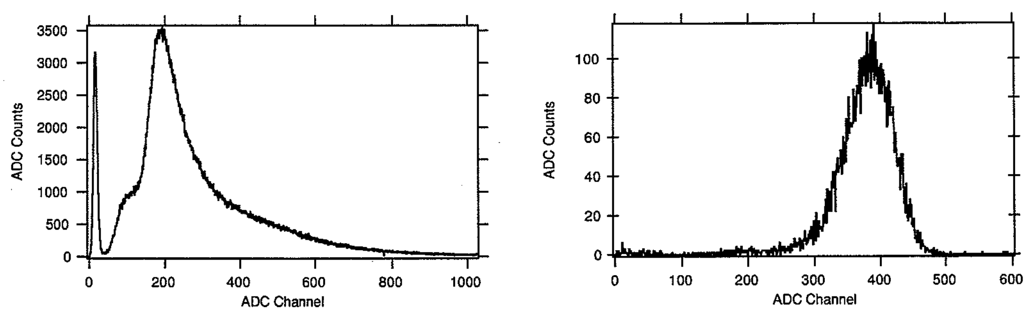

Figure 32: Strontium (left) and Americium (right) spectra recorded with the trigger card diodes.

has a latency of 300 ns. The signals from the trigger diodes are additionally delayed by the trigger logic (~130 ns). The signal confirming an event enables the sequencer to send digital readout commands delayed by 100 ns to the APC chip. The readout chip is programmed such that its integration time does not exceed 1 μs. Then it waits for confirmation or rejection by the trigger logic. In the case of no readout, the signals are erased. In case of readout the data taking is stopped until the signals are sequentially processed by the SIROCCO. When done, the APC is initialised and again in charge integration mode. The timing of the APC control sequences and the trigger logic is carefully tested and verified.

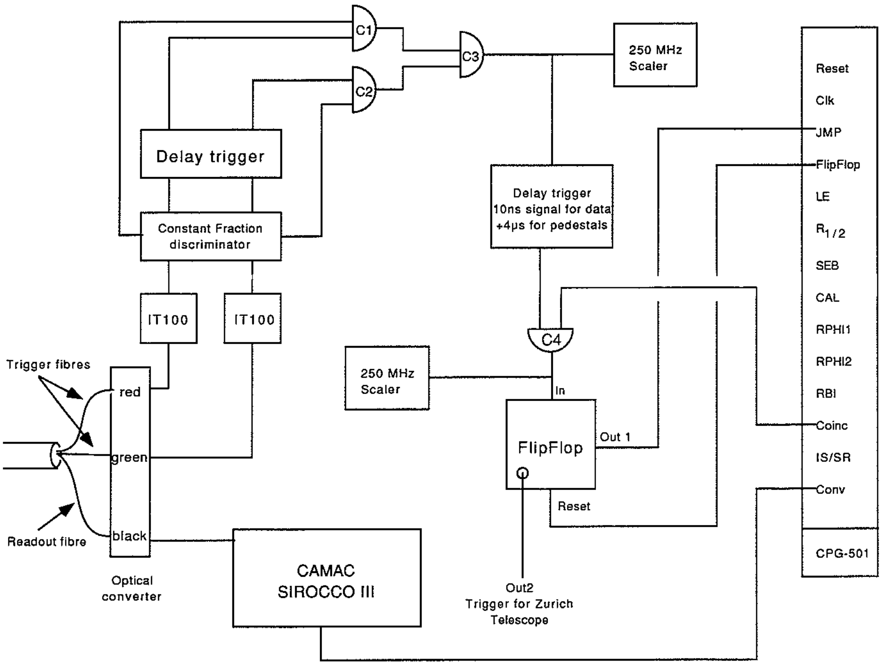

Figure 33: Trigger logic controlling the readout in the beam test using the grazing angle method. In connection with the beam telescope (section 5.7) an additional output signal for this data acquisition system is provided.

Figure 33 shows the trigger logic in detail. The optical trigger signals (marked with red and green) are converted back to electrical signals and decoupled by an inverting transformer (IT100). A constant fraction discriminator (CFT) generates a logical signal when the threshold limit is passed. In order to suppress electronics generated events the signals are split and delayed and then fed back into coincidences (C1 and C2). The output of a third coincidence (C3) generates the trigger. In a delay trigger stage the signal is optionally delayed if pedestal data (event free) is recorded or if a special calibration is active.

The programmable pattern generator provides an artificial signal (Coinc) which indicates that the APC is sensitive. This signal in coincidence with the diode trigger enables a flip-flop stage to send a signal to the CPG. This signal (JMP) enables the pattern generator on the other hand to start the readout sequence. At the same time the SIROCCO receives convert signals (Conv) indicating the sequential pixel data from the chips. After readout the sequence is trapped in an infinite loop and the APC is insensitive until data recording on the computer is finished. When computer and SIROCCO are ready for new events the CPG receives a Reset signal and data taking starts over again.

5.4 Proton irradiation

Five prototype sensors were irradiated with 120 MeV protons while the detector signals were actively recorded. Here the pixels were exposed to protons transversing the detector perpendicular and the readout of the sensor was active at randomly chosen times. No trigger was used and therefore, the setup described above was changed in some respects.

Especially the APC chips are operated in a different mode. The pipeline shift register and the switched pipeline capacitors are enabled in order to record the signal pulse form during irradiation. To avoid thermal runaway the detectors are kept close to 0°C. With a flux of 2×10^8 protons/mm^2/s the total fluence of 10^{15} protons/cm^2 is achieved within one day.

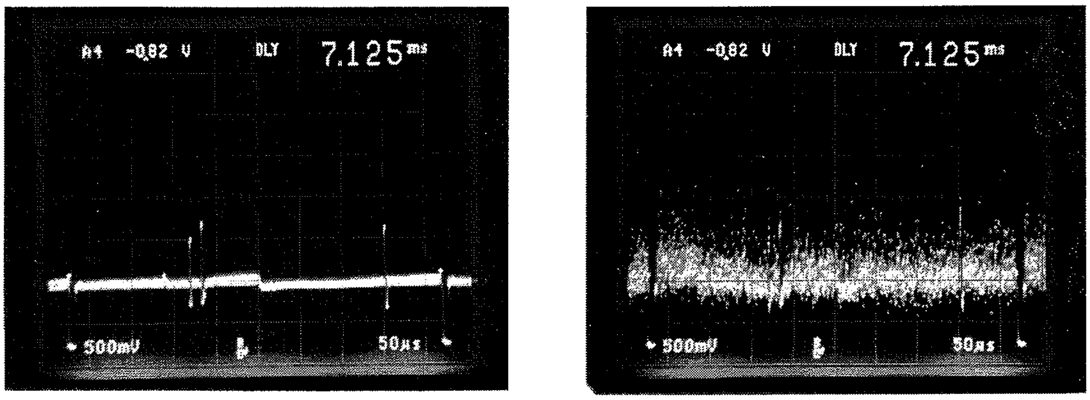

Figure 34: Left: readout of the 256 pixels without beam, right: proton beam on.

Figure 34 shows the readout of the 256 pixels of pipeline buffer number one. The two readout chips are visually separated by the kink. The photograph on the left is the readout with the beam shutter closed. With the beam shutter open the readout looks as shown on the right photograph.

The sensors are initially n^+ pixels in n-bulk material. Before type inversion the bias voltage is easy to determine. As soon as the space charge region is on the pixel side they show a clear signal which is at full depletion voltage. Figure 35 shows the bias voltage as a function of the fluence. After type inversion occurrence of full depletion is decided on the the signal height which is less obvious.

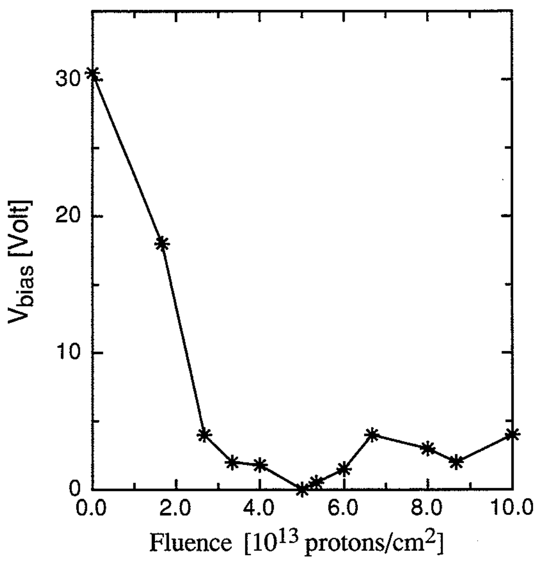

Figure 35: Measurement of type inversion. The bias voltage as a function of the fluence.

The pipeline capacitors are sequentially switched to the output of the preamplifier with a frequency of 10 MHz. In this way each of the 24 buffers of the pipeline (the remaining 8 buffers were used for calibration) recorded a time slice with a length of 100 ns.

During pulse form recording the beam intensity is reduced such that only a few of the 256 pixels would be hit by protons. Figure 36 shows the signal shapes at four different fluences. The preamplifiers are operated such that they integrate the charge of the pixels. Therefore the leakage current shows up as a slope in the output versus the time. Before irradiation, the pixels without hits remain flat with time indicating little leakage current. In figure 36 (left) four pixels show

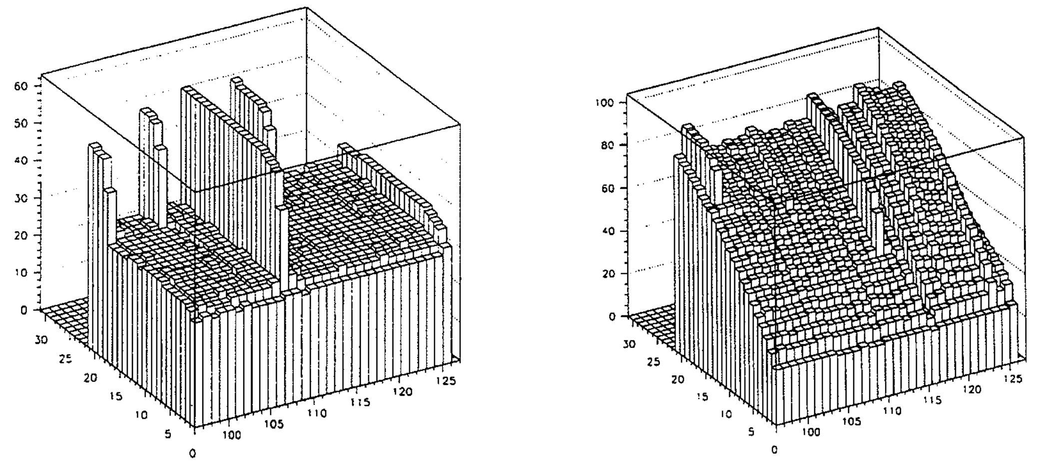

Figure 36: Pixel signal height (vertical height) versus time (2.4 μs) and pixel number (here 0-128). The four graphs represent four different fluences.

clear signals. The signal hight variations are dependent on the deposited energy of the transversing proton. With rising fluence the slope becomes steeper reflecting the leakage current. The remaining eight buffers at the end of the pipeline are used to calibrate the pulse height. With this measure the leakage current for one pixel is determined to 24 nA at 0°C and -225 V bias voltage for a fluence of 1×10^{15} protons/cm^2 (figure 36 (right)). At this fluence the pulse height distribution shows a drop of 20% of its initial value [53].

5.5 Pion irradiation

Another set of three pixel sensors of regular type were exposed to radiation. This time by positive charged pions with a mean energy of 200 MeV were used. The sensors were mounted to their baby frames and connected to the APC's. They were lined up behind each other in a cooling box, kept at 0°C and biased. The beam was narrowed such that its geometry with 2.5 cm (x)$\times$ 1.5 cm (y) was at minimum where the readout chips were located. The peak intensity of the beam was measured to be $1.5 \times 10^{\,9}$ pions/cm^2/s.

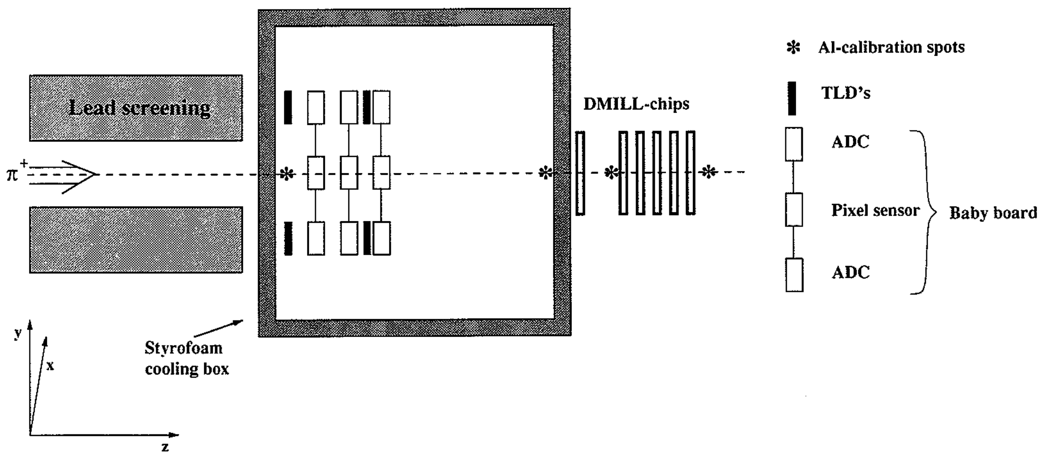

Figure 37: Schematic illustration of the pion irradiation setup. The observation position is from the side

Figure 37 is a schematic illustration of the pion irradiation setup. Aluminium foils are used to calibrate the integrated flux. In addition six TLD's (crystals used for dosimetry) control the integrated flux of the APC's. Although the readout chips are shielded with 15 cm of lead they accumulated radiation from the beam halo and recoiling particles from the DMILL[9] chip carriers which were irradiated in the same setup. These DMILL prototype chips with a 22×30 pixel array and various types of analog amplifiers are also tested on radiation hardness [54]. The chips mounted on ceramic frames, which were not within the cooling box, caused a lot of backscattering and were highly active afterwards.

The integrated fluence of 54 krad of the APC readout chips is within a tolerable limit (~100 krad). The fluences applied to the sensors are

- $3.6\times10^{14}/cm^2$; high resistivity silicon,
- $6.1\times10^{14}/cm^2$; low resistivity silicon,
- $9.0\times10^{14}/cm^2$; low resistivity silicon.

After irradiation continuous cooling is needed in order to suppress the anti annealing process and simulate operating conditions similar to the LHC environment. Therefore the sensors are stored in a refrigerator with a temperature of 2°C. A mobile refrigerator is at disposal for longer transportations (e.g. to the CERN). For the way from the laboratory to the test beam area (~5-10 Min) the sensors were uncooled. First measurements on the sensors using the grazing angle method were performed two weeks after irradiation (see section 6).

5.6 The pion beam profile at PSI

At PSI minimum ionising pions of 450 Mev/c are used to probe the prototype sensors. The pion beam has quite a broad geometry with a diameter of ~8 cm and therefore a slight divergence of the particles is expected.

The measurement of the depletion depth with the introduced method is only reliable if guaranteed that the beam is horizontal with respect to the location of the trigger diodes. Additionally, the divergence of the beam should not be too large. This deviation is measured with the help of a second remote movable tripod. This beam scanner equipped with a small scintillator (2×2 mm) and a photo-multiplier is placed about four meters downstream behind the location of the trigger diodes.

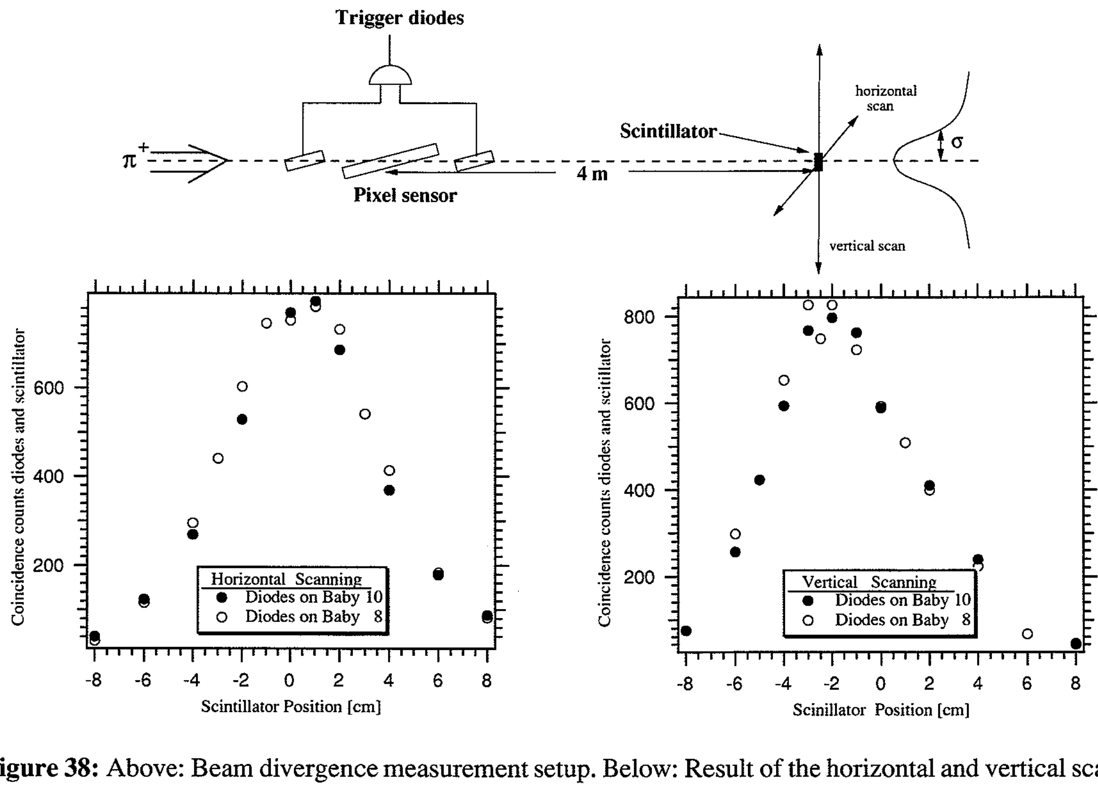

Figure 38: Above: Beam divergence measurement setup. Below: Result of the horizontal and vertical scanning.

9. this is a mixed analog-digital radiation hard process using the silicon on insulator technology

An additional counter registers the scintillator pulses which are in coincidence with the trigger diodes. In order to avoid a counting rate dependent on the beam intensity the counter is stopped when the trigger counter has registered 15'000 events.

Above in figure 38 the measurement with the scintillator setup is illustrated. The horizontal beam scan is presented on the left of figure 38. The result of the vertical beam scan is shown on the right. Zero denotes the absolute position of the trigger diodes above ground. The vertical scan shows a slight deviation with an angle of 0.3° from the horizontal axis. The nearly Gaussian shape of the beam profile with a divergence of 4.5×10^{-3} radians in the vertical and 8.7×10^{-3} in the horizontal axis, respectively has no influence on the precision of the depletion depth measurement.

A more critical value which has more influence on the measurement is the exact determination of the grazing angle (section 5.8).

5.7 Amendment for the Lorentz angle measurement

Large research and development efforts are carried out at various research groups to improve the performances of silicon detectors or develop new kinds of micro strip and pixel detectors. The Lorentz angle measurement was carried out at CERN using a high energetic pion beam with 225 GeV/c. Here, the beam diameter was only 0.5 cm with negligible divergence.

An important step in developing new detector techniques or investigating specific problems is the test under high energy particle tracks. High energetic particle beams are preferably used to keep the multiple scattering low. In order to measure sensor characteristics such as resolution, efficiency and noise it is convenient to have precise information for each track with better resolution than that expected from the device under test. Beam telescopes with high position resolution provide the desired information.

Such a beam telescope was built at the University of Zürich for tests on CMS pixel sensor prototypes. In a first application this telescope was used in combination with the setup and the sensors described above in order to determine the Lorentz angle in irradiated silicon detectors under the influence of magnetic fields [56]. The cited reference is included in this work in appendix B and contains further experimental details and information of the setup described here.

The telescope is composed of eight silicon micro strip detectors with an active area of 3.2×3.2 cm^2 and a thickness of 300 μm each. For a two dimensional track information pairs of two sensors are arranged with a strip orientation perpendicular to each other building a module. Each of these dc-coupled devices has p^+-implants of 10 μm width in n-type silicon. The pitch of the 1279 strips is 50 μm and every second (640 strips) is connected to the input of an analog readout chip. This Viking readout chip (VA2) has a preamplifier shaper architecture with a shaping time of 2.3 μs [57].

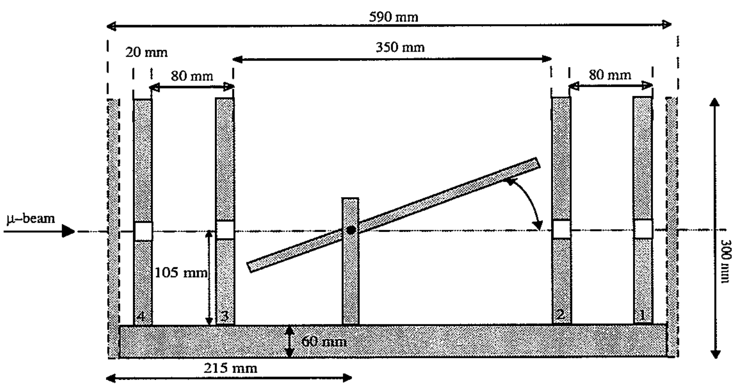

Figure 39: Side view of the telescope detector modules numbered by 1, 2, 3 and 4 and the movable frame for test sensors.

A solid aluminium frame provides space for the installation of the four modules. The sensor under test is placed inbetween. The spatial resolution is measured to be 0.97 μm in x and 1.26 μm in the y direction [58]. A schematic illustration is found in appendix B figure 2 showing additionally the setup of the data acquisition system of the beam telescope. The telescope data acquisition system is based on a Lab-View controlled VME crate which houses two analog to digital converter processing the analog signals. A timing unit provides the digital control signals for the Viking chip.

The pixel sensor with its trigger diodes is mounted on an aluminium frame which is tilted by a certain angle. This frame is located between the in the four telescope layers as indicated in figure 39.

The beam particles transverse the telescope plane perpendicular. When the trigger diodes of the tilted detector indicate a hit on the sensor all eight telescope detectors are read out in parallel.

5.8 Determination of the grazing angle

The measurement of the depletion depth is very sensitive to the adjustment of the grazing angle. A laser plumb bob was developed to measure the tilting angle. The laser spot defining the plumb-line shines trough a window of Plexiglas creating a primary spot. Then it is reflected by the sensor surface generating a secondary spot. By knowing the distance l between window and

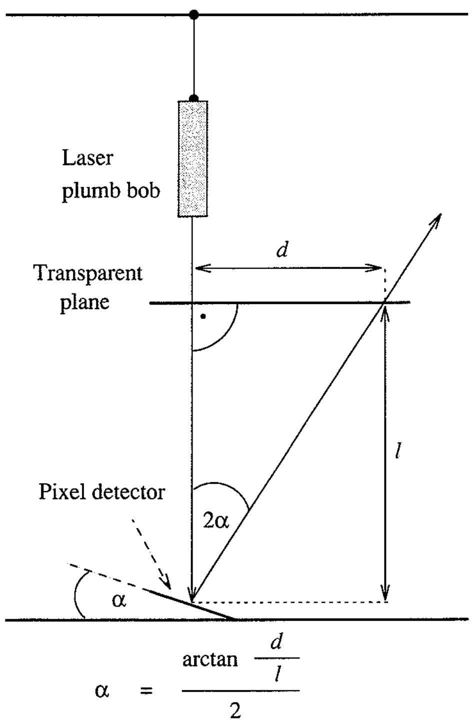

Figure 40: Laser plumb bob method for the measurement of the grazing angle

detector and reading the span d between primary and secondary beam-spot the grazing angle α can be determined with a simple geometric calculation

$$\tan 2\alpha = \frac{d}{l}, \tag{5.1}$$

with a precision of $\pm0.05°$. Using the laser method this angle is determined to be 7.65°. Given a width of 300 μm of the sensor row of 18 pixels is expected to show a signal.

Beam telescope alignment

In a slightly modified setup the grazing angle method is used to determine the drift angle caused by a magnetic field (see next section). A beam telescope is used to increase the resolution of the pixel sensor. The additional track information can be used to calculate the geometric location of the sensor relative to the detector planes of the telescope. A few hundred events are used to determine this relative position by projecting the sensor on the telescope plane. Therefore the coordinates of the pixels x' and y' have to be transformed such that they are projected to the x-y plane using

$$\begin{pmatrix} x' \\ y' \end{pmatrix} = \frac{1}{\sin\theta\cos(\alpha-\beta)}$$

$$\begin{pmatrix} -\sin\phi\sin\beta+\cos\phi\cos\beta & -\sin\phi\cos\alpha-\cos\phi\sin\alpha \\ -\cos\phi\cos\theta\sin\beta-\cos\theta\cos\beta & -\cos\phi\cos\theta\cos\alpha+\sin\phi\cos\theta\sin\alpha \end{pmatrix}\begin{pmatrix} x-x_0 \\ y-y_0 \end{pmatrix}. \quad (5.2)$$

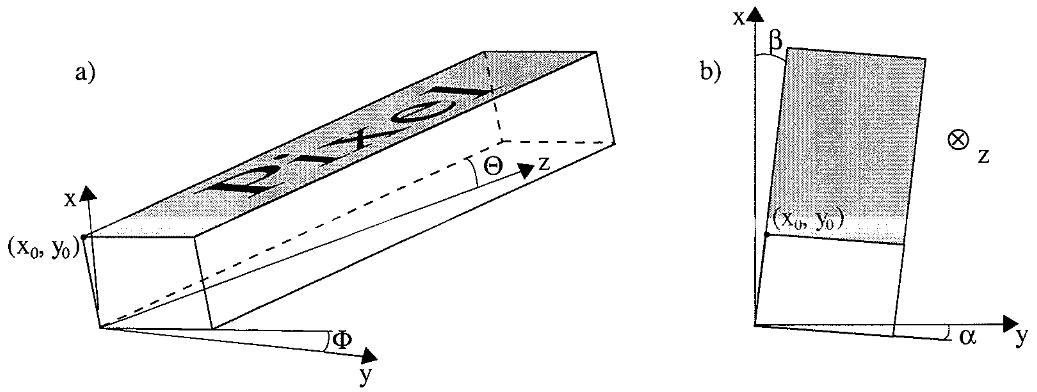

Figure 41: Left: spatial location of the pixel sensor; right: projection of the sensitive area (grey) in the x-y plane.

The lower left edge of the pixel array is denoted with x_0 and y_0 and x, y are the projected coordinates. This mathematical projection and the meaning of the different angles are illustrated in figure 41 which shows on the left the spatial location of the pixel sensor. Here, θ denotes the grazing angle which is usually tagged with α. The projection of its sensitive area (in grey) to the x-y plane is shown on the right in figure 41. The pixel sensor events are individually searched for signals building a chain (the signals which line up in a row). The pixel coordinates defining the start and the end of a street are transformed by equation (5.2). A χ^2-fit routine (MINUIT) uses the angles from equation (5.2) as free parameters which are minimised until the impact coordinate predicted by the telescope is in agreement with the pixel coordinate of the corresponding event.

6 EXPERIMENTAL RESULTS

Nowadays most of the scientific research is based on computer aided analysis. The data stored in files contains vast arrays of numbers. One aspect of computional analysis is the visualisation of these numbers and the interpretation of the meaning.

Conclusions which are drawn from the analysis help understanding the microscopic processes of such a sensor and leads to further improvements.

The data obtained with the grazing angle method contains much more information on the performance of the pixel sensor than expected on the first inkling. The following subsections give an overview of the method used to analyse the data and present results and conclusions. The performed beam tests are mainly restricted on the regular pixel sensor design described in section 4.1.1 which is irradiated with 6×10^{14}pions/cm^2. This is the representative fluence anticipated for a radius of 7 cm and six years of LHC operation.

6.1 Methods of data analysis

The number of events which can considered for the analysis is limited. Part of this inefficiency is caused by the overlap of the trigger diodes causing readouts which contain no particle induced signal. Furthermore not every event containing a signal on a row of pixels can be used. Some of the signals are located in a pixel row on the edge. Or the particle impact is located in front of the pixel array or close to the end where only a part of the signal is indicated.

Therefore, an algorithm capable to find the typical signatures has to be developed which can distinguish between useful events and events which exceed the pixel array limit. Furthermore, data containing no pixel signals have to be used for updating the pedestal values.

Every readout channel (and therefore, every pixel) has a characteristic level caused by variations on the chip (pedestal) such as slight changes in the data buffer capacities. These levels show timely variations which depend on disturbances caused by electronic noise and pick up. Leakage current from the sensor pixels also lead to time dependent variations in the readout channels. In order to avoid high fluctuations amongst the pixels these pedestals should be updated regularly. For illustration this is explained here in more detail. A file, denoted as run, is described with a specific run number. Such a run contains several thousand events (typically 20'000) recorded under the same external conditions (such as bias voltage, temperature etc.). In the following 'event' denotes the data comprising a full readout of the 256 pixels. The first few thousand events contain no particle induced signal because of an artificial trigger delay (section 5.3.3). It was the initial idea to calculate average pedestal values from these events for each channel or pixel individually which could be subtracted from the events containing street signals. However, the external conditions did not remain stable during the three or four hours of data taking (caused by longer periods without beam) and therefore the pedestal variations show a time dependent variation.

The pedestal update is achieved by keeping a set of 20 bias values stored for each pixel, from which the average serves as pedestal value. Whenever the algorithm finds no particle induced hit on the entire pixel array, these values are added to the bias value set while the oldest entries are deleted. An illustration of this methodology is given in figure 42. It presents the data from a sensor irradiated with 6.3×10^{14} pions/cm^2 (annealed for $\sim$500 days at 2°) where the left graph shows the raw 256 ADC values containing a pion induced pixel signal. The adjacent graph represents the pedestals while on the right histogram pedestal corrected signals appear. The histogram to the right in figure 42 only has little resemblance with a street of pixels showing a signal. This is caused by the sequential readout which has nothing in common with the spatial location of the pixels. Only after sorting these signals by the pixel location the signals form an obvious street as shown in figure 43. A few thousand events similar to that one shown in figure 43 represent the statistical basis of further investigations.

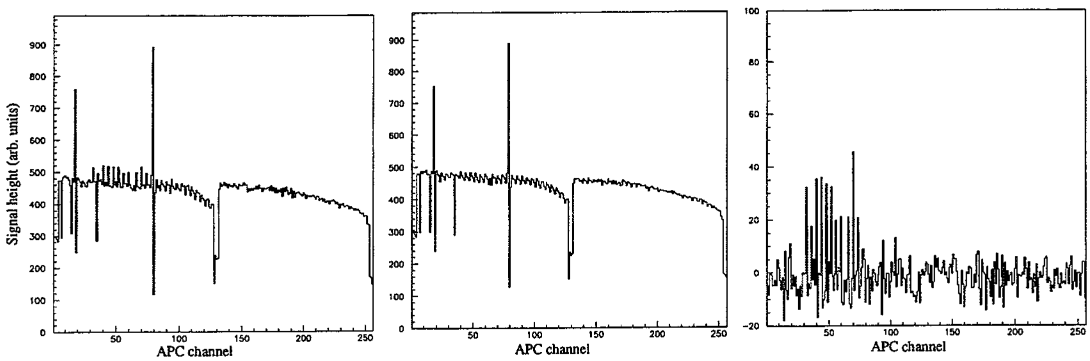

Figure 42: The raw data containing a pion induced signal is shown on the left. The medium histogram shows the corresponding pedestal values. The pedestal subtracted signals are shown in the right histogram. The striking peaks are caused by shorted readout channels and do not appear on the pedestal corrected histogram. On the left and on the middle histogram the two APC chips are distinguishable by the gap.

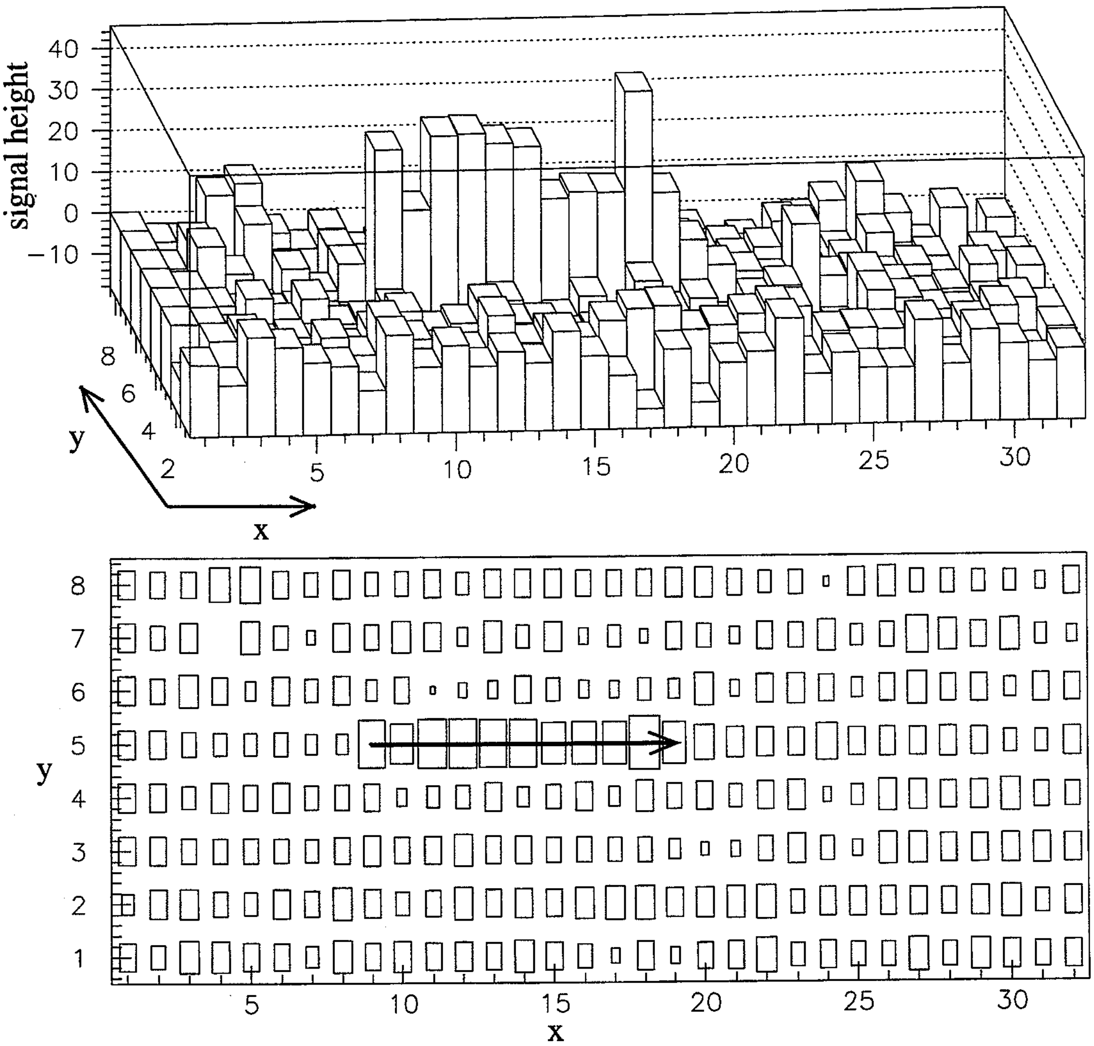

Figure 43: Same event as in figure 42 with the pixels sorted by their location and represented in a two dimensional lego plot (above) and as a box diagram (below). The pion induced signal generates a clearly visible pixel street. The arrow indicates the direction of the transversing pion.

6.2 Depletion depth profile

One of the main intentions of the method described is the determination of the depletion depth of irradiated silicon detectors. From equation (3.5) a linear dependency between the depletion depth and the square root of the applied bias voltage is expected. With the grazing angle method the validity of this correlation is tested on irradiated silicon sensors.

Therefore, the three sensors irradiated with different fluences of 1.4, 6.3 and 9 $\times 10^{14}$ pions/cm^2 are operated at various bias voltages. Before irradiation, each detector was tested under the same conditions in order to have representative data for the calibration. Figure 44 shows the pulse height profile of the averaged pixel street prior to irradiation and 20 days after irradiation with 6.3×10^{14}/cm^2.

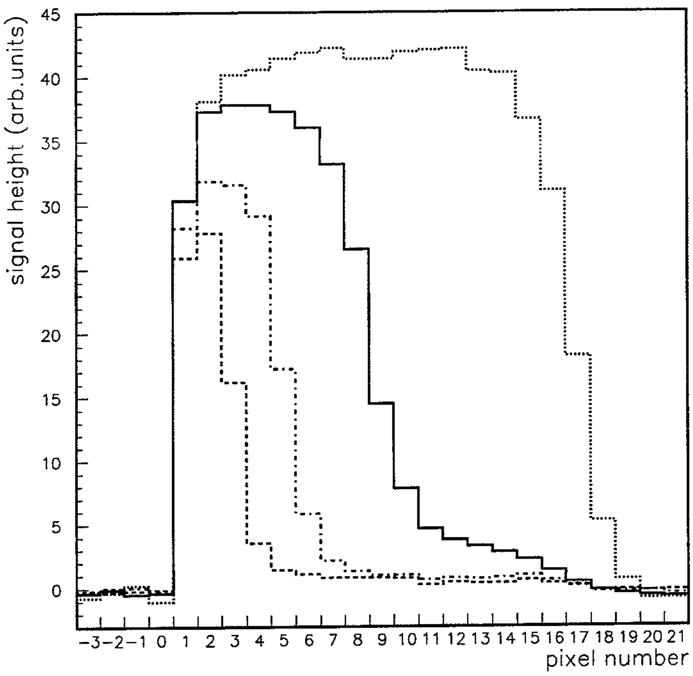

Figure 44: Pulse height profile of pixel rows for different bias voltages: The dotted line shows the detector prior to irradiation. Irradiated with pions to a fluence of 6.3×10^{14}/cm^2 the street shape at 300 V (solid line), 100 V (dashed-dotted line) and at 36 V (dashed line) is shown.

Before irradiation and as soon as full depletion is achieved, shape and length of the street are independent from the bias voltage (dotted line in figure 44). After irradiation, the strong dependency on the applied bias voltage becomes visible. Although the most probable charge deposition in a 300 μm thick silicon detector corresponds to an average of 25'000 electron-hole pairs the energy deposition along the particle track is a stochastic quantity. By superimposing several hundred events such as in figure 43, this stochastic energy deposition is equalised by statistics simulating a uniform signal which is distributed along the pixel rows.

The data which is recorded at different bias voltages is analysed for the relation between depletion depth and applied bias voltage (equation (3.5)). Adjacent pixels in the row are selected using a threshold criterion. The number of these pixels produce a row length spectra as a function of the bias voltage. By knowing the angle, under which the particles transverse the sensor, the obtained row length can be translated into a depletion depth. Figure 45 shows that the relation $d \approx \sqrt{V_{\text{bias}}}$ is conserved even for high fluences. This measurement has also implications on the effective doping concentration. Equation (3.7) shows the correlation of N_{eff} with the bias voltage and the square of the depletion depth. The observed linearity leads to the conclusion that the effective doping concentration has to be constant within the depleted volume. Otherwise the data points would deviate from the straight line fit.

An analytical dependency between the fluence and the effective doping concentrations is

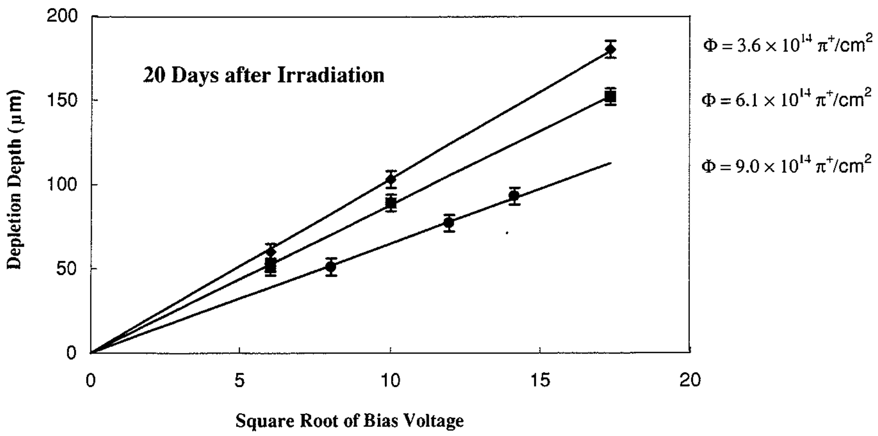

Figure 45: Depletion depth as function of the square root of the bias voltage for different fluences.

given for high fluences as

$$\Delta N_{\text{eff}} \approx C \cdot \phi, \tag{6.1}$$

with C as damage factor is characteristic for the irradiating particles. For pions this factor is determined to 0.03 /cm [50]. With this, the required voltage for depleting the detector to a certain depth is

$$V_{\text{bias}} \approx 2.5 \times 10^{-9} \cdot d^2 \cdot \phi. \tag{6.2}$$

The factor 2.5×10^{-9} appearing in equation (6.2) originates from the constants specified in equation (3.7) which are multiplied by C. The slopes at different fluences which can be determined from figure 45 are consistent with equation (6.2) and the observations of reference [59].

A closer look at figure 44 reveals a surprising fact. The row length is naturally limited by the depth of the depletion zone. The signal of the average row shape which is plotted with a solid line (V_{bias} = -300 V) does not drop instantly to zero. A signal originating from the undepleted region must arrive at the pixel readout. The mechanism which causes the charge transport within the undepleted region is subject of a model simulation described in sections 7 and 8. The following section describes the experimental method which investigates the time resolved shape of the pulse height profile.

6.3 Late charge observation and its explanation

The results presented above are based on a measurement using a shaping time which is at maximum 1 μs. Whether the charge is collected within a useful time in terms of LHC conditions remains to be answered. Therefore a measurement has to be performed which probes the charge collection time of irradiated silicon sensors.

This detailed time resolved measurement of the street shape requires a slight modification of the data acquisition setup. In particular, the time variation of the trigger signal has to be registered in coincidence with the data recording sequence. This is best explained using figure 46.

Figure 46 shows a selection of digital control signals which define the sensitive window of the APC preamplifiers. For better understanding a detailed view of figure 30 is added which displays a single channel of the amplifying circuit. The switches R12 and CS are always open. Thus, the preamplifier is in integration mode. As soon as the reset switch is opened the integrated charge from the pixel is written to the latch capacitor. By opening the switch behind the capacitor the stored charge is fixed. This handshaking mechanism between LE and Reset defines the maximum

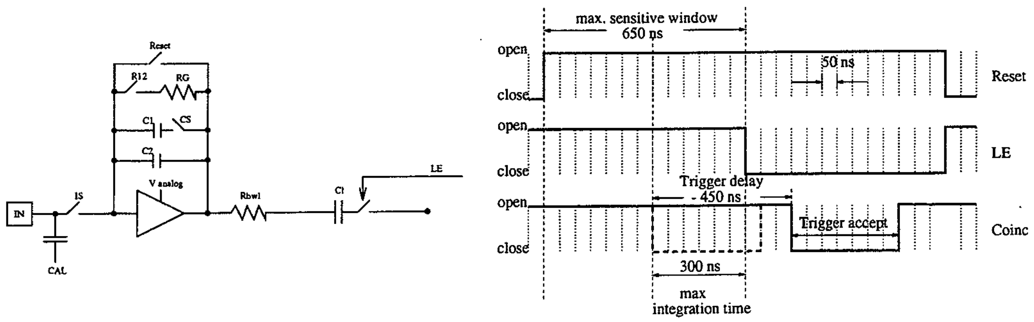

Figure 46: A selection of digital steering signals which control the data recording sequence of the APC chip. Additionally, a detailed view of the preamplifier stage from figure 30 is displayed.

sensitive window in figure 46 to be 650 ns. This integration time is limited by the artificial coincidence signal which defines the period in where trigger signals are accepted. Because of the trigger latency this window is delayed by 450 ns leading to a maximum integration time of 300 ns. In parallel, a 80 MHz scaler is started by the trigger signal, counting until the Reset switch is closed again. This time information is now added to the header file of each event bearing the integration time information. The larger the number, the longer the integration time.

This configuration allows a differentiation of the signals in time. The result of this analysis is shown in figure 47 where two time bins are created. The first graph shows the shape of the pixel

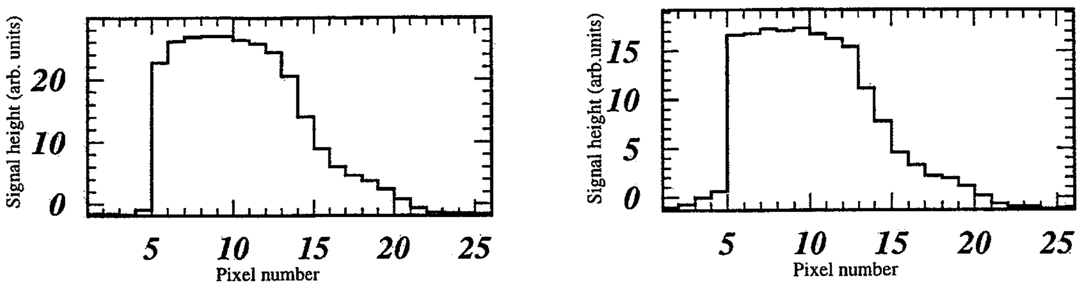

Figure 47: The analysis of two different integration times of a pixel sensor irradiated with 6×10^{14}pions/cm^2. The left graph is the street shape with a maximum integration time of 250 ns. On the right histogram the maximum integration time is 80 ns.

street with a maximum integration time of 250 ns. The right graph displays the signal distribution with a maximum integration time of 80 ns. Unfortunately it could not be measured below this integration time because it is the shaping time of the preamplifier. A slight difference is visible which becomes obvious in figure 48 where the ratio between the two histograms is shown. While the

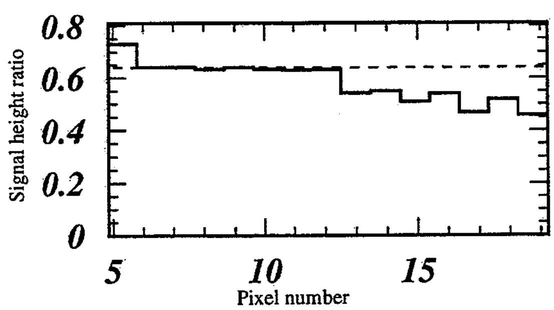

Figure 48: The ratio of the histograms displayed in figure 47. The dashed line denotes the ratio of an unirradiated sensor.

ratio between the different integration times of an unirradiated detector remains constant, the irradiated device (6.3×10^{14}/cm^2 plus 180 days annealed at 2°C) shows a discrepancy where charge from the undepleted region is observed. It implies that even after 80 ns which is a factor of ten above the usual charge collection time still charge is drifting towards the pixels. The microscopic mechanism which explains such a behaviour is unclear. But it is imaginable that this latency is caused by diffusion which is the main transport mechanism in the field free (undepleted) region. Another speculation arises from the suggestion that a slight electric field in the undepleted region is active. Reference [60] reports observations using α particles that indicate an non-zero electric field in partially depleted silicon detectors. The numerical simulation, described in section 7 comes to a similar conclusion.

6.4 Charge collection efficiency

In order to translate the ADC value into a charge, the number given by the ADC has to be calibrated. Two methods are possible and used. One method is described in this section. The other procedure is described in section 6.5.

Each of the sensors was tested prior to irradiation under the same conditions as after irradiation. Minimum ionising particles produce in average $\sim$80 electron-hole pairs per μm. By knowing the particle track length the area under the dotted line in figure 44 corresponds to the generated charge along the track. In this case, a track length of 2'062 μm ($\tan\alpha \times 16.5$ pixels) is measured for the unirradiated sensor which generates an average of 171'875 electron-hole pairs. This measure corresponds to 248 electrons/ADC.

Figure 49 presents again an extract of figure 44 showing the street profile prior and after irradiation. It is clearly observed that the charge collection efficiency of silicon detectors is reduced by radiation. Two effects are identified which cause the difference between the street shape of the unirradiated and the irradiated detector. The decreased depletion depth is responsible for a reduced pixel row length. Trapping is responsible for the signal height reduction of the row. In

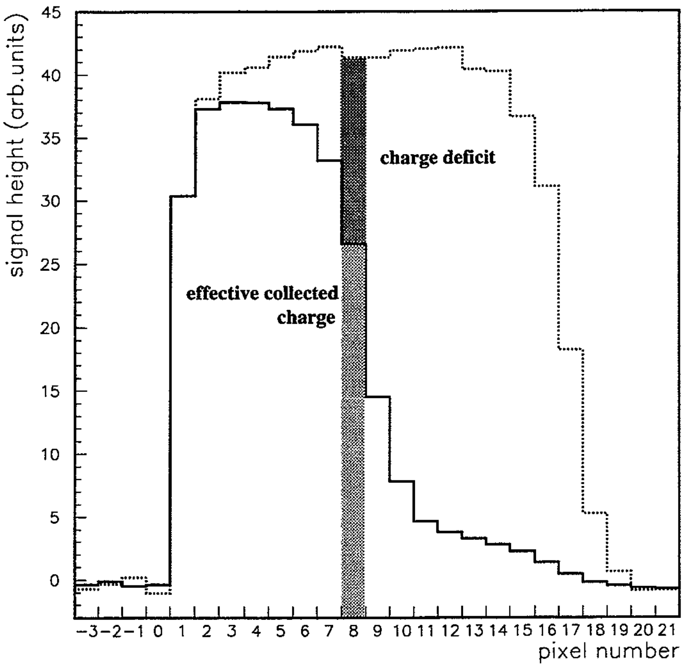

Figure 49: Comparison of the pulse height shape of the sensor prior to irradiation and after a fluence of 6.3×10^{14} /cm^2. The grey pattern emphasises a particular bin corresponding to a certain sensor depth. With the light grey the effective collected charge is expressed. The dark grey pattern stands for the charge deficit compared with data prior to irradiation.

equation (3.28) the trapping time τ in dependence of the fluence ϕ is given. For silicon prior to irradiation this trapping time is much longer than the collection time t_c for electrons and holes. Thus, no charge loss is observed. With the radiation induced change of N_{eff} trapping time becomes the same order of magnitude as the charge collection time.

A number of initially generated charge N_0 at $t = 0$ is assumed. After the time interval dt, the change of the number per time is given by the differential equation

$$\frac{dN_0}{dt} = \frac{1}{\tau}N_0 \tag{6.3}$$

The solution of such an equation is well known and the number of free carriers N_C is given by

$$N_C(t) = N_0 \cdot e^{-(t/\tau)}. \tag{6.4}$$

With equation (6.4) the number of trapped charge increases obviously with a decrease of the trapping time. Since the collection time is dependent on the drift length the probability of trapping increases with the depth in which the charge was generated. This leads to the exponential drop of the signal height profile in figure 44.

Using equation (3.25), generalised for electrons and holes, the observed exponential decay is explained by substituting the electric field with equation (3.17) which leads to

$$t_c \approx C \ln \frac{x_0}{x}. \tag{6.5}$$

Here, $C = d^2/2\mu V_{\rm bias}$ and x is the depth in which the charge is generated and x_0 the location where the charge is collected. Using this expression for t_c in equation (6.4), the following relation is derived

$$N_C = N_0 \cdot \exp\left(-\frac{C \ln(x_0/x)}{\tau}\right), \tag{6.6}$$

which leads to

$$N_C = N_0 \cdot (x_0/x)^{-(C/\tau)} = N_0 \cdot (x_0/x)^{-d^2/(2\mu V_{\rm bias}\tau)}. \tag{6.7}$$

This theoretically predicted behaviour is confirmed by the experiment. In figure 49 one pixel bin is additionally emphasised by a grey pattern. The light grey expresses the effectively collected charge by the irradiated sensor while the dark grey region denotes the charge deficit. In figure 50 the ratio between the effectively collected and the missing charge spectra is plotted for the fluences of 3.6×10^{14}/cm^2 and 6.3×10^{14}/cm^2. It shows the exponential behaviour as predicted by equation (6.7) as function of the depletion depth. The sensor with the lower dose was later again exposed up to a final fluence of 9×10^{14}/cm^2.

Comparing with data prior to irradiation the increasing charge deficit is determined as a function of the depth in which the charge was generated. With the calibration of the ADC

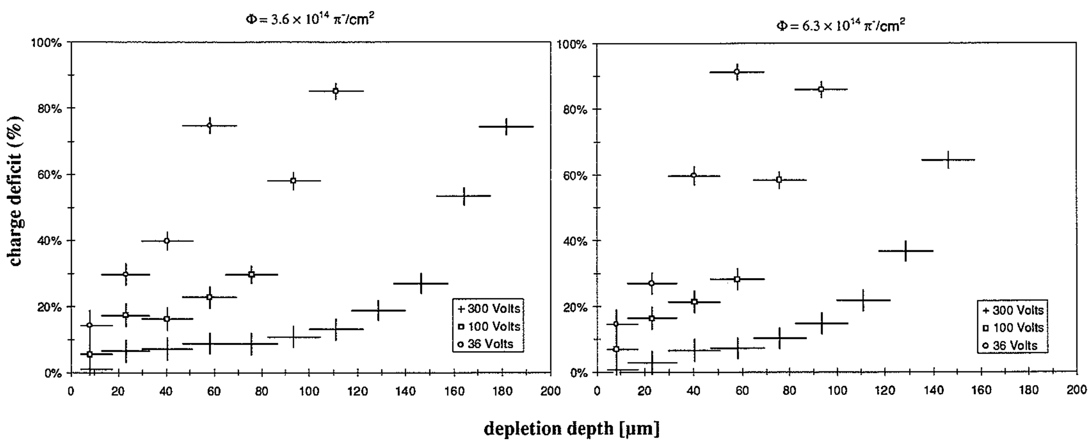

Figure 50: Charge deficit as function of the depth where the charge was generated for the different fluences.

scale, the signal charge for perpendicular tracks is determined to 9'300 electrons for a fluence of 6.3×10^{14} /cm^2 and with a bias voltage of 300 V. This number was obtained 20 days after irradiation at $-10.8°$C. The timely development of the charge collection efficiency is presented in section 6.6.

6.5 Leakage current

The leakage current of a single pixel after irradiation is a crucial value for the readout electronics. Due to the analog readout, the preamplifiers must absorb the pixel charge without getting into saturation. As safety margin, the CMS pixel chip is designed to absorb a leakage current of up to 100 nA.

In the framework of the grazing angle measurement a calibration measurement is performed determining the leakage current per pixel. Furthermore, the bias voltage supply is equipped with an Ampere meter measuring the leakage current of the entire sensor.

The increase of the leakage current as a function of the bias voltage is shown in figure 51. Most of the bulk generated leakage current is absorbed by the guard ring and by the n^+-implant surrounding the pixel array. At higher fluences and for temperatures above 0°C, the leakage current

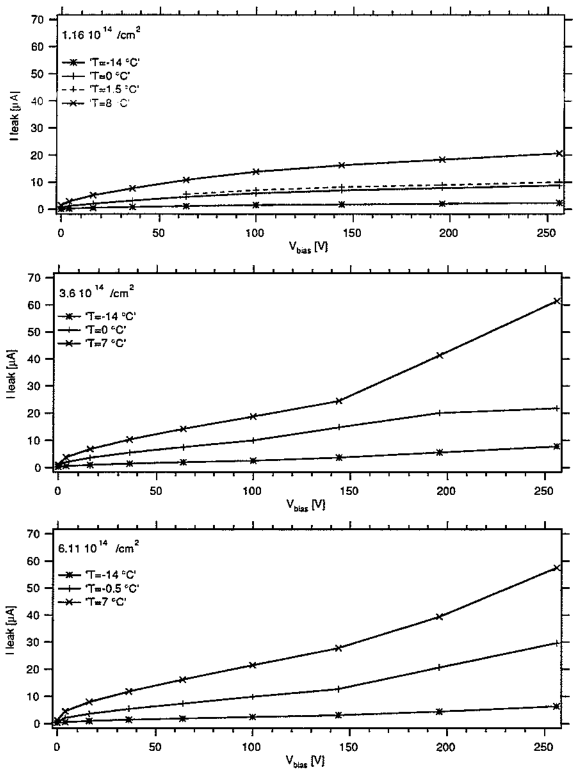

Figure 51: The leakage current measured for the entire sensor as a function of the applied bias voltage. The curves represent measurements at different temperatures and for the different fluences.

increases dramatically with increasing bias voltage which could result in thermal runaway. Thermal runaway is a vicious circle caused by self heating. High leakage current leads to an additional warming up of the sensor which results in an increased leakage current and so on. An uncontrolled rise of the leakage current leads to junction breakdown and to destruction of the sensor.

The leakage current of an individual pixel is measured in a calibration run using special capabilities of the APC chip. This is the second method how the ADC scale is calibrated. It is based on the built-in calibration mechanism of the APC. On demand a capacitor (CAL in figure 30) is supplied with a voltage generating a defined charge at the input of the preamplifier. This charge is measured to be $n{\cdot}0.78$ fC/V_{Cal} [62]. Here, n stands for the four variations on the capacitors. The size of these capacitors is $4n{\times}9\ \mu m^2$ with $n = \{1,..4\}$. Figure 52 shows the pedestal corrected readout of the channels 60-120 (chip1) with and without calibration signal. The differences of these four steps correspond to a certain charge per ADC bin.

In figure 53 the differences of all channels are plotted. The uppermost figure represents the subtraction of all channels containing a calibrate signal with $n = 3$ from the calibrate signals with $n = 4$. The result is a Gaussian distribution of the differences caused by natural variations of the capacitors and due to noise effects. But the mean gives the average ADC value which corresponds

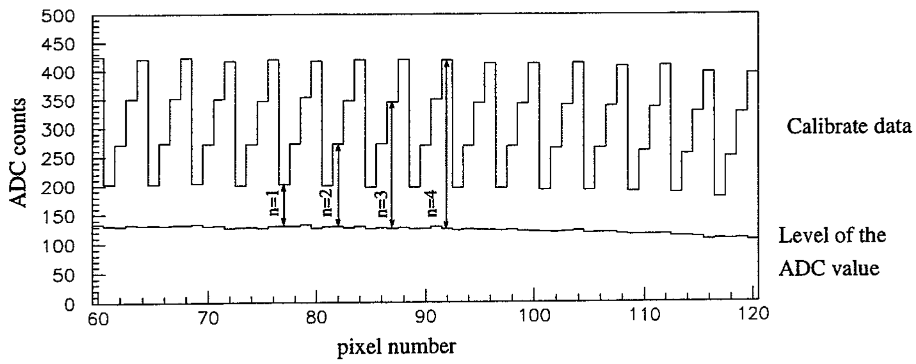

Figure 52: Readout of 128 pixels with and without calibrate signal. The figure shows the channels 60 up to 120. The lower curve are the ADC values when no voltage is applied to the calibrate capacitors. With 3.6 V applied, the calibrate signal is superimposed to the normal readout. The four different steps originating from the different capacities are clearly visible ($n = 1, ...4$).

to a charge of 0.78 fC/V_{Cal} with V_{Cal}=3.6 V.

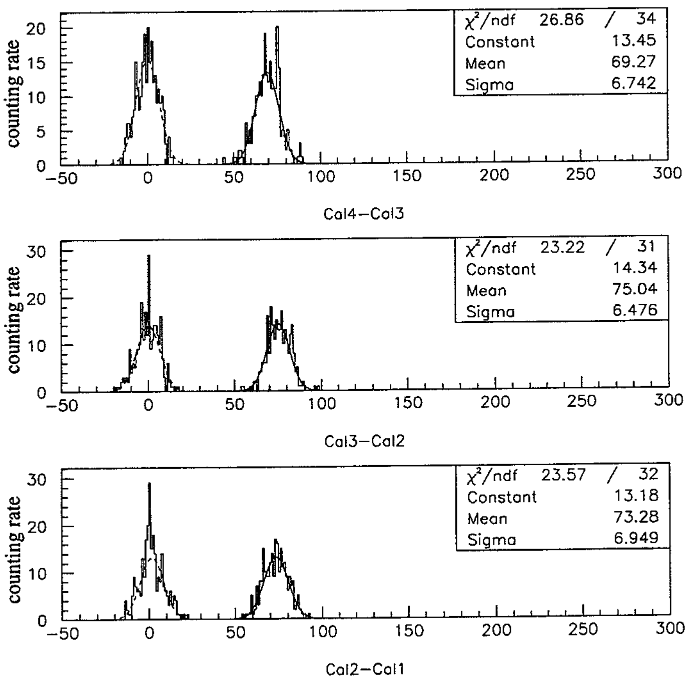

Figure 53: Differences between the calibrate signals for $(n = 4) - (n = 3)$, $(n = 3) - (n = 2)$ and $(n = 2) - (n = 1)$, respectively. The mean of the Gauss fit represents the ADC value which corresponds to a certain charge. The Gauss peak around zero are the pedestal corrected ADC signals without calibrate.

In order to test the correctness of the pedestals in figure 53 also the ADC signals without calibrate are plotted, producing the same spread as the calibrate signals. Therefore it is assumed that no additional effects are added by the calibrate operation. Averaging the three mean values a measure of 72.1 ADC counts yields which corresponds to 242 electrons/ADC (compared with 248 e/ADC from section 6.4).

The leakage current per pixel is determined with tree different data sets. Figure 52 shows two of them. The pure pixel signal and the superimposed calibrate signal. A third set of data is recorded with a slight change in the digital sequence, controlling the charge integration by the APC's preamplifiers. Here, the integration time is increased by 400 ns. Consequently, the integrated charge is expected to be higher than at shorter integration time because of the leakage current. Similar as in the proton irradiation setup (section 5.4), the increase of the ADC value from the shorter to the longer charge integration time is translated into a charge using the calibrate data. The leakage current is calculated using $I_{\text{leak}} = \Delta Q/\Delta t$ with $\Delta t = 400$ns. For a fluence of $6\times10^{14}/\text{cm}^2$ and a bias voltage of 300 V a leakage current of 11 nA is obtained at -5°C.

By transforming some equations introduced in section (3.1.3) the experimental data can be compared with the predictions from the theory. With equation (3.5) the leakage current calculated in equation (3.18) becomes dependent on the bias voltage. The fluence dependency is given by equation (3.19) and temperature dependence is shown in equation (3.20). Some of the expressions describe a relative change of the leakage current and therefore an expression is derived which compares the ratio of the measured leakage current at different temperatures, bias voltages and fluences.

$$\frac{I_1}{I_2} = \sqrt{\frac{\phi_1 V_1}{\phi_2 V_2}}\, e^{-0.1\Delta T}. \tag{6.8}$$

Here, the damage constant α which is characteristic for the irradiated device and the type of the radiation as well as other parameters can be reduced. The expression $\exp(-0.1\Delta T)$ is an approximation for the leakage current ratio at two different temperatures. As a rule of thumb: the leakage current changes by a factor of two for every 7°C [61].

Equation (6.8) provides an important test for the data obtained with the calibration setup allowing a comparison with the theoretical prediction. Table 6 represents a set of calibrate data obtained at different temperatures, bias voltages and for different fluences. The ratio of the ex-

Run number	Fluence $[10^{14}/\text{cm}^2]$	Bias voltage [V]	Temperature [°C]	Leakage current [nA]
185	9.1	100	0	16.2
187	9.1	144	0	18.2
201	6.3	256	0	19.7
209	6.3	300	-10	8.2

Table 6: Tabulation of the experimentally obtained leakage currents at different temperatures, bias voltages and different fluences.

perimentally obtained data compared with the ratio calculated with equation (6.8) are in good agreement:

$$\left(\frac{I_{185}}{I_{210}}\right)_{\text{exp}} = 0.822 \rightarrow \left(\frac{I_{185}}{I_{210}}\right)_{\text{theo}} = 0.756$$

$$\left(\frac{I_{185}}{I_{209}}\right)_{\text{exp}} = 1.975 \rightarrow \left(\frac{I_{185}}{I_{209}}\right)_{\text{theo}} = 1.922$$

$$\left(\frac{I_{201}}{I_{209}}\right)_{\text{exp}} = 2.400 \rightarrow \left(\frac{I_{201}}{I_{209}}\right)_{\text{theo}} = 2.510.$$

A lego histogram plots the spatial distribution of the leakage current. In figure 54 such a map is shown. The lego diagram shows the predicted uniformity of the leakage current distributed along the pixel array.

During beam test periods and in the analysis, some of the irradiated sensors showed spots of nervous pixels. Namely, when a new detector was taken out of the refrigerator where they are stored and transported into the cooling box in the beam test area. Most of these regions disappeared after a certain time by conditioning with high bias voltage ($\sim$ 400 V). But in particular under operation with the grazing pion beam some regions remained active. These spots turned out to be in the neighbourhood of a pixel which was by accident not connected to a readout channel.

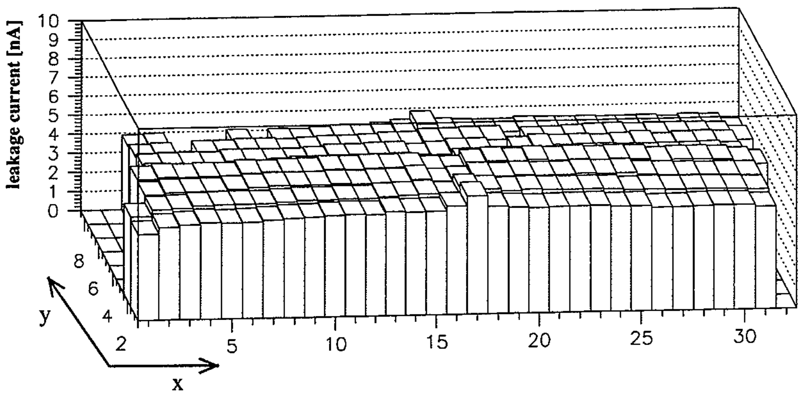

Figure 54: A map of the leakage current distribution for each pixel showing the predicted uniformity. Lego diagram of the same sensor with $6.3\times10^{14}/cm^2$ and at V_{bias}=-300 V (T=-10°C), measured 20 days after irradiation.

This incident is also observed by other groups [63] and is explained by stochastic discharges of the non-connected pixel. Floating pixels collect the charge just like the others but the collected charge leads to an increase of the pixel potential. When the potential difference exceeds a certain value, abrupt discharges to the adjacent pixels as in figure 55 above occur. The problem is

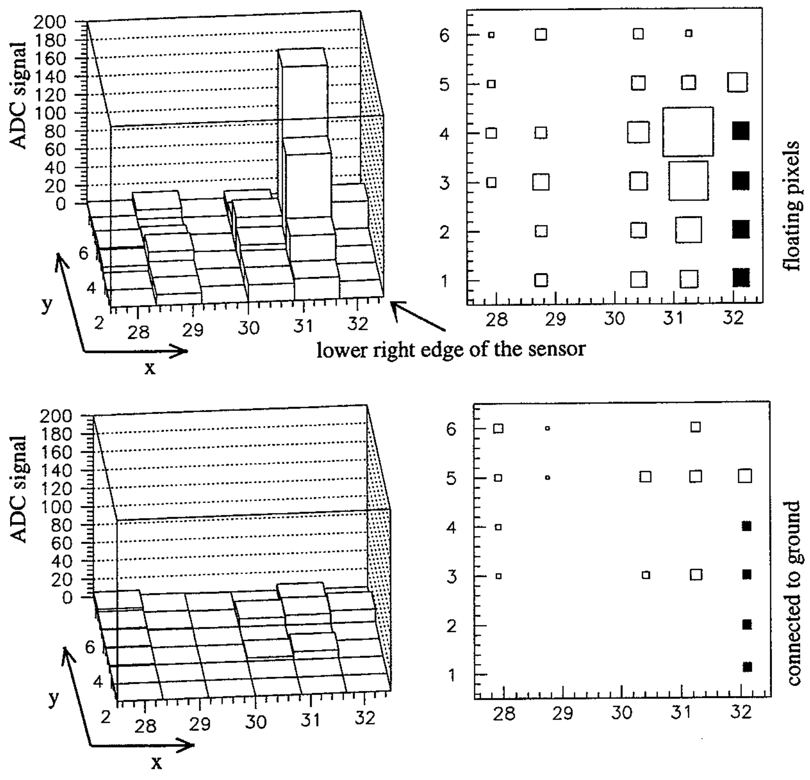

Figure 55: Left: detail view of a region showing an abrupt discharge of a floating pixel to the neighbouring region. Right: after connecting the pixel to ground this phenomenon is not observed anymore.

not anymore observed when the floating pixel is connected to ground potential as in the figure 55 below.

In the assembling phase of the CMS detector it can happen that a bump bond between the readout amplifier and the pixel fails to form a connection. Since the readout circuits cannot distinguish a discharge generated event from a real event stochastic discharges have serious implications for the CMS pixel detector regarding the occupancy.

A solution is the proposed design in figure 56. Here, the pixel implants are surrounded by two floating p^+-stop rings. Both have a small opening opposite to each other creating a highly re-

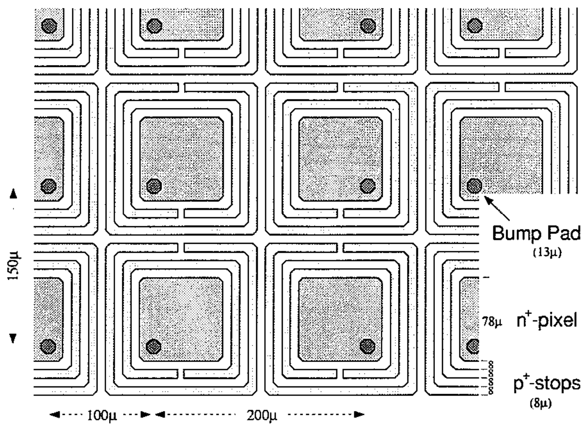

Figure 56: Layout of a pixel sensor with 150 μm pitch. The double p^+-stop rings are floating and allow a high resistive path to the neighbours.

sistive channel to the neighbouring pixels. This inter-pixel network has little effect on fast, particle induced signals but provides a potential for non-connected pixels and therefore prevents stochastic discharges. In addition, this network allows testing the sensor and measuring the leakage current of the entire sensor before bump bonding.

The dark bump bond pads in this design are shifted by 25 μm to the outside in order to fit the recent double column layout of the readout chip. This gives an alternating 100 μm/200 μm bump pad pattern. The diameter of 13 μm is minimised in order to decrease the stray capacitances.

6.6 Annealing effects and long term behaviour

The most realistic simulation of LHC conditions would need irradiation in portions of the anticipated fluence while the sensors are operated in a cooled environment. But it is more practical to simulate radiation damage in a more economic and less time consuming scenario. In the case described here, the detectors were irradiated with fluences anticipating different luminosities of the LHC collider. Periodically repeated measurements over a few hundred days will provide knowledge of the long term behaviour of irradiated detectors and deliver a time scale for the annealing processes.

The irradiated sensors are periodically tested with the grazing angle method. All the parameters such as leakage current and depletion depth discussed in the sections above are followed up with the time which has passed since irradiation. The most realistic fluence anticipated for a radius of 7 cm is $6.3\times10^{14}/\text{cm}^2$ Therefore, the according sensor is in the focus of the presented long term study.

Altogether, the grazing angle measurement was repeated four times in periods of 20, 180, 380 and 500 days since irradiation. The first three measurements were performed at PSI using pions with 330 MeV. The last data taking period took place at CERN in the framework of the Lorentz angle measurement using a 225 GeV/c pion beam.

Depletion depth

Starting with the investigation of the long term behaviour of the depletion depth figure 57 shows on the left the evolution of the depletion depth as a function of the bias voltage over a period of 550 days. Depletion depth and charge collection efficiency are directly correlated. Because of the increasing depletion volume more charge is collected. In parallel it is observed, that the trapping time τ decreases.

The above plots in figure 58 present the street profile recorded at different times. It can be noticed that the scale of the ADC axis varies. This was caused by a change in the SIROCCO offset which was necessary between the first and the second test beam measurement. Because of this change the absolute calibration of the ADC scale was lost. Assuming that the plateau and in par-

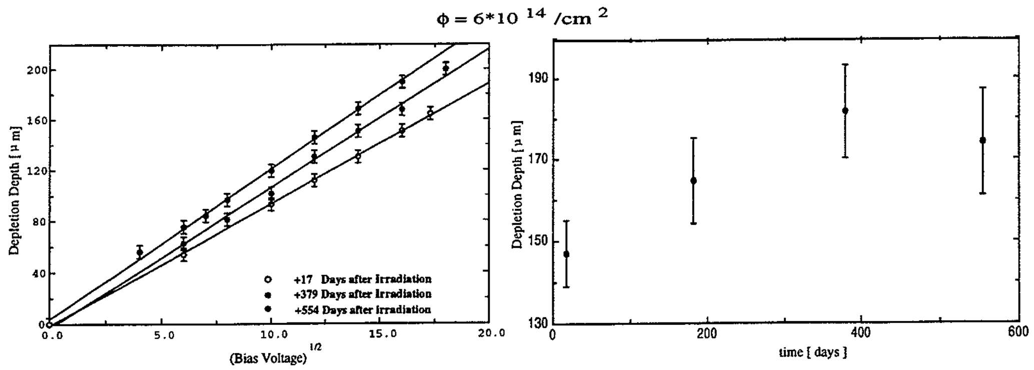

Figure 57: Left: evolution of the depletion depth as function of the applied bias voltage. Right: the depletion depth as function of the time at for a fluence of $6.3\times10^{14}/\mathrm{cm}^2$ and with a bias voltage of -300 V.

ticular the amount of charge collected by the first pixels in the row nearly corresponds to the total collected charge of an unirradiated detector the ADC scale could be calibrated again. This measure is supported by the calibrate data which show the same decrease. For security at the CERN setup this was calibrated again using an unirradiated sensor which confirmed the above assumption.

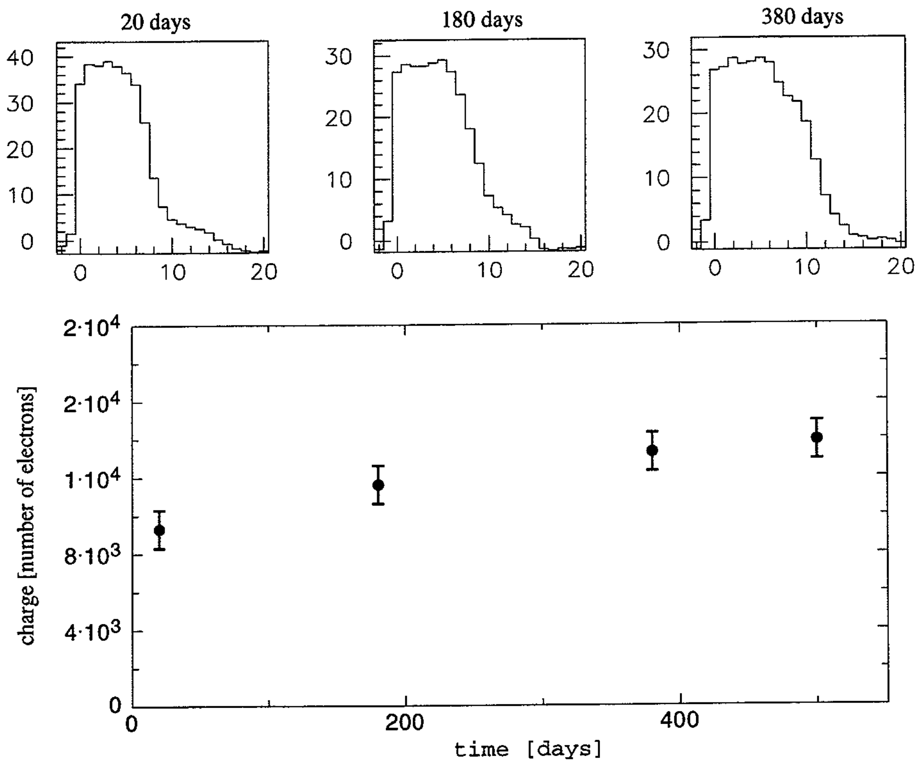

Figure 58: On top of this figure the street profile of the same sensor is presented (fluence $6.3\times10^{14}/\mathrm{cm}^2$) at a bias voltage of 300 V. The three graphs differ in time with 20, 180 and 380 days past irradiation. Below all four measurements are included as function of time.

Effective carrier concentration

At a bias voltage of -300 V the depletion depth has increased from initially 150 μm up to almost 200 μm, shown in figure 57 on the left. Employing equation (3.7) this measurement is directly translated into the effective carrier concentration (figure 59). The last measurement performed 500 days after irradiation indicates that the beneficial annealing has come to an end and no further recovery is expected. Owing to this, a sensor thickness of 200 μm is anticipated for the CMS detector. The real scenario at LHC foresees that the pixel detector is operated at a temperature below

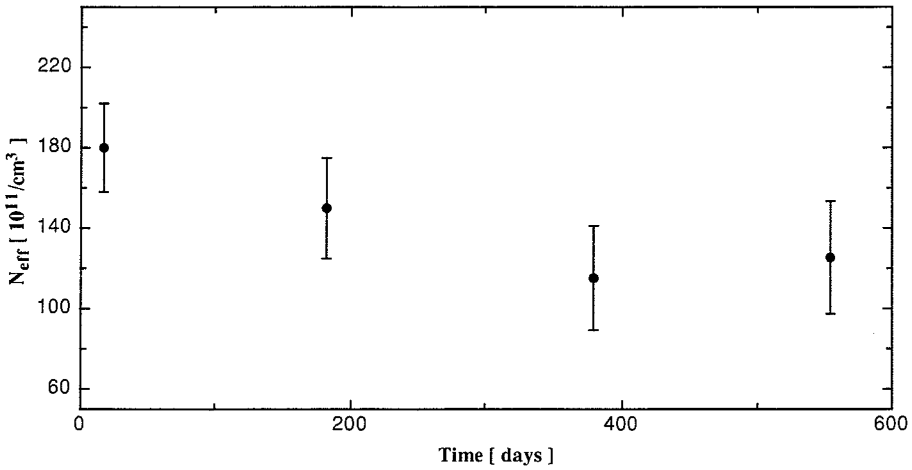

Figure 59: The development of the effective doping concentration as function of the time past irradiation.

$-5°C$. During maintenance, when parts of the tracker are removed the pixel detector is without cooling for a certain time. Within the warm phases ($\sim$ 20°C over several hours) the annealing processes are accelerated and the dominating beneficial part is welcome. But special precaution has to be taken on the temperature budged in order to prevent reverse annealing. It is strived that an average temperature of 5°C/year should not be passed. Therefore the simulated annealing with storage of the sensors at 2°C is quite realistic and conclusions can be directly transfered.

Leakage current
The leakage current is also subject of the long term investigation. Figure 60 shows the measured leakage current as function of the time since irradiation. According to the Shockley-Read-Hall

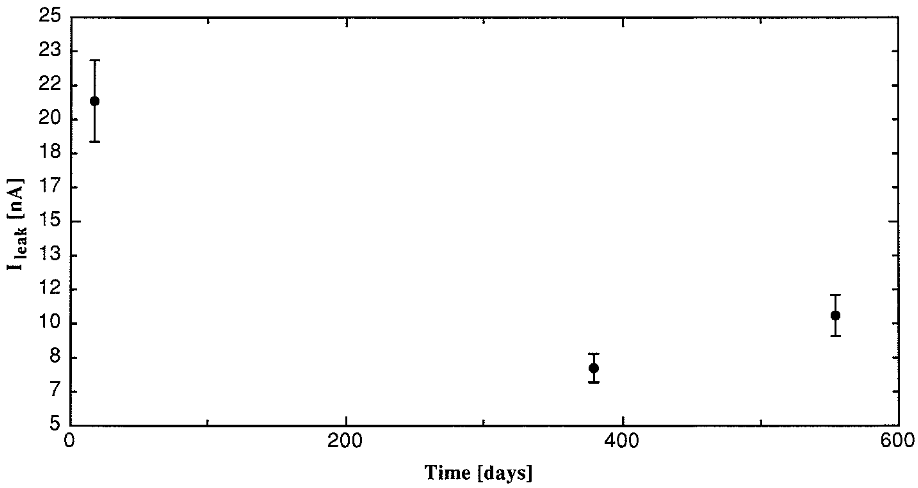

Figure 60: Leakage current as function of the passed time since irradiation. All data points are normalised to 0°C.

theory the increase of the leakage current can be described by the emission process. By substituting the effective carrier lifetime in equation (3.18) by its original definition [19], the radiation induced increase of the leakage current is related to the emission rate for electrons and holes $r_{\mathrm{e,h}}$ and by the induced defect concentration N_{d} [64]

$$\Delta I = N_{\mathrm{d}} q_0 \frac{r_{\mathrm{e}} r_{\mathrm{h}}}{r_{\mathrm{e}} + r_{\mathrm{h}}}. \tag{6.9}$$

Equation (6.9) implies that a decrease of the defect concentration leads to a reduction of the leakage current which would agree with the above measurements if N_{eff} can be identified with the defect concentration N_d. A comparison between the figures 59 and 60 would confirm such an assumption.

For pixels with a size of 150×150 μm^2 the leakage current is expected to be 44% higher.

6.7 Direct Lorentz angle measurement

The spatial resolution benefits from the Lorentz effect because of increased charge spreading. As reported, the signal after a fluence of 6×10^{14}/cm^2 is about 9'300 electrons. If this charge is distributed over more than two pixels, the charge per pixel is of the order of the readout chip threshold which is around 2000-3000 electrons. Therefore, the Lorentz force induced deflection angle (see equation (3.33)) is an important measure.

Figure 2 in appendix B explains how the grazing angle method is used for determination of the Lorentz effect. Again the method takes advantage of the simple geometric relationship (equation (6) in appendix B) between the measured and the wanted values

$$\tan\theta = \frac{\tan\beta}{\tan\alpha}. \qquad (6.10)$$

In this simplistic model, the Lorentz angle θ is determined by the grazing angle α and by the observed deflection angle β of the charge measured at the surface. Since in different depths of the sensor bulk different potential distributions are expected (figure 13) only a method simulating a three dimensional light spot is suited to resolve these effects. The grazing angle method has proved to be a good application to study charge drift effects with a good resolution. But this resolution is not sufficient for a precise measurement of the Lorentz angle.

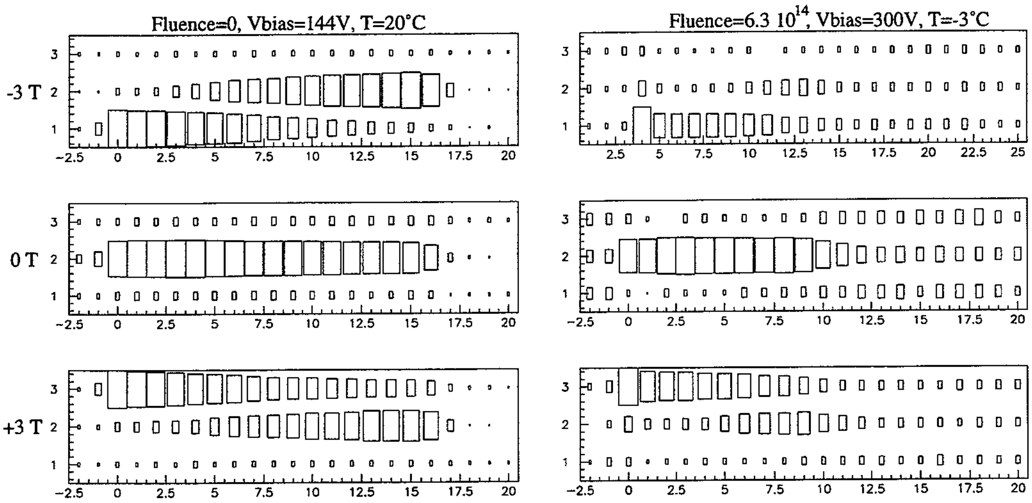

Figure 61: Qualitative result of the Lorentz angle measurement without tracking information. Left: the unirradiated sensor with ±3 Tesla magnetic field and without magnetic filed (centre plot). Right: the same measurement with the irradiated sensor with a fluence of 6.3×10^{14}/cm^2 (annealed 500 days at 2°C).

In case of the unirradiated sensor, 300 μm is the maximum drift length of the charge carriers. The anticipated charge deflection by the Lorentz force is 148.5 μm (using a 3 Tesla magnetic field and a Hall mobility μ_H=1650 cm^2/Vs) which of in the order of the pixel pitch. In the irradiated case the expected deflection with a depletion depth of 150 μm amounts to 74.3 μm. Therefore, the precise tracking information provided by a beam telescope is indispensable.

Figure 61 shows the result of the Lorentz data without tracking information. The plots on the left of figure 61 show the Lorentz effect of the unirradiated sensor at ± 3 T. The centre plot is without magnetic field. After irradiation with 6.3×10^{14}/cm^2 and 500 days annealed at 2°C the plots on the right of figure 61 are obtained.

In the irradiated as in the unirradiated case a slight difference between the two directions of the magnetic field are perceivable. For the unirradiated sensor at -3 Tesla the deflected charge on the neighbour pixel road is more distinctive than in the data with +3 Tesla magnetic field. In the irradiated case the opposite behaviour is observed. This observation has its simple explanation in the pixel rows of the sensors which are not exactly parallel to the particle beam. A small deviation leads either to an amplification or to an attenuation of the Lorentz effect. The angle between the axis defined by the particle beam and the pixel sensor has to be adopted for the Lorentz angle determination. In figure 41 this deviation is expressed by the angle β (this β differs from the one used in equation (6.10)).

With the precise tracking information for the impact position of each event the resolution of the plots shown in figure 61 can be increased. In figure 62 this improvement becomes apparent. Here, instead of three rows of pixels only the two participating rows are shown and the binning

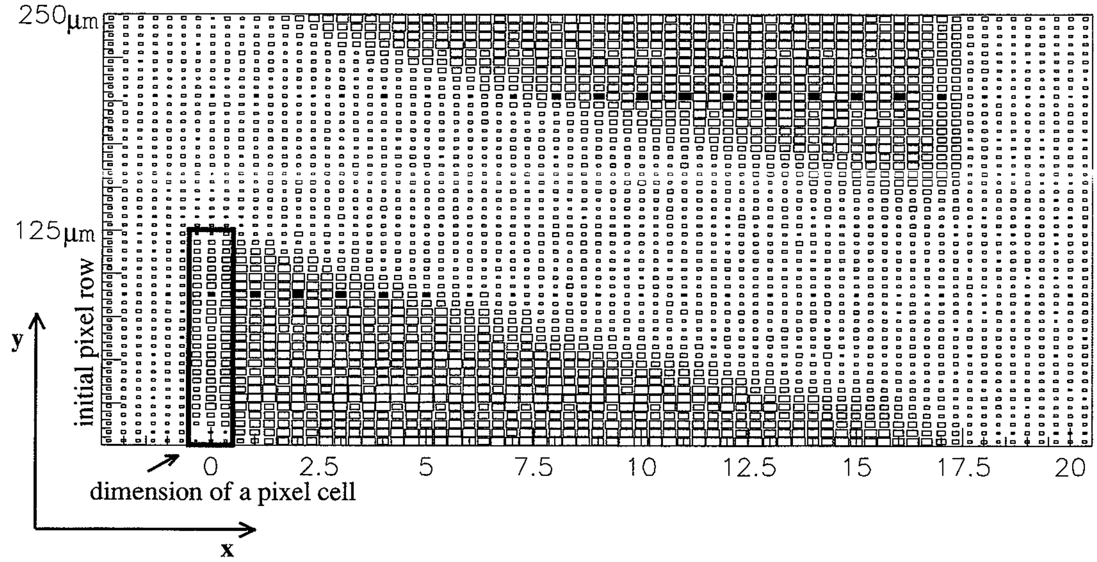

Figure 62: The same data as shown in the left of figure 61 for -3 T. While in figure 61 three rows of pixels are plotted, here only two rows of pixels are shown. The impact point predicted by the telescope is on the lower pixel row.

of the histogram is therefore increased. Using equation (5.2) the particle trajectory is translated into a pixel coordinate with an accuracy of ~2 μm in y and ~5 μm in the x coordinate. The 125 μm wide pixel cell is subdivided into 25 bins of 5 μm in y and into 3 bins of 41.6 μm width marked with a frame in figure 62. If, for example, the telescope predicts a particle impact in the coordinates x=5.6 and y=3.7[10] then the signals of the pixel row number 4 are added to the bins which are marked black in figure 62. Accordingly, the signal of the neighbouring road is added to the corresponding bin (the upper marked boxes in the figure). In this manner, with a few thousand events the histogram is filled leading to the presented appearance.

For the determination of the Lorentz angle the binning in the x-direction is not necessary and therefore neglected in the following. Figure 63 shows again the data of the unirradiated sensor at -3 T, this time without fine binning in the x-axis. This plot is used to determine the angle β.

The charge distribution asymmetry is calculated according to

$$A = \frac{Q_n - Q_i}{Q_n + Q_i} \in [-1, 1]. \tag{6.11}$$

Here, Q_i stands for the charge collected on the impact pixel row and Q_n denotes the charge of the neighbour row. According to the data presented in figure 63 above, the distribution of A employing equation (6.11) is shown in figure 64.

If more than half of the total charge is collected on the upper (lower) curve the value of A becomes negative (positive). In order to obtain the correct β the value of A has to be normalised. With this normalisation the fit parameter A1 corresponds to $\tan\beta$ as shown on the bottom of

10. These values have to be multiplied by the pixel pitch in order to have the absolute position in μm

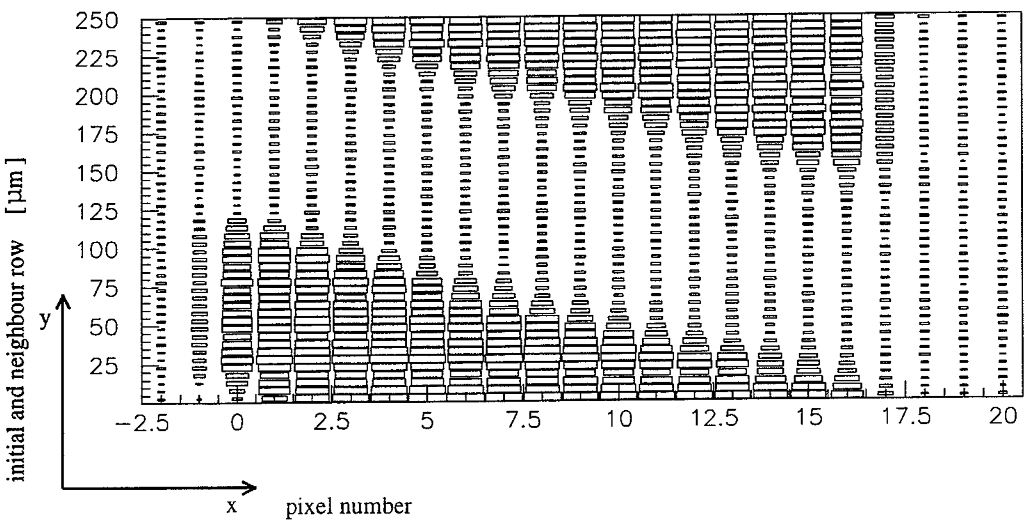

Figure 63: Same data plotted as in figure 62 without fine binning along the x-axis.

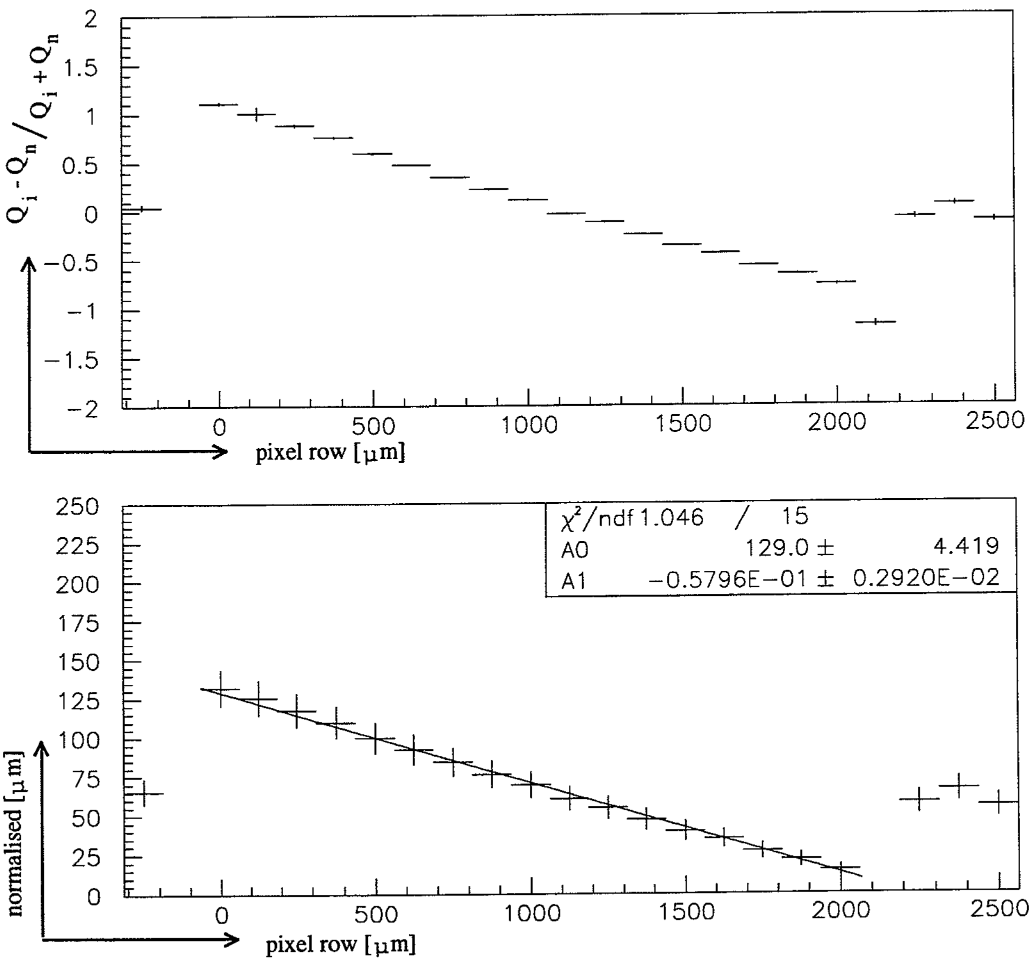

Figure 64: The distribution of A as calculated with equation (6.11) using the data of figure 63. Above: without normalisation, on the bottom: with normalisation. The fitted slope parameter gives the correct value for β.

With this normalisation the fit parameter A1 corresponds to $\tan\beta$ as shown on the bottom of figure 64. This measure leads by performing all necessary corrections to a Lorentz angle of 18.2° at 3 T. The other results of this procedure are summarised in table 1 of the appendix B.

In case of the irradiated sensor (figure 65) the same procedure was used but more difficulties arise. One is the reduced depletion depth which decreases the signal on the neighbour road. Another peculiarity is the kink visible in figure 65.

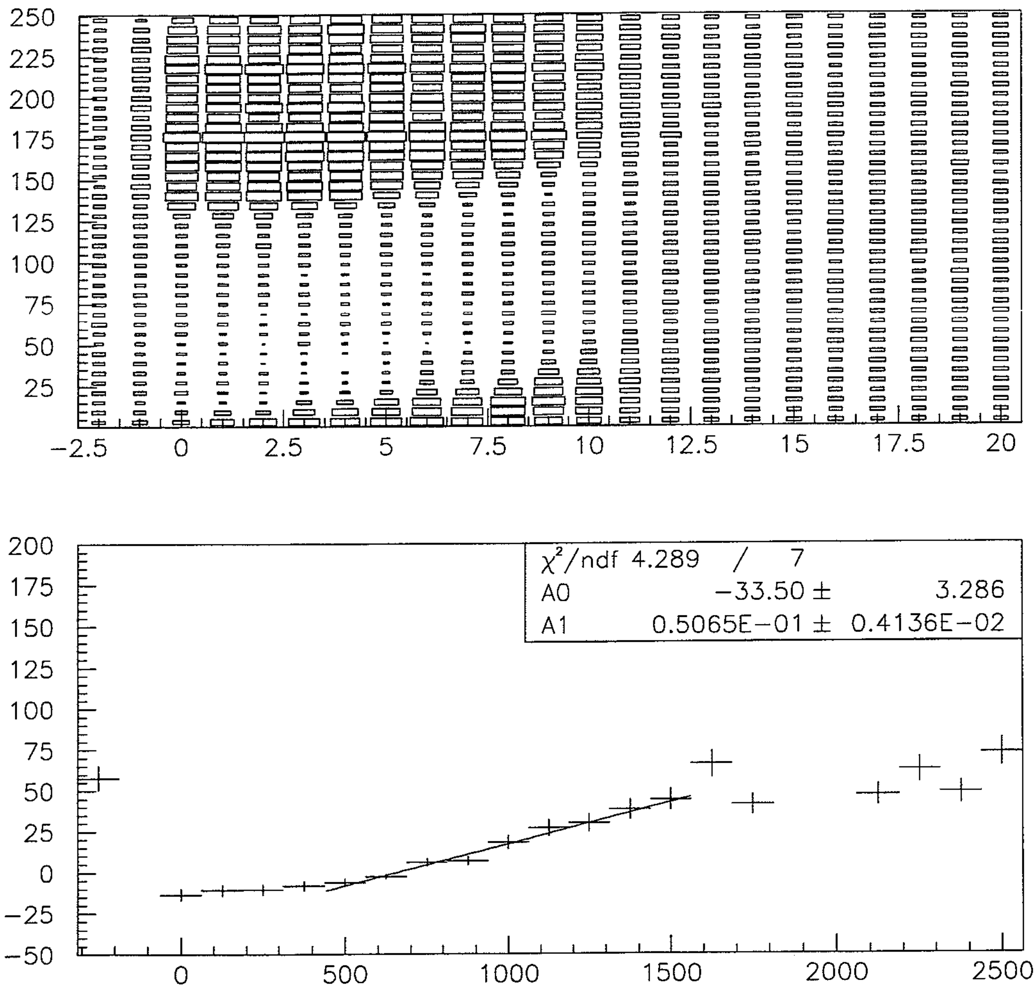

Figure 65: Data recorded at a magnetic field of B=+3 T. Above: data from the irradiated sensor displayed in the same way as in figure 63. Below: presentation of the irradiated data according to equation (6.11).

The reasons for this appearance are not entirely understood but the simulation in section 8 confirms that it is caused by the potential distribution of the electric field underneath the surface. In figure 13 the potential distribution of a pixel like structure was calculated. Additionally it was mentioned that field irregularities caused by the implants reach into the bulk. The depth of these irregularities is about the same as the width of the gap. If these $\vec{E}$-field disturbances suppress the Lorentz effect the obtained appearance is plausibly explained.

To verify that the above mentioned explanation is in the order of the observed effect this will be demonstrated on the example of figure 65. The bend occurs at the sixth pixel which corresponds to a depth of 77.5 μm (pixel#6·binning (125μ)· $\tan\alpha$) for a grazing angle of α =5.9°. The gap width of the sensor used in this measurement is in the same order (60 μm).

It is a legitimate question why this effect is not observed in the unirradiated case. The irradiated sensor is operated in underdepletion and therefore the disturbance of the field lines is apparently higher than in case of overdepletion. Therefore, the more reliable measure is 26.8° for 3 T as quoted in table 1 in appendix B.

7 NUMERICAL SIMULATION OF THE EXPERIMENTAL MEASUREMENTS

Computer simulation methods are now an established tool in many branches of science. The motivation for computer simulations of physical systems are manifold. One of the main motivations is that one eliminates approximative models with computer simulations. More complex problems in physics are generally not amenable to analytical solutions and one has to resort to some kind of approximation. With computer simulation systems can be studied that are not yet tractable with analytical calculations. The numerical approach allows to study complex systems and gain insight into their behaviour.

At the outset of a simulation stands the well defined model of a physical system. The intention of a simulation is to compute the properties or observables of the physical system which are not determinable by the experiment or by the analytical model. The simulation described here is motivated by open or unanswered questions such as trapping constants (see section 3.2.2) and the late charge observation (section 6.3) proceeding from the grazing angle experiment.

The numerical model should simulate the charge collection process and describe the observed signal formation. Issues addressed in the simulation include:

Charge injection: including randomly generated tracks, electron-hole pair creation along the predefined track and the calculation of the number of electron-hole pairs according to the straggling function from Bichsel (see section 7.2).

Charge carrier diffusion: diffusion of electron-hole pairs within the entire simulation. The simulation time base which corresponds to realtime is defined by the diffusion process.

Drift: movement of the charge carriers under an externally applied potential difference.

Radiation effects: reduced depletion volume due to radiation induced impurities and charge carrier trapping.

Induced signal: trapped charge carriers induce a signal on the readout.

Magnetic field: charge is deflected by the Lorentz force.

Furthermore all effects mentioned should be parametrised and adjustable to the experimentally observed signal The output should be in the same data-format as the real data superimposed with pedestal values from the experiment. Aiming at the reproduction of the experimental data the simulation output could then be scrutinised with the same analysis program mentioned in section 6.1.

7.1 Basic approach and assumptions

The simulation is a FORTRAN code in which the spatial location of each charge carrier is defined by three variables x, y and z. Here, x and y have the same orientation as used in the analysis defining the sensitive pixel area. With z the depth into the bulk is described where $z = 0$ refers to the n^+-pixel side.

These three variables are predefined one dimensional arrays and each array number identifies a charge carrier. Therefore the maximum number of electron-hole pairs is restricted to the depth of the array. A particle grazing the detector under a small angle generates about 200'000 electron-hole pairs. Since the generated charge is randomly distributed and because of the changing drift length this number is highly variable. If the charge generated exceeds the predefined array limit this event is rejected.

An advantage of this method is that besides of the limitation of the number of electron-hole pairs the detector size in which the carriers move is unlimited.

7.1.1 General assumptions to simplify the numerical simulation

To study the behaviour of charge carriers under an externally applied electric field some restrictions and assumptions have to be made. Each charge carrier is assumed to be independent from the other. Neither mechanical nor electrical interactions among the particles is allowed and only the exterior forces determine the movement. These movements are treated in a classical, non relativistic way. The released charge does not modify or influence the field lines of the externally applied field.

For the study of the charge carrier dynamics no quantum mechanics is used. The array in which the charge carriers move has a macroscopic scale (the same extension as the real pixel device). It is considered that the implants do not extend into the bulk and therefore no deformation of the electric field lines results. They are all in parallel, and the pixel cells touch each other without gaps. Therefore, charge is collected by a pixel as soon as it reaches the surface (z=0) and when its coordinate corresponds to the pixel location.

Modelling irradiated silicon sensors, additional assumptions have to be made. The charge collection time is assumed to be much faster than the the time period a trapped carrier remains within the trapping centre. Typically, charge in a 300 μm thick silicon detector is collected within about 8 ns [17]. In contrary, detrapping is of the order of μs [65]. Here, detrapping denotes the time measured between a charge carrier capture by a trapping centre and its release. Therefore trapped charge only influences the signal which is measured by the amplifiers. Then the charge carrier remains motionless and is not further considered.

High effective doping concentrations have a perceptible effect on the carrier mobility [20]. Up to a concentration of 10^{15}/cm^3 it is negligible and therefore not considered in the simulation (see section 6.6).

High electric fields, as discussed in section 3.1.1, also affect the mobility of electrons and holes. The linear relationship between the carrier velocity and the mobility times the electric field (equation (3.9)) is invalid for field strengths above 10^4 V/cm. This condition is exceeded by the experiment (a voltage drop of 300 V over 150 μm leads to 2×10^4V/cm). In case of type inversion where the junction is on the n$^+$-side, the highest field strength is found below the pixels. Here equation (3.9) is not valid anymore. In case of the simulation this fact is ignored since only a small region is affected.

The transition between the space charge and undepleted region is treated as an abrupt phase shift (which is in reality surely not the case) from a mainly field free into a region with a defined electric field.

7.1.2 Random number generator

Although complete randomness of such a generator is, strictly speaking, impossible on a finite digital computer many generators are available which pass various tests for statistical independence.

Computer simulations of Brownian dynamics or Monte Carlo methods rely due to their stochastic nature on random numbers. The quality of the results produced by such simulations depends partly on the quality of the random number generator. For application in computer simulations theses generators must have several features. The numbers produced must pass important tests of statistical independence and have periods which are so long that, for practical purposes, values from these generators can be considered as independent.

Unfortunately there is no generator available ensuring complete randomness, but the list of available algorithms with increasing quality is growing. This reduces the risk of applying a particularly bad one in a simulation.

Computational efficiency becomes extremely important for the simulation of stochastic processes which require vast amounts of random numbers. The generation of 10^{10} random numbers for the simulation of dynamical problems is nothing special anymore so that the computation of a single random number has to be very fast. This simulation program for instance, handles up to 3×10^5 electron-hole pairs and for every iteration step 10^6 random numbers have to be calculated.

The random number generator used in this simulation is the routine available in the CERN program library called RANLUX (see [69]and [70]). It generates pseudo-random numbers uniformly distributed in the interval (0,1) where the end points are excluded. Each call to this routine produces an array of single-precision real numbers. A luxury level between 0 and 4 can be chosen which guarantees the quality required for the specific application. The lowest level (0) gives a fast generator which will fail some sophisticated tests of randomness; The highest level (4) is about five times slower but guarantees randomness with high accuracy. In all cases the period is greater than 10^{165}.

7.2 Charge Injection

Injection coordinate and injection angle are randomly generated within a defined range. In the experiment, a slight divergence of the pion beam is observed. Accordingly, the injection angle varies around the initial grazing angle by $\pm 0.5°$ corresponding to the real pion beam (section 5.6 actually, the measured divergence is $\pm 0.3°$). With an initial angle of 8° the track length varies around $\pm 150\mu$m.

In order to avoid events which are rejected, the possible y and x impact coordinates are limited to the boundaries required by the analysis program (see section 6.1).

The operation mode of thin silicon detectors used for the observation of the transit of charged particles is based on the ionisation J (electron-hole pair generation) produced in the detector for each particle passing through it. This generation J is related to the total energy loss Δ of the particle. Both Δ and J are stochastic quantities. The charge injection mechanism is treated within a Monte Carlo routine by Roland Horisberger based on a review of Hans Bichsel [66]. This routine calculates the random energy loss within a 10 μm^3 silicon cube according to the Bichsel straggling. Straggling function is the usual expression used for the probability density functions $f(\Delta)$ and $\phi(J)$.

Moderately relativistic charged particles other than electrons lose energy in discrete amounts of E in independent, stochastic single collisions. The differential energy loss ($\frac{dE}{dx}$) is given by the Bethe-Bloch equation [17]. Only for a thick layer $(dE/dx)\delta x \gg T_{\max}$, where δx denotes the material thickness and $T_{\max}$ is the maximum kinetic energy, the straggling distribution becomes nearly Gaussian. For thin absorbers this energy loss is not Gauss-shaped anymore and shows a characteristic tail extending towards higher energies.

Landau [67] used a transport equation describing the change in $f(\Delta)$ and then solved this equation with Laplace transforms. His function known as Landau distribution describes the energy deposition by ionisation very well. Applied for in thin silicon absorbers this function predicts the correct width, but it will not describe the appropriate shape and the precise value of the most probable energy loss.

The Bichsel straggling proves to be an accurate description of the distribution which simulates the interaction of the charged particles in the detector by a Monte Carlo method. It is a convolution of functions which describe interactions of charged particles with matter (especially for silicon).

For this method it is necessary to have a knowledge of the energy-loss spectrum $\sigma(E)$ for single collisions. The passage of each particle thorough the detector is followed from one collision to the next. The distance travelled between collisions as well as the energy loss E in the collision determined by random numbers. These individual energy losses are added up to the total energy loss Δ of the particle

$$\Delta = \sum_i E_i. \tag{7.1}$$

The calculation is repeated for N particles. An important assumption is that successive collisions are statistically independent. In this case the number of collisions experienced by the particles is described by the Poisson distribution

$$P(n) = \frac{m^n}{n!} e^{-m}, \tag{7.2}$$

where $P(n)$ gives the fraction of particles suffering n collisions and m is the average number of collisions for all particles. This average number is defined by $m = M_0 d$, with the sensor thickness d and the total collision cross section M_0.

The probability density function for n collisions is given by the n-fold convolution of the single collision spectrum $\sigma(E)$

$$\sigma(\delta)^{*n} = \int_0^{\Delta} \sigma(E)\sigma^{*(n-1)}(\delta - E)dE, \tag{7.3}$$

with

$$\sigma(\Delta)^{*0} = \delta(\Delta) \quad \text{and} \quad \sigma(\Delta)^{*1} = \sigma(\Delta).$$

The complete straggling function then is

$$f(t,\Delta) = \sum_{n=0}^{\infty} \frac{m^n e^{-m}}{n!} \sigma(\Delta)^{*n}. \tag{7.4}$$

Sometimes during charge injection using the Bichsel straggling high numbers of charge carriers are generated within a small region. This behaviour can also be interpreted as the production of energetic knock-on electrons (δ-rays). The consequence of this production was tested in a separate program [61] and the influence on the street shape was found to be negligible. For unrelativistic particles the δ-ray angle of emission with respect to the incident particle track is given in good approximation by [68]

$$\cos^2(\theta_\delta) = E_\delta/(E_\delta + 2m), \tag{7.5}$$

with the electron mass m. This means that θ_δ usually is close to 90° which is not considered for generating the street profile.

7.3 Diffusion

Diffusion is a stochastic process which can be simulated using the random walk method. Suppose, a particle is placed anywhere on the lattice, this point serves as the origin. At each time step the particle hops to one of its nearest neighbour knots in the lattice. For a two dimensional lattice the particle has four possibilities: up, down, left and right. The essential feature of random walk is that the particle at each time step has the choice of any of the four nearest neighbours including the one where it came from.

In one dimension, diffusion can be described using a simple game of dice with a left-right option for each charge carrier. A good approximation for a Gauss distribution is obtained if two presuppositions are fulfilled. A large number of particles have to be involved into this game and it has to be repeated several times.

The Gaussian distribution can be derived from the binomial distribution if the number of trials $n \to \infty$ and the probability p is kept constant. Starting from the binomial distribution $P_B(x,n,p)$, its mean $\mu = np$ and variance $\sigma^2 = np(1-p)$ one defines the new variable $z := (x-\mu)/\sigma$ and the function $\varphi(z) = \varphi(x,n,p) = \sigma p_B(x,n,p)$. The differential of $\varphi(z)$ is defined as

$$\frac{\mathrm{d}\varphi}{\mathrm{d}z} = \lim_{\Delta z \to 0} \frac{\varphi(z+\Delta z) - \varphi(z)}{\Delta z}. \tag{7.6}$$

If $\Delta z = 1/\sigma$ is chosen in correspondence to an increment of 1 in x and performing some algebraic calculations

$$\begin{aligned} \frac{\varphi(z+1/\sigma) - \varphi(z)}{1/\sigma} &= \sigma\varphi(z+1/\sigma)\Big(1 - \frac{(x+1)(1-p)}{(n-x)p}\Big) \\ &= \Big(-z + \frac{p-1}{\sigma}\Big)\varphi(z+1/\sigma)\frac{1}{1-pz/\sigma}, \end{aligned} \tag{7.7}$$

is derived.

For $n \to \infty$ and constant p in equation (7.7) on the left hand side, $\Delta z = 1/\sigma$ will go to 0 and we get the following equation:

$$\frac{\mathrm{d}\varphi}{\mathrm{d}z} = -z\varphi(z). \tag{7.8}$$

Here, $\varphi(z)$ is a Gauss function with $\varphi(z) = C\exp(-z^2/2)$. Normalised and expressed as a function of x, μ and σ the Gauss distribution is derived

$$P_G(x, \mu, \sigma) = \frac{1}{\sqrt{2\pi}\sigma}\, e^{-\frac{1}{2}\left(\frac{x-\mu}{\sigma}\right)^2}. \tag{7.9}$$

Therefore, the binomial distribution can be approximately described by the Gauss distribution. Already for $np > 4$ and $n(1-p) > 4$ the Gaussian shape is sufficiently reproduced by a binomial distribution.

This relationship is useful for the numerical model of diffusion. Here, the simple game of dice in three dimensions describes diffusion in the detector.

At $t = 0$ a number of charge carriers are assumed to be located in one point. Because of the concentration gradient they dissolve in a Gaussian distribution around the origin. The differential charge concentration $\mathrm{d}N/N$ can be described in one dimension with [26]

$$\frac{\mathrm{d}N}{N} = \frac{1}{\sqrt{4\pi Dt}}\quad e^{-x^2/4Dt}\mathrm{d}x. \tag{7.10}$$

Compared with equation (7.9) the mean deviation σ_x can be related to

$$\sigma_x = \sqrt{2Dt}. \tag{7.11}$$

By knowing the diffusion coefficient D (described in equation (3.14)) for electrons and holes in silicon this relation can be used to calculate the width of the Gauss distribution after a time interval Δt. Or vice versa, after repeating the game several times on a number of particles the time base for one iteration can be calculated by the obtained spread.

This concept is used to determine the step width with which an electron or hole diffuses if one iteration in the simulation should correspond to 10 ns in real time. If the particle just has the freedom to move in one dimension ($\pm x$), equation (7.11) could be employed to calculate the step width. In the three dimensional case the particle has six options to move[11]. The mean deviance of the three dimensional case is related with $\sigma_{x,y,z} = (1/\sqrt{3})\ \sigma_x$ to the deviance in one dimension. Therefore the step width in a specific direction has to be larger than in the one dimensional case if the same result has to be produced.

Figure 66 shows the result of the diffusion of a point like charge cloud after several iterations. A random generator creates a number between 1 and 2 for the one dimensional case and between 1 and 6 for the three dimensional movement. Each number corresponds to a motion into a certain direction.

The movement of electron-hole pairs within one iteration corresponds to 10 ns in realtime. It comprises a full drift and diffusion calculation of all participating electrons and holes.

In order to explain the late charge hypothesis from section 6.3 diffusion was the prior subject studied by the simulation. But the iteration time of 10 ns is not an adequate time scale to investigate drift which is therefore treated on a shorter time scale within the diffusion routine.

7.4 Drift

For simulating the drift velocity equation (3.9) is employed to calculate the step width of a carrier depending on its mobility and on the electric field. It only acts along the z-axis. According to the applied bias voltage (-300 V at the p-side) electrons are sweeped towards the n^+-pixel side ($z = 0$) while the holes move to the p^+-side ($z = 300$).

11. $\pm x$, $\pm y$ and $\pm z$

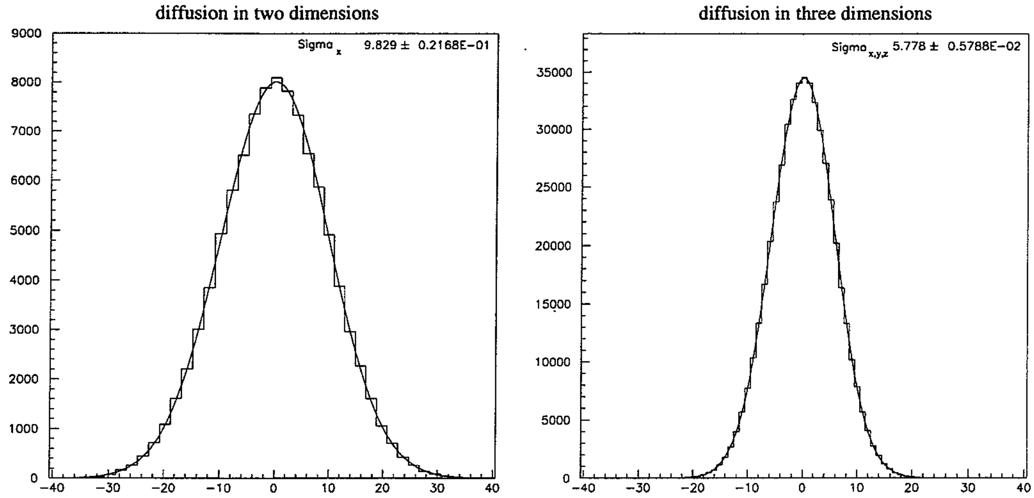

Figure 66: Simulation of a diffusing particle clout with its origin in 0. The left figure shows the charge distribution when only two options of motion (left right) are at disposal. The right figure presents the same plot but with six possible moves. The mean deviation σ is transformed into the other by $\sigma_{x,y,z} = (1/\sqrt{3})\ \sigma_x$.

In the space charge region drift is the dominating motion and the charge collection process is complete after a few nanoseconds. Therefore, drift is considered in time bins of 0.1 ns. This refining parameter is adjustable in order to study a more detailed motion. Diffusion is of minor importance in terms of charge collection time but not negligible. The diffusion step size is automatically scaled with the refinement parameter which is active in the depleted region.

The electric field distribution along the depleted volume is calculated from the applied bias voltage using equation (3.17). From this distribution the step width $\Delta s_{\rm e,h}$ of a charge carrier is derived employing equation (3.9)

$$\Delta s_{\rm e,h}(z) = \mu_{\rm e,h} \cdot \Delta t \cdot E(z). \tag{7.12}$$

The step width Δs per time interval Δt (=0.1 ns) depends on the electric field strength at the given position z. This position is calculated in steps of 1 μm and the corresponding width is stored in lookup tables for electrons and holes individually.

Within the simulation the carriers are sequentially treated by their array number. In a second step it is determined if the corresponding z-coordinate localises the particle within the depletion region. If this, for example, is confirmed for an electron it is drifted in steps which correspond in real time to 0.1 ns. This procedure is repeated until the electron is trapped or has reached the n^+-pixel side. If none of these conditions is fulfilled (after 100 iterations) the routine is stopped when the drift time is in accordance with the diffusion time interval of 10 ns. In the next iteration the corresponding particle is then considered again.

Figure 67 demonstrates the drift of a hole in constant time steps of 0.1 ns from the n^+-side to the p^+-side. Here it is calculated with an electric field where the maximum field strength is on the p-side. This is the case before type inversion.

From initially small step sizes because of the small electric field on the n^+-side it is accelerated towards the p^+-side. Diffusion is not considered in this example. Because of its smaller mobility it takes the hole roughly 16 ns to traverse the 300 μm thick detector. In contrary, the electron which is released on the p-side senses a strong electric field and is accelerated towards the n-side. With decreasing field strength the step width per 0.1 ns decreases too. Nevertheless the drift time is about 6 ns because of the mobility which is for electrons three times larger.

7.5 Provision for radiation effects

In the experiment the radiation effects are perceptible by a decrease of the depletion volume and by an increase of the trapping charges. The tail of the street profile which is experimentally

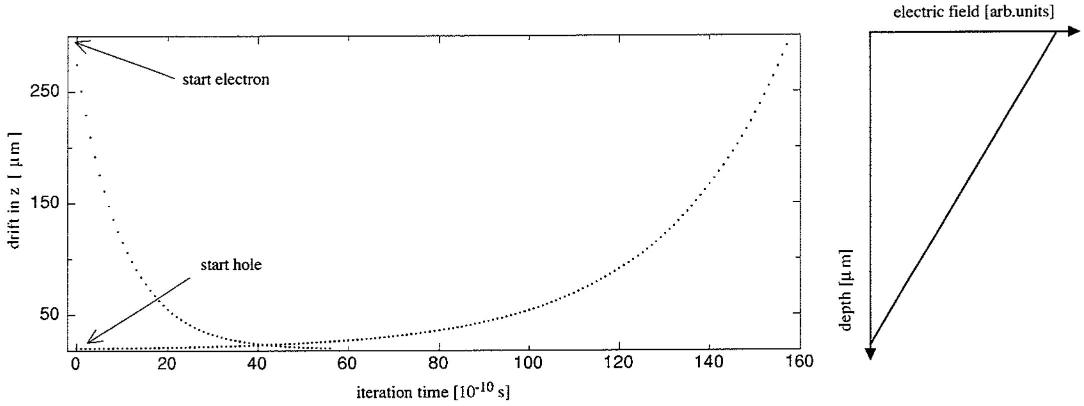

Figure 67: Drift stages of a hole moving from the n^+-pixel (z=0) side to the p^+-side (z=300) as function of the iteration time in steps of 0.1 ns. The electron starts from the opposite direction and is about three times faster because of its mobility. This is the simulation for the unirradiated case where the junction is on the p-side of the sensor considering a potential drop of 120 V for full depletion as obtained from figure 19.

observed is evidently generated within the undepleted region reaching the readout late in time (section 6.3). It is suspected that a small electric field must still be active within the undepleted region (references [60] and [50]).

This simulation is dedicated to describe the results of the grazing angle method discussed above which is tested on n^+-pixels in n-type (after type inversion p-type) material. Therefore the junction is defined to be on the n^+-pixel side after type inversion. This has also an effect on the behaviour of the electric field. With the junction the maximum field strength has changed and is now on the n^+-pixel side (z=0). Figure 68 presents the situation after type inversion. The hole is

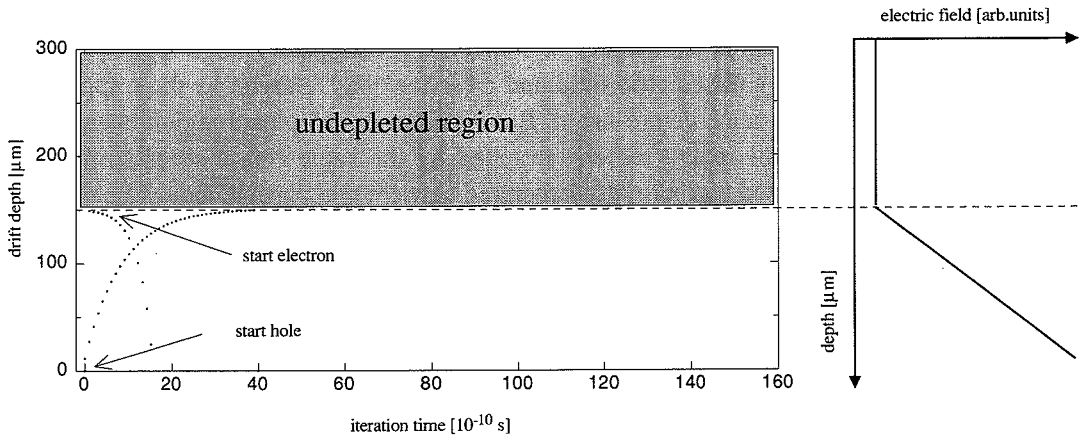

Figure 68: Changed direction of the electric field. After type inversion the maximum field strength is found on the n^+-pixel side. Because of the high field the particles cover the reduced drift distance in shorter time.

pushed away from a strong electric field below the pixels and the electron starts in moderate steps from the edge of the depletion zone.

Trapping effects

Trapping effects are caused by an increased number of trapping centres. These centres decimate the number of free charge carriers and thus the average lifetime of each carrier is decreased.

In the simulation this trapping time $\tau_{e,h}$ (see equation (3.27)) is treated as free parameter to fit the results to the experimental data. This fitting is not yet automated by a minimisation like the χ^2 method but numerous iterations have produced reasonable results (see section 8).

According to equation (6.4) trapping time describes the reduction of free charge carriers. This equation is employed by the simulation to calculate a trapping probability for each carrier within the depletion region (see above).

For a given trapping time equation (6.4) is employed to calculate the percentage of trapped carriers after 0.1 ns. This percentage gives a measure which is tested on each time step and on each carrier individually by generating a random number. If the random number is above the measure the carrier remains free otherwise it will be trapped. Once trapped carriers have induced their mirror images they are not considered anymore.

Reduced depletion depth

Simulation of a reduced depletion volume is realised by shrinking the active drift zone to a certain depth (150 μm for example). Within the remaining region only a small electric field (or no field at all) is assumed. Because of the slower diffusion process this region is not considered within the fine time scale of the drift and movements of the carriers are updated in steps of 10 ns.

Trapping remains active but recombination of electrons and holes is not considered. This is justified by the diffusion length. Diffusion length for electrons is defined as

$$L_e = \sqrt{D_e \tau_e}. \tag{7.13}$$

Typical charge carrier lifetimes τ are of the order of 10^{-8}s. With an electron diffusion coefficient (equation (3.14)) of 35 cm^2/s a drift length of about 60 nm is calculated for electrons [71].

If an electric field is assumed a free parameter can be adjusted to a certain voltage which drops over the entire undepleted volume. According to the electric field profile model as shown in reference [60] this drop leads to a uniform electric field strength which is independent of the position in the undepleted zone.

Another parameter which can be used to fit the experimentally observed tail is the trapping probability within the undepleted volume. Although the causing effects are unclear, it is possible to introduce a time different from the trapping time for electrons and holes considered in the depleted region. From diamond similar observations are reported. It is believed that trapping centres are permanently occupied within the undepleted region. Within the space charge region free charge carriers are sweeped away by the electric field and a carrier ones released by the trapping centre will not be retrapped by the same centre again. But within the undepleted region charge carriers mostly remain within a small spatial region retrapped by the same centre several times. These occupancies can also be caused by thermally generated carriers and particle induced electron-hole pairs could have apparently longer trapping times than in the depletion region.

Therefore, with this parameter it is possible to tune the trapping probability by factors. Factor 1 stands for the same trapping time as in the depleted region. Bigger than one stands for longer trapping times and vice versa, small trapping times are achieved with a factor less than one.

As soon as an electron reaches the depletion region it abruptly senses the electric field and starts its way towards the collecting pixels (figure 68). In contrary, a hole sensing the edge of the depletion region is set back into the undepleted region without an effect on the readout.

Charge which is trapped within the undepleted zone is also assumed to have no effects on the pixels. This assumption is not valid for small depletion volumes. As shown in figure 74 charge trapped far from the sensing surface has little effect on the induced charge and the above assumption holds for depletion regions above 125 μm. Below this depletion depth charge trapped within the undepleted region has to be considered as well. This is not yet done in the present simulation.

7.6 Induced signal by trapped charge

Turning to the experimental data it seems that trapped charge remains electrically active. The charge of a trapped carrier is not shielded and it induces image charge that contributes to the integrated signal which is visible at the amplifiers.

Figure 69 displays again the street profile obtained from a sensor at 300 V bias and 20 days after irradiation with a fluence of 6.3×10^{14}/cm^2 (figure 44). In addition the signals of the neighbour streets are made visible. Every time, a pixel street candidate was found by the offline analysis program the signals of the corresponding adjacent pixels ares recorded as well leading to the presented shape. The model in figure 70 describes how the observed effect from figure 69

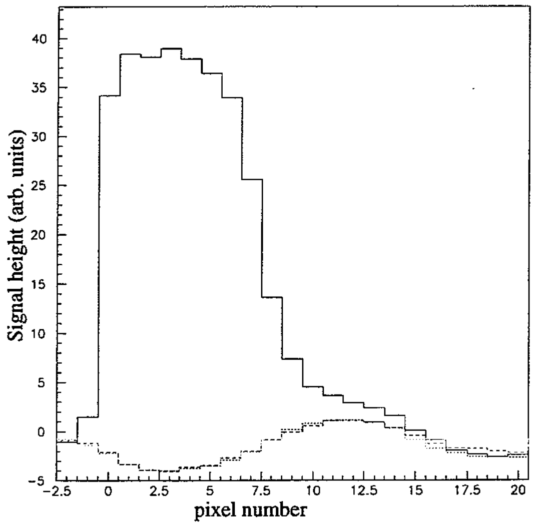

Figure 69: Same street profile as in figure 44. In addition integrated signal of the adjacent pixel rows is plotted.

can be interpreted by induced charges. On the left of figure 70 the sketch in case of no trapping is

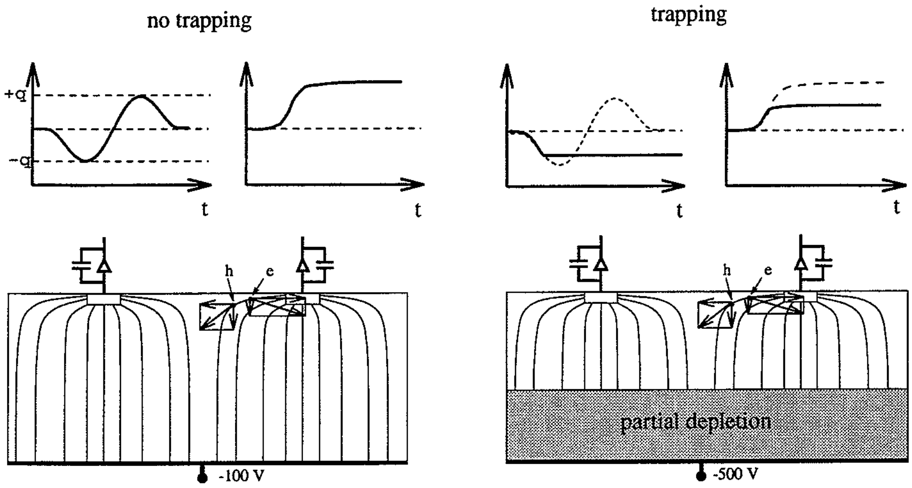

Figure 70: Here, both scenarios are presented. Left: no trapping assumed, right: with trapping. Above the figures the charge signal as function of the time is plotted for the charge collecting and the neighbouring pixel.

shown. As soon as the electron-hole pair is generated they drift apart along the electric field lines. The negative charge drifts towards the collecting pixel. Long before it has physically reached the pixel the amplifier senses the induced charge. As long as the hole is in the neighbourhood this charge is partially compensated. When the hole is remote and the electron has reached the readout the full charge of the electron is considered.

Beneath the n^+-side the electric field lines are focused towards the implants. The hole which moves along the field lines has a drift component directing to the neighbour pixel. This component induces a negative swing in the adjacent amplifier. As it moves further this component vanishes and the amplifier 'sees' a positive charge drifting away inducing a positive swing. Integrated over the entire charge collection process this is averaged to zero.

This model implies that in case of no trapping the above signal in figure 69 is not observable in an unirradiated sensor since there the trapping time is longer than the charge collection time.

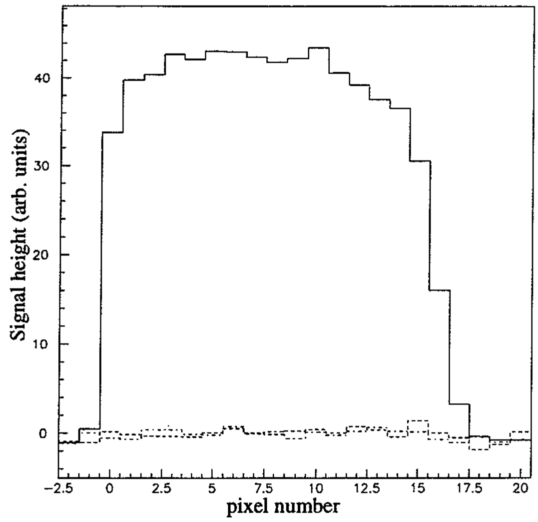

Figure 71: The street profile of the unirradiated sensor accompanied by its nearest neighbour rows. Here the peculiar shape as in figure 69 is not observed.

Figure 71 gives the prove for this prediction. Here, the peculiar shape of the neighbour rows is not observed which supports the accuracy of the above model.

The origin of the neighbour row shape in case of trapping is illustrated on the right of figure 70. The record of movements remains the same as described above with the difference, that this series of motions can be stopped immediately by a trapping process. The example in this figure considers the case of a trapped hole. Here, the hole is trapped as long as a drift component points towards the neighbour pixel. Therefore, the induced charge is frozen when the hole stops in its movement leading to a negative charge integral. But also the main collecting pixel is affected. The electron may reach the amplifier but part of its charge remains compensated, biased by the trapped hole.

Figure 72: Solution by method of images. The original potential problem is on the left, the equivalent-image problem on the right.

In the simulation this effect has to be considered if parameters such as the trapping time should be resolved with this model. Therefore, the induced charge depending on depth and polarity of the carrier has to be calculated. On the left of figure 72 charge located in front of an infinite conducting plane at zero potential is shown which is employed for the calculation.

The actual charge density induced on the surface of the conducting plane can be obtained by the method of images [73]. This method introduces an equal charge with opposite polarity located at the mirror-image point behind the plane defined by the position of the conductor (on the right in figure 72). Regarding the behaviour of the electric field lines and the resulting forces this measure has the same effect as the described problem. In case of one conducting sphere a simple analytical solution can be found [73].

The simulation has to deal with a more involved model because of a second conducting plane close to the one introduced above. The electric field lines emanating a point charge which is located between two planes are split up. Therefore a second image charge has to be introduced opposite of the second plane. But because of interference between these two image charges extra virtual charges are needed. On both sides of the two conducting planes additional image charges are introduced in order to achieve a good approximation of the charge density induced on the two conducting planes. This situation is illustrated in figure 73. The numerical simulation dedicated to this problem deals with ten of such image charge pairs leading to a solution with an accuracy on the 1% level compared to the exact analytical solution which needs an infinite number of image charges in both directions.

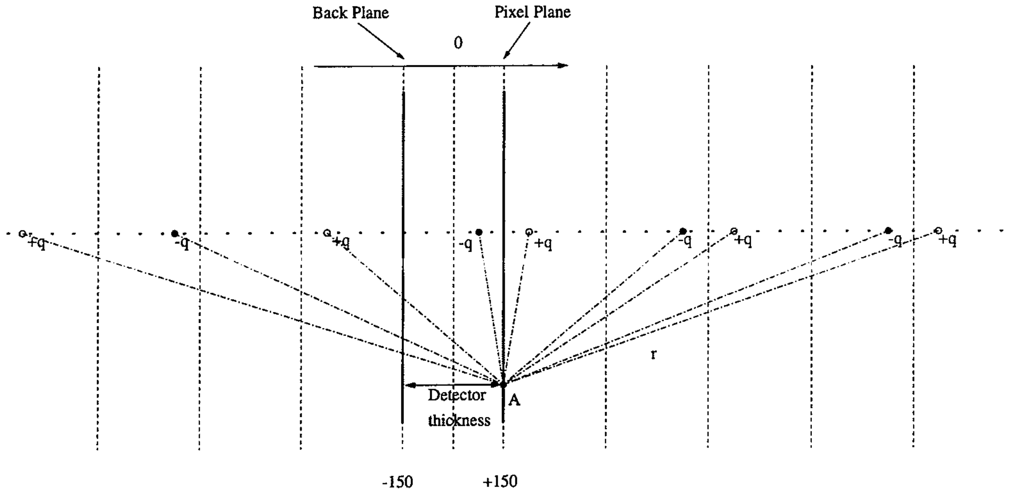

Figure 73: Model to explain the numerical method used to calculate the charge distribution which is induced by a charge carrier situated inbetween two conducting planes.

This numerical program calculates the induced signal of a positive charge in between the planes of a silicon detector. The induced charge is calculated in steps of 5 μm for a detector thickness of 300 μm. Figure 74 shows the distribution of the induced charge collected by the pixels at four different distances to the surface. Each plot corresponds to the charge distributed over an area of 5×5 pixels.

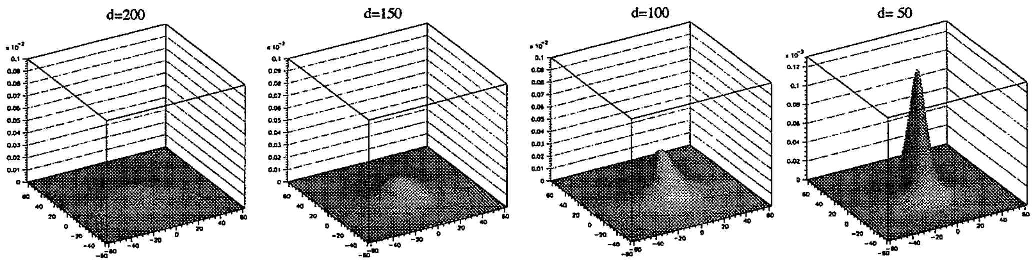

Figure 74: Distribution of the induced charge as function of different distances. The distance of the electron to the sensing pixels is described with d (in μm).

The result of this simulation is stored in a look up table. The actual induced charge of a trapped carrier is used to calculate the integrating charge on the preamplifier.

7.7 Magnetic field effects

As reported, data using the grazing angle method was recorded under the influence of a magnetic field (section 6.7). The simulation provides the option to consider magnetic fields of any strength which act perpendicular to the electric field. The deflection of the moving carriers due to the magnetic field is introduced to the simulation employing the simple state of motion introduced in equation (3.31).

A closer look to the detailed theory of the dynamics of semiconductors in electric and magnetic fields things are not as simple as it is considered here. Terms such as magneto resistance and cyclotron resonance come into play. But these theoretical approaches describe microscopic effects which have no or little effect on the observed signal formation. In the awareness that this investigation is aimed at the explanation of macroscopic effects pragmatic recipes are used to describe the observed phenomena.

Therefore the magnetic field effect is kept simple and only treated as a second force which acts perpendicular to the electric field. Every time a carrier moves a distance Δs by the electric field the fraction which the particle is deflected by the magnetic field is calculated by $\Delta s \cdot \tan\theta$.

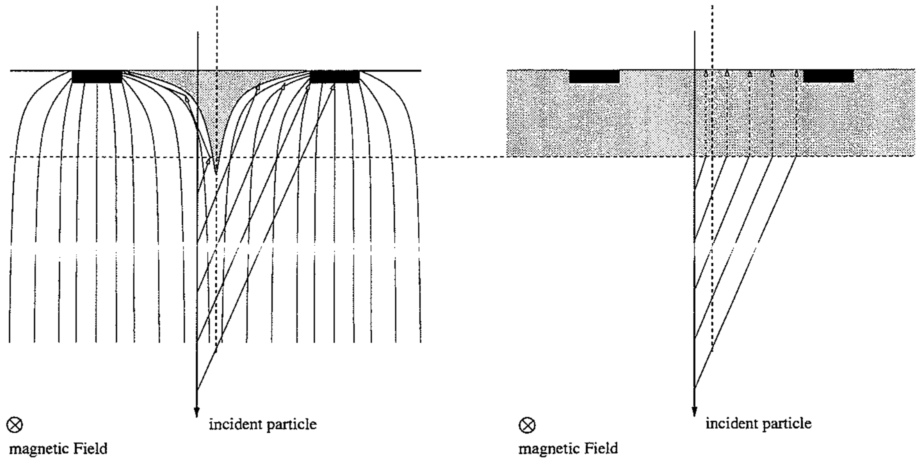

Figure 75: Left: hypothetical explanation for the observed bend in figure 64 by disturbances in the electric field underneath the surface. Right: model to simulate this hypothesis.

A peculiarity is a region which is introduced below the charge collecting pixels (z=0). This region is variable in depth and within, the Lorentz force can be optionally disabled. As mentioned, the electric field lines in this simulation are considered to be all in parallel within the entire depletion region. The observed bend in figure 64 can be explained by deformations of the electric field. In order to feign these deformations a region disabling the Lorentz force is supposed to have the same effect as a deformation of the electric field lines.

Figure 75 illustrates this effect. On the left side the hypothesis is drawn how the charge collection process is influenced by the disturbance of the electric field lines which are focused towards the implants. In case of underdepletion a considerable region of small electric field strength remains between two pixels (grey pattern). A charge carrier following the electric field line starts changing is direction towards the pixel. This reduces the velocity vector perpendicular to the magnetic field. Therefore, from a certain distance below the surface, charge is not further deflected by the Lorentz force.

The right drawing in figure 75 illustrates the model which is used in the simulation. At a certain depth below the surface the Lorentz force is disabled and therefore the charge drifts without further deflection towards the surface. The result of this simulation compared with the data is given in section 8.2.

8 Simulation Results and Comparison to the Experiment

The result of the simulation described in section 7 is contained in a simple data file. The structure of this file is similar to the format of the experimental data. But natural pedestal variations and stochastic baseline fluctuations are missing.

In combination with the time rise study (section 6.3) long pedestal values have been recorded ($\sim$ 5000 events). This real pedestal file from the experiment is used to be merged with the numerical generated events faking a real data file which can be used by the analysis program.

To each second pedestal event the numerical numbers are added. Only every second event is used because of the necessary pedestal updates in between (see section 6.1). The analysis program notices automatically and with high efficiency (only about 1% of the simulated events and pedestal updates are missing) if an event is to be used as pedestal update or for adding to the street profile.

The primary aspect of the simulation is to generate a set of numerical data which comes as close as possible to the reality. It should involve the all the models which conclude from observations in the experiment. Therefore each event was created using a random charge generation along the particle track. As with the real data high statistics and integrated over many events generates the picture that is expected for a homogeneous charge distribution.

In the simulation there is a shortcut for this process. Instead of randomly generating the charge along the particle track a defined portion of charge can be created. On this single event certain effects can be studied without a vast amount of CPU time.

Some of the following results use this advantage is a kind of previewing mechanism. It is used to demonstrate the effects of some free simulation parameters such as trapping time or depletion depth.

8.1 Reconstruction of the depletion depth profile

Fortunately not all parameters used in the simulation are undefined. For instance the depletion depth for a given bias voltage is subject of the experimental measurement and can be used as input parameter. Also the grazing angle is a given parameter. For other parameters such as trapping time a model or an approximation can be found predicting at least the order of magnitude. Others are completely unknown such as the electric field strength or the trapping time in the undepleted region.

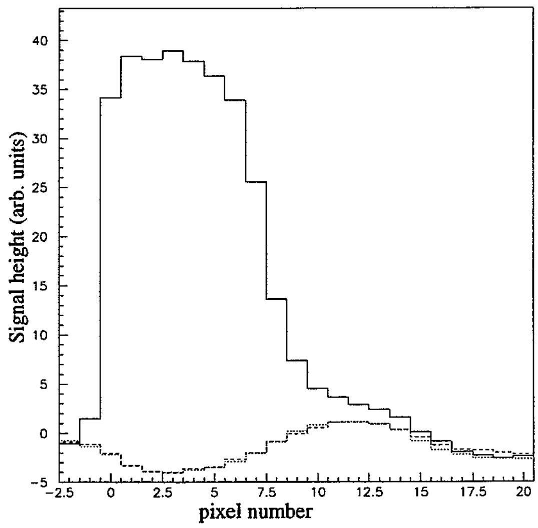

Figure 76: Copy from figure 69 showing the street profile with the neighbour rows included.

The following figures will show the evolutional adaption of these parameters in comparison with the experimental result. Focus of the simulation is the reproduction of the street profile from figure 69 which is here displayed again in figure 76.

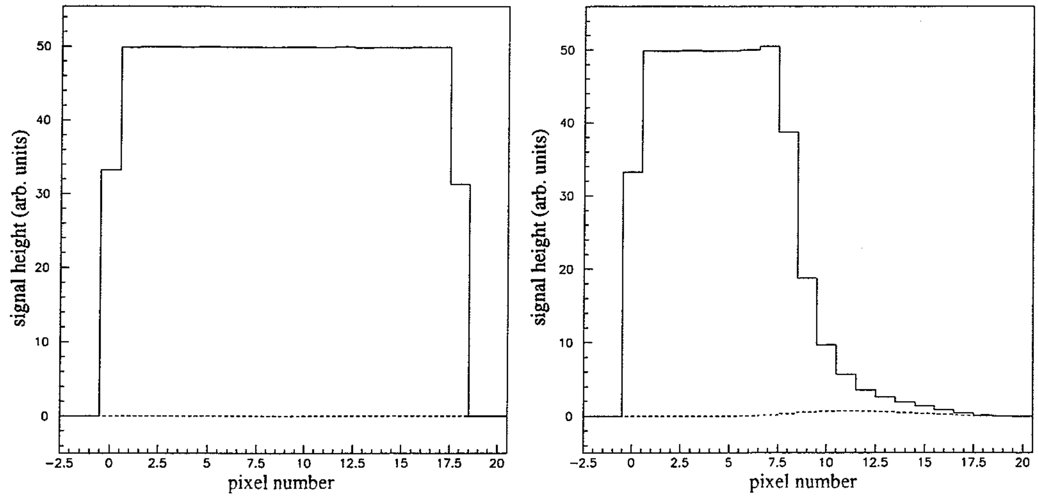

Figure 77: Left: simulation of the unirradiated sensor.

The following figures can be considered as a slide show where the evolution of the free parameters and their effects are scrutinised. They are all created using a single event with homogeneous charge distribution. The pulse hight is generated by using the ADC-key obtained in section 6.4 where 248 electrons correspond to one ADC channel. If not especially mentioned, the simulated charge collection time (which corresponds in the experiment to the integration time) is set to 300 ns.

The left of figure 77 shows the starting point where all radiation induced effects are disabled. Trapping time is set in the order of micro seconds and the sensor is fully depleted.

Additionally to clarify the influence of the induced charge by trapped carriers the neighbour streets are shown as well. The width of the street including 17 pixels gives the expected depletion depth of 300 μm for an angle of 7.6°. The first pixel in the row always shows less charge than the others. This is explained by the charge injection. The impact coordinate of simulated particle is in the centre of the first pixel and therefore only a part of the charge is collected.

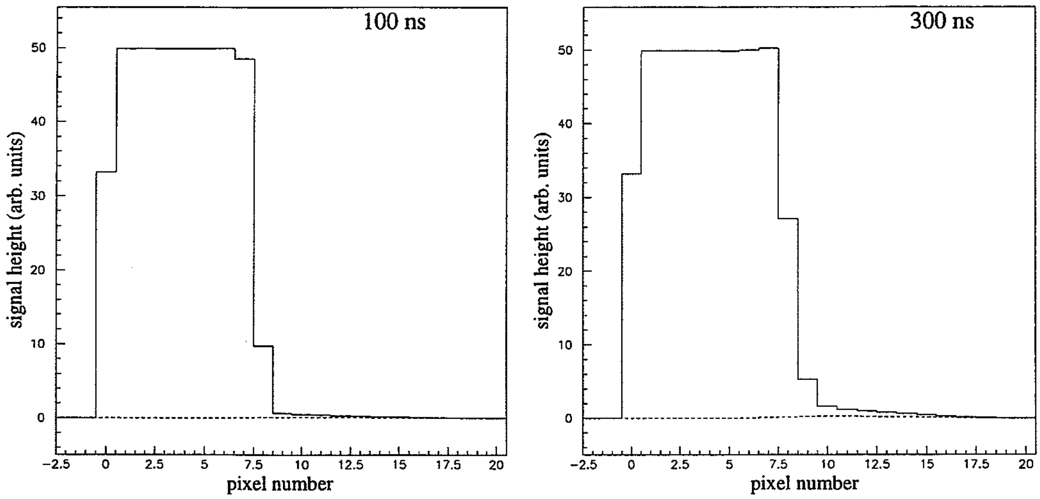

Figure 78: Effect of a reduced charge collection time. Left: 50 ns, right: 100 ns maximum charge collection time.

On the right of figure 77 the depletion volume and the charge collection time were changed. The depletion depth is now decreased to 150 μm and the collection time is increased to 1.5 μs. From the eighth pixel on the charge origins from the undepleted region. Diffusion is the main transport mechanism and not every carrier 'finds' its way to the depletion zone. Therefore, the fraction of missing charge increases with increasing depth which explains the decreasing pulse height.

But still a number of charge carriers reach the readout from the undepleted region. This is not so astonishing when reminding that trapping and charge collection time are in the order of micro seconds.

Charge origin from the undepleted region is late in time as it was shown in the experiment (section 6.3). This is caused by the slower motion process of diffusion. If the simulation properly reflects the experiment this diffusion caused tail should also vanish when the charge collection time is reduced.

Figure 78 shows the resulting street profile. Left: a maximum integration time of 100 ns is chosen and right: with a charge collection time of 300 ns. After a time of 100 ns only this charge has reached the readout which was created within the space charge region. A small number of charge which was close to the transition between depleted and undepleted region is also collected by the readout. After 300 ns more and more charge carriers diffuse from the undepleted region reaching the readout.

Trapping

In the following, charge collection time will be again at 300 ns and the right profile in figure 78 corresponds to the situation when no trapping is assumed. In case of trapping this situation changes dramatically. The following figures use the trapping times calculated from equation (3.28). For the electron trapping τ_e=1.38 ns and for the hole τ_h=6.17 ns is found simulating a fluence of $6.3\times10^{14}/cm^2$.

The plots in figure 79 are obtained by partial introduction of trapping time. Enabling electron trapping results the street shape on the left. The plot on the right shows the situation if only hole trapping is active.

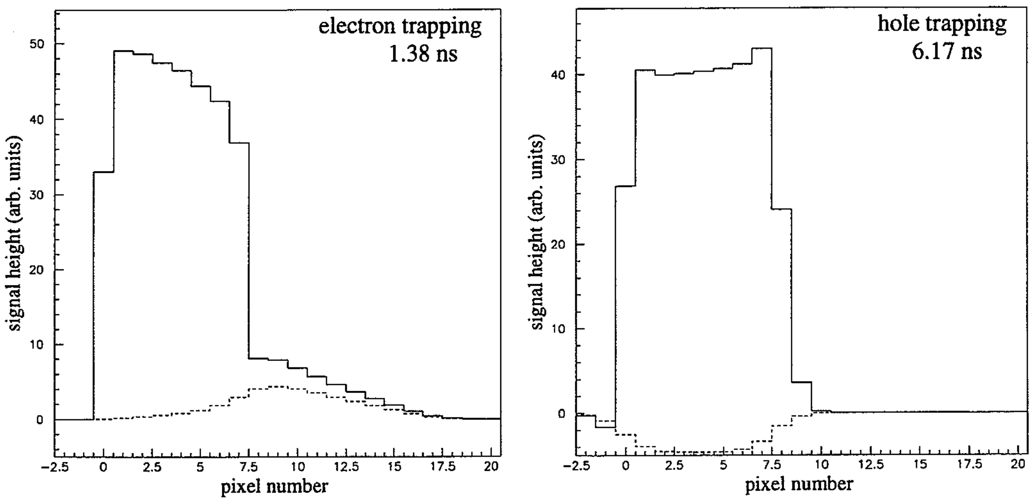

Figure 79: The influence of trapping on the street profile. Left: situation where only electrons are trapped. Right: hole trapping.

By considering the trapping effects which are individually caused by electrons and holes some conclusions can be drawn. Trapped electrons are responsible for the shape of the end of the row. And holes form the shape of the beginning of the street. This is caused by the different drift directions. Holes move away from the readout and have to transverse the entire depletion region before the are consumed by the undepleted region. Most of these holes are trapped and only a small fraction reaches the transition between depleted and undepleted region. The induced charge of the trapped holes causes a decrease of the pulse height on the first pixels and a negative swing on the neighbour pixels.

Electrons generated near the readout sense a strong electric field and reach the readout before they become trapped. Trapping increases with increasing depth and a rise in the induced charge on the main road and on the neighbour pixels is noticed. The observed tail from the undepleted region is caused by induced charge of trapped electrons. This tail should vanish when both trapping constants are active and the holes are trapped too. In this case the electron induced signal is compensated by the hole charges.

Figure 80 displays the situation when both effects, hole and electron trapping are active. In this case, the tail induced by trapped electrons is no longer observable. All known radiation

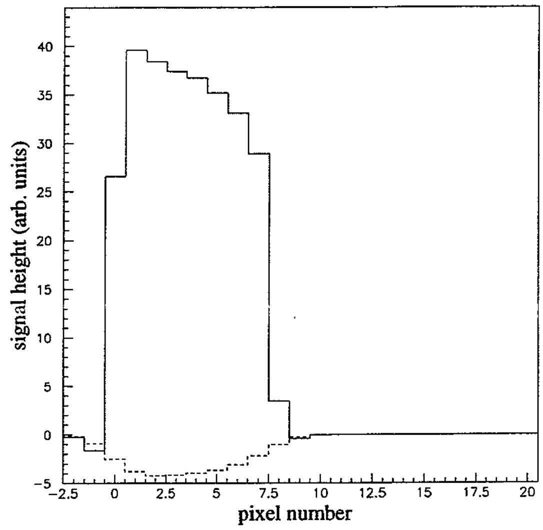

Figure 80: Electron and hole trapping are active. The observed tail from the left of figure 79 is not observed. This is explained by the induced charge which is compensated by the trapped holes.

damage induced effects are considered but compared with the experimental data there is a difference regarding the tail. There is no use to elongate the charge collection time because of the short carrier lifetimes. Are there alternative mechanisms responsible for this experimental observation?

Generating the tail

Two possible effects can be used to explain this observed tail. As suspected by reference [60] a rest electric field could have survived in the undepleted region. In this case the word 'undepleted' looses its validity because it describes a field free region. The other possibility is the trapping time itself. If, for a strange reason the trapping constant is not valid in the entire sensor the tail can be generated by the simulation as well.

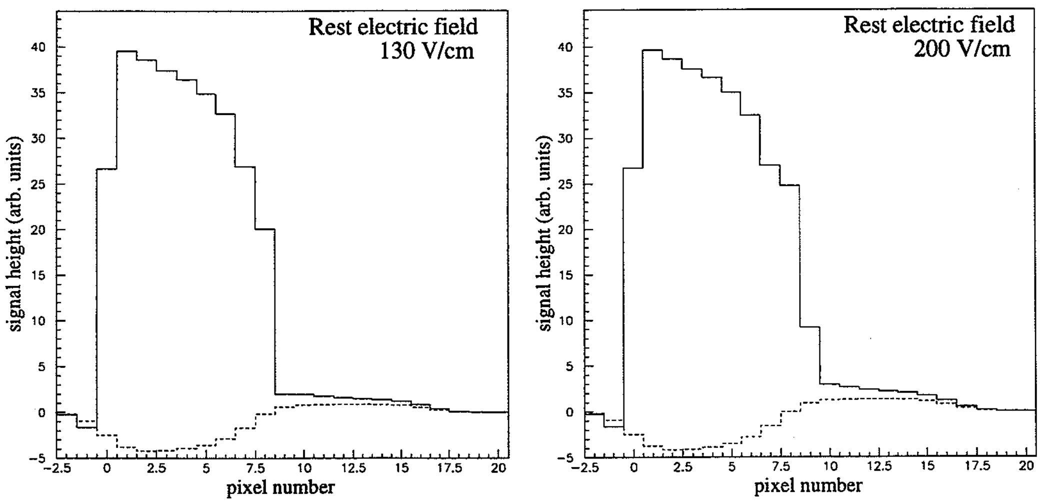

Figure 81: Change of the tail shape depending on the voltage drop over the undepleted region.

First the electric field hypothesis should be scrutinised. Figure 81 shows the change of the street profile depending on the rest electric field (130 V/cm and 200 V/cm) in the undepleted region.

An explanation what mechanism should cause a change of the trapping time within the undepleted region is not available yet. The most realistic assumption is that the undepleted region acts in terms of trapping as intrinsic silicon. Here, the recombination time determines the carrier lifetime which is in the order of ~300 ns. With this as input the plots in figure 82 are generated.

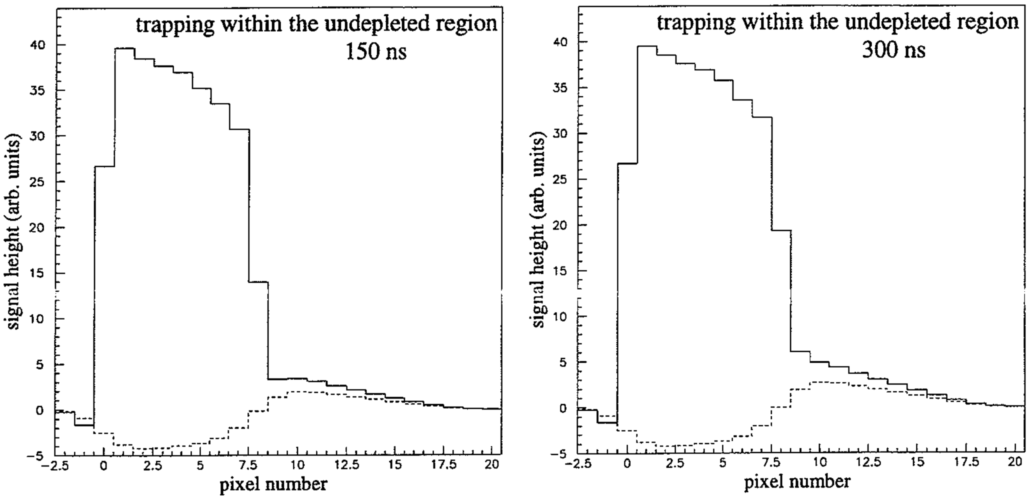

Figure 82: Forming of the tail because of an elongation of the trapping time within the undepleted region. Assuming intrinsic silicon ~300 ns is the recombination time.

The influence of the variation of trapping time to the tail shape is clearly observable. And with deceasing recombination time the tail vanishes.

For both models a full simulation comprising the generation of experiment like data is performed. About 1000 events are generated using the random distributed charge creation according to the Bichsel straggling. The data file is merged with real pedestal data and then analysed. The clear shape as it was obtained in the one event simulation is now smeared by the uncertainty in finding the beginning of a row. By misinterpretation the beginning of a street can be found one pixel too early or too late.

Figure 83 displays the result of this entire simulation process in comparison with the experimental data (dashed line). In figure 83 the tail is generated using the rest electric field hypothesis

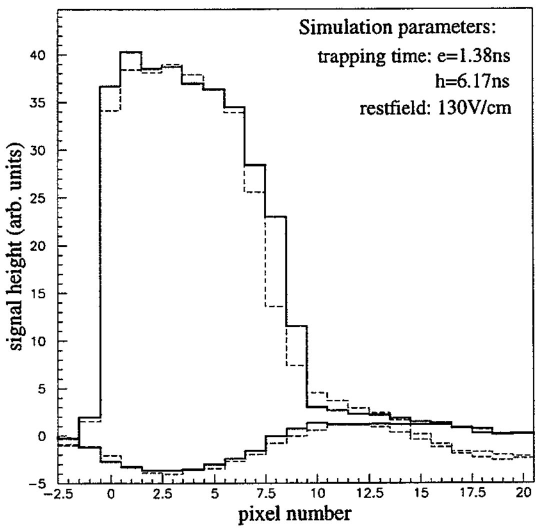

Figure 83: Simulated street shape (solid line) after the entire simulation process. About 1000 simulated events using a random charge generation along the particle track contribute to this figure.

with a voltage drop of 1.5 V over the 150 μm deep undepleted region. This corresponds to an electric field of 100 V/cm. Although not predicted, this measure is not in contradiction with the theory of irradiated semiconductors and is an accepted fact in the community [75].

It is uncertain if an explanation for the hypothesis of a reduced trapping time can be found but this phenomenon is also reported by groups investigating diamond as application for position sensitive sensors [76]. Figure 84 represents the entire simulation process performed with a changed trapping time in the undepleted region. Here, the mean lifetimes considered for electrons and holes are elongated by a factor of 50. The tail on the main pixel street as the negative swing on the

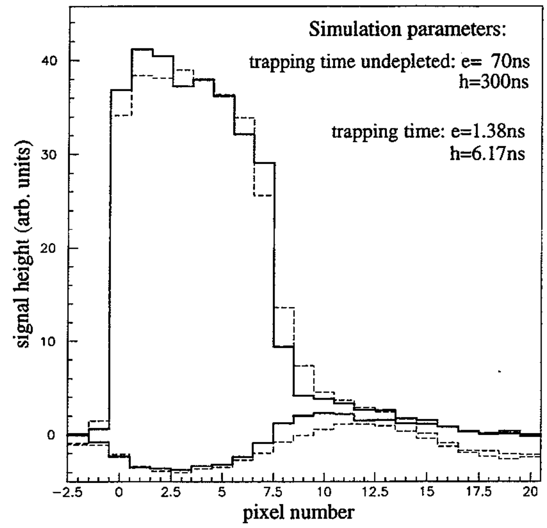

Figure 84: Street shape obtained with an elongation of the trapping times for electrons and holes. This trapping is valid within the depletion region and increases the carrier life time by a factor of 50.

neighbours are reproduced well. A slight deviance is observed when it swings back.

Explanations which trigger the effects are missing, but the simulations show reasonable accordance with the experiment and maybe it is a combination of both. Only the negative swing at the very end of the experimental data is insufficiently reproduced in both cases.

For both simulated models a suitable explanation has to be found. In any case the consequences for a silicon detector operated under LHC conditions are negligible because of the fast readout (shaping time 30 ns). Here only charge is observed which origins from within the depleted region. The charge which is generated within the undepleted region only contributes to the leakage current.

The only expected difficulties arise from charge trapping which reduces the signal by induction. Immediately after irradiation this reduction corresponds on the neighbour pixel to $\sim$1000 electrons. Because of the readout threshold this can suppress charge sharing and reduce the spatial resolution.

8.2 The Lorentz effect in high magnetic and electric fields

For the simulation of the experiment where the Lorenz effect is studied high statistics is inevitable. A plot such as presented in figure 63 is obtained by integrating over a few thousand events. In the experiment the particle impact coordinates are randomly distributed. Sorting these coordinates into the corresponding bins the typical appearance is obtained. The simulated events have to be treated in an equivalent manner and therefore the impact coordinates are stored for each event.

This data is used to create a special file where the data format in accordance with the telescope predicted impact coordinates. In the experiment, this information is stored in a dedicated file where event number, x- and y-coordinate are quoted.

Equation 3.31 is used to calculate a charge carrier velocity dependent drift. In the fixed time scale which is used in the numerical simulation these velocities are transferred into movements.

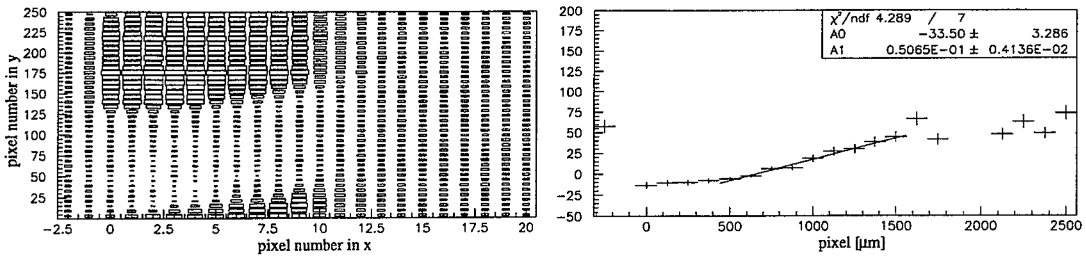

Figure 85: The Lorentz effect measured on an irradiated sensor (copy from figure 65). Left: box histogram created with the telescope data. Right: slope of the charge chairing according to equation (6.11).

In section 7.7 the concept was shown how this experimental observation can be explained and how it is approached by the simulation. Figure 85 shows again the experimental data as displayed in figure 65.

The slope starts relatively flat, and shows a bend from the sixth pixel on. This is interpreted to be caused by deformations of the electric field lines towards the pixel implants. This can be simulated by disabling the Lorentz force from a certain depth below the surface.

The approach to reproduce this behaviour is shown in figure 86. It was calculated using a Lorentz angle of 26.8° which is near the expected value of 26.3° with 1650 $cm^2/(Vs)$ as Hall mobility for electrons. According to the sensor used for the Lorentz measurement (initial fluence of $6.3\times10^{14}/cm^2$ and annealed over 500 days at 2°C) a depletion depth of 170 μm was used. The grazing angle of 5.9° was obtained from the telescope projection.

On the left again the box diagram is shown and the right plot is achieved employing equation (6.11). Although a slight negative slope is visible on the first six pixels in on the right of figure 86 the approximation reproduces the observed effects fairly well.

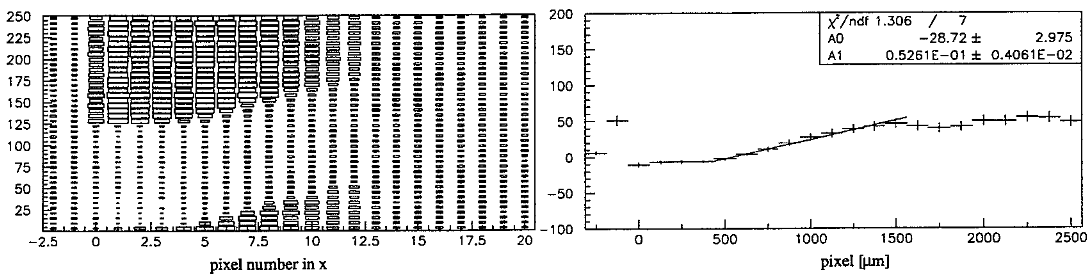

Figure 86: Simulation of the experimental data measuring the Lorentz effect. Here, the approximation from figure 75 is involved in the calculation.

If figure 75 is employed again it can be found that the difference between the experimental observation and the simulation is caused by the simplification of the model. The regions of small electric fields are cusps reaching into the sensor. With the broadening of this region towards the pixels the Lorentz force is increasingly suppressed. This is not approximated by the simulation which only distinguishes between regions where the Lorentz force is active and where it is disabled.

A good prove that this effect is caused by the introduction of such a region is given by performing a simulation under the same conditions but without a specific disabling of the magnetic field effect. The result of this simulation is shown in figure 87 using the same manner of presentation as above.

As summarise it can be concluded, that the simulation has contributed in manifold ways to the better understanding of the experimentally observed effects. The models and approximations implemented in the simulation describe the experiment quite well. At the beginning of new approximations was always an observation which did not fit to the simulation. A good example is the negative swing on the neighbour pixels. Initially, the simulation of induced charge effects was not included and the observed behaviour could not be reproduced. By introducing the according

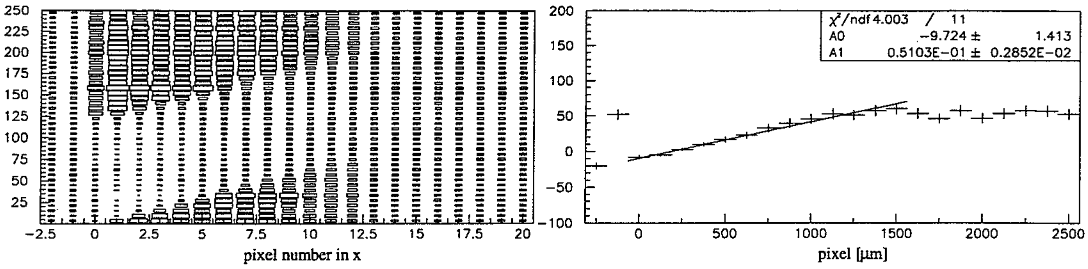

Figure 87: Simulation of the magnetic field effect. Here, within the entire sensor the Lorentz force is enabled.

calculation good agreement is achieved between the experiment and the simulation.

The approximation given in equation 3.28 for the dependence of the trapping times of electrons and holes could be confirmed by the simulation and is within the errors of the fit with the experiment.

A rest electric field within the undepleted region is the most probable candidate to explain the observed tail (figure 76). The simulation could specify the order of magnitude and exclude that it is caused by electric fields higher than 300 V/cm. In addition, a competitive effect was shown which generates a similar fit to the experimental data.

9 CONCLUSION AND OUTLOOK

Silicon, undoubtly belongs to the most investigated materials in the world. Its diverse area of electrical and medical applications makes silicon indispensable. Nevertheless not all its phenomenons and behaviours are completely resolved. In particular mechanisms that come along with radiation induced damage remain on the list of further investigations. But already without an suitable model most of the dependence of radiation induced damage can be explained. For application in high energy physics experiments pragmatic recipes for long term operation have to be found.

This work is an additional contribution to the better understanding of silicon as a position sensitive detector for ionising radiation.

As main result it can be stated that silicon is able to meet the demands as sensor material for the CMS-pixel detector at LHC. Gallium arsenide has shown to be quite susceptible to charged hadrons, resulting in a significant and unacceptable signal loss [76]. Diamond was shown to be resistant to at least 10^{15} pions/cm^2. Up to 250 μm charge collection depth has been reached [77] and further improvements can be expected. Therefore diamond might become a candidate again at later time, provided it can be mass produced at affordable price. Therefore silicon has proved to be a viable detector and has been chosen as baseline sensor material.

In particular the main results will be summarised:
A larger depletion depth than anticipated at the time of the Technical Proposal [14] was found at acceptable bias voltages. This has allowed the pixel size to be increased from (125 μm)^2 to (150 μm)^2.

The average leakage current per (125 μm)^2 pixel is determined at a temperature of -5 °. For a fluence of 6×10^{14}/cm^2 and -300 V it was measured to be 11 nA (20 days after irradiation) which is well below the limit of the 100 nA which the analog readout block is able to consume [15].

Measurements on the different sensors have shown that the charge collection efficiency is strongly design dependent. Small pixel implants (25×25 μm^2) show a reduced signal compared to implants with a width of 75×75 μm^2. This observation is not yet quantitatively established but it motivates to pursue further detailed investigations on this subject.

The signal charge for perpendicular tracks, as obtained from a comparison with preirradiation data was measured to be roughly 10 000 electrons (20 days after irradiation). In order to profit from analog interpolation, the readout should have a hit threshold not larger than 2000-3000 electrons [15].

The decision to run the detector partial depleted at moderate bias voltage in order to accept a reduced charge signal has many advantages in terms of price reduction. High voltage secure designs need more process steps in production and are therefore more expensive. On the other hand the bias voltage supply should not be neglected. As quoted before, 11 nA seem to be very small but this changes if a number of 30×10^6 pixels have to be considered, which adds up to $\approx$0.5 A (current which is compensated by the guard ring structures not included). In view of the fact that this power has to bee cooled again it is wise to reduce the applied bias voltage to its smallest limit.

Thereupon the method of grazing angle was valuable for further investigations:
The proportionality between depletion depth and the bias voltage ($\sqrt{V} \sim d$) could be confirmed for irradiated detectors which implies that the effective doping concentration N_{eff} remains constant over the detector volume.

It was observable that charge carrier approach the readout nodes which have proved to originate in the undepleted region. A detailed test beam study has shown that it concerns charge which comes late in time. The numerical simulation has shown that this behaviour is not reproducible if not a rest electric field on the 5% level is assumed in the undepleted region. Which in accordance with reference [60].

The experimentally found shape of the signal street and the neighbour roads, as shown in figure 69 deviates from the unsophisticated expectation. It is mainly produced by trapping effects. This was successfully manifested as the induced signal caused by trapped charge was added to the simulation.

As mentioned before the simulation shared a big contribution to the obtained understanding of the macroscopically observed effects. Approximated values such as trapping times could be confirmed and the order of magnitude for the rest electric field in the undepleted region was determined.

An additional chapter is opened with the Lorentz angle measurement on irradiated silicon. On this measurement is reported in the appendix B. The resolution of the grazing angle method was improved by the use of a high precision beam telescope. This telescope provided a precise impact prediction which was used to measure the angle between the expected and the actual appearance of the charge. With a simple trigonometric relation the Lorentz angle was determined. In case of the unirradiated detector the $tan\Theta_L \sim$ B relation could be confirmed. Using the value for the Hall mobility the electron drift angle is expected to be 24° in a 4 T magnetic field for 144 V and at room temperature.

Technical problems have prevented a similar result on the irradiated detector. If the above relation is still valid this will lead to an angle of 34° in a 4 T magnetic field at 0°C with an applied bias voltage of 256 V. The comparison of these two results (for the irradiated and the unirradiated sensor) by scaling the different temperatures and bias voltages has failed. There are hints that the Lorentz effect is much more sensitive on the strength and on the distribution of the electric field than expected. Generally, it can be stated that the Lorentz angle (like the mobility) is no longer a constant parameter at high electric fields. An other observation has led to the simulation confirmed assumption of the existence of undepleted cusps between the pixels which suppress a Lorentz drift near the surface.

As an outlook promising results were presented by the RD48-Collaboration reporting on improved radiation hardness with oxygen enriched silicon detectors which can be rated as a significant progress. If the results presented by the collaboration can be confirmed this will delay type inversion and reduce the bias voltage needed to fully deplete the sensors!

A MOTHER BOARD ELECTRONICS LAYOUT

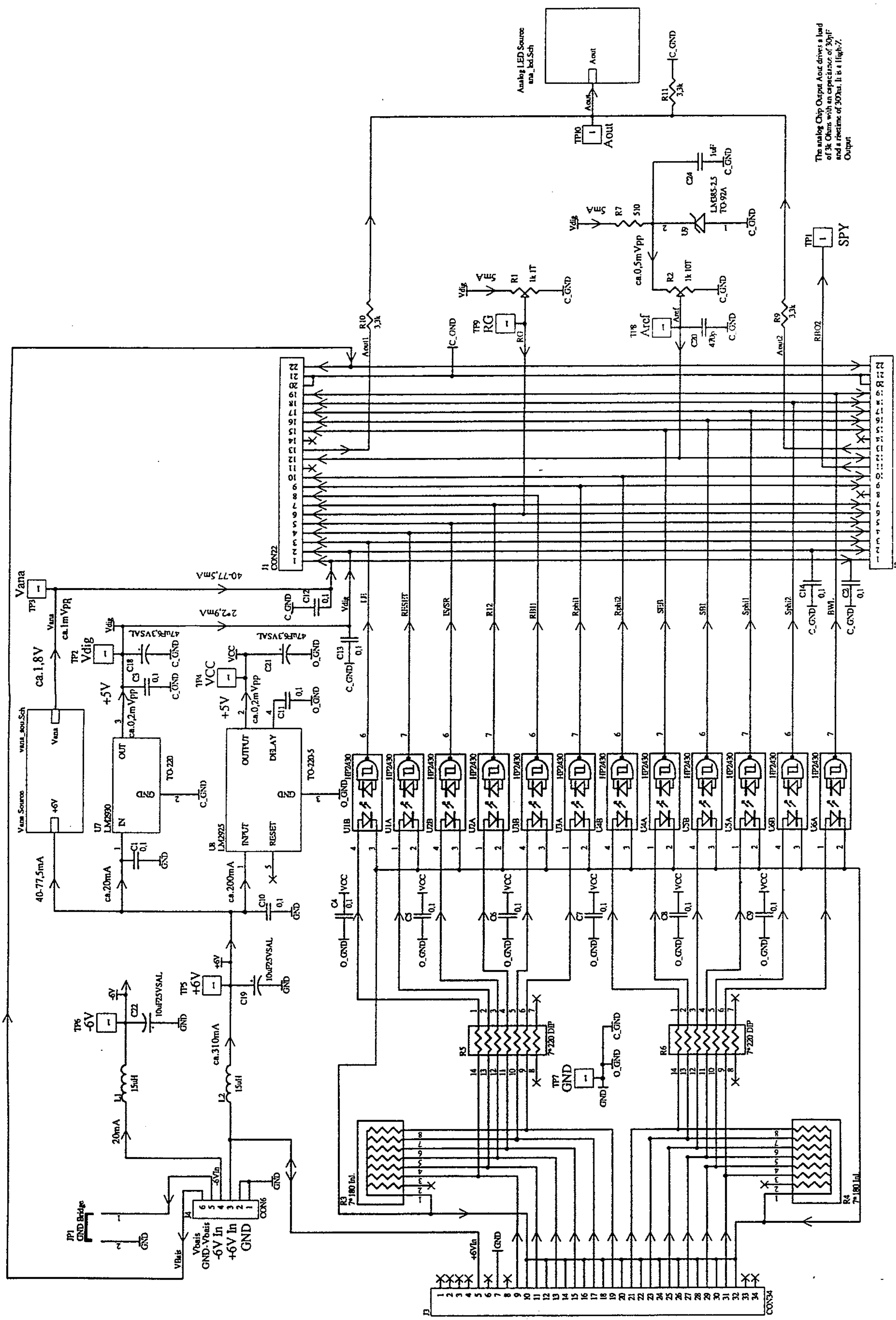

Figure 88: Layout of the motherboard electronics. This PCB board was designed from the Uni Basel electronics group.

B LORENTZ-ANGLE MEASUREMENT IN IRRADIATED SILICON

LORENTZ-ANGLE MEASUREMENT IN IRRADIATED SILICON

B. Henrich*

Institut für Physik der Universität Basel, CH-4056 Basel

R. Kaufmann†

Physik Institut der Universität Zürich-Irchel, CH-8057 Zürich

on behalf of a collaboration between the Universities of Zürich and Basel
and the Paul Scherrer Institute, Villigen, Switzerland

Abstract

The very high magnetic field in modern high energy physics experiments can be used to improve the spatcial resolution of large pitch silicon tracking detectors by ensuring charge sharing between neighbouring strips or pixels. For the reconstruction of the passing particle's track the influence of the magnetic field on the drifting charge carriers must be known. One of the parameters is the Lorentz-angle which describes the change of the drift direction with respect to the electric field. But the drift properties are also affected by radiation induced damages. Therefore Lorentz-angle studies have been performed in silicon before and after irradiation with $6 \cdot 10^{14}$ pions. The devices under test were pixel detectors with square n-type pixels. The measurements have been made using minimal ionising particles and a high precision tracking telescope. The method is based on particles traversing rows of pixels at a grazing angle of 8° (grazing angle method). A detailed analysis of the Lorentz-angle at different magnetic fields is presented and radiation induced effects are discussed.

*beat.henrich@cern.ch

†rolf.kaufmann@cern.ch

1 Introduction

Semiconductor tracking detectors consist of a reversed biassed, fully depleted p-n junction. One of the implants (p or n) is highly segmented in strips or pixels. A passing charged particle creates electron-hole pairs which are drifting in the electric field to the corresponding electrode. This drift is affected by the presence of a magnetic field as well as by irradiation damages. The harsh radiation environment changes some important parameters of the silicon sensor. In order to understand these changes various irradiation studies have been made in the past and will be the subject of forthcoming investigations. The high magnetic field will mainly influence the spatial resolution of the sensor, since a Lorentz-force will be exerted on the drifting charge carriers. Both conditions are given in the new high energy physics experiments at LHC[1].

2 The Lorentz Effect

Due to the electric field the charge carriers produced along the track of a traversing particle drift to the corresponding node. A magnetic field not parallel to the electric field will cause a Lorentz force and hence the charge carriers will not drift along the electric field anymore. This Lorentz effect distributes the charge carriers to several strips or pixels. The charge sharing can be used to calculate the centre of gravity of the charge distribution which improves the traversing particle's track information.

Consider a charged particle drifting in constant electric and magnetic fields. The resulting force on the particle is

$$\vec{F} = \mp q \cdot (\vec{E} + \frac{\vec{v}}{c} \times \vec{B}) \tag{1}$$

where $\vec{B}$ is the magnetic field and $\vec{E}$ the electric field. If the scattering relaxation time τ ($\approx$ the average time between two phonon- or impurity-scatterings) is long enough the particle will perform a circular motion (cyclotron motion) with $\omega_c = e\,B/m^*$, where m^* denotes the effective particle mass (condition $\omega_c \tau \gg 1$). However, if $\omega_c \tau \ll 1$ the particle "forgets" its history with each collision and will perform a random walk with an averaged net velocity in the direction of $\vec{F}$. If $\vec{B}$ is perpendicular to $\vec{E}$ the carriers drift at an angle Θ_L (Lorentz angle) with respect to the direction of the electric field

$$\tan(\Theta_L) = \mu_H \cdot |\vec{B}| \quad . \tag{2}$$

The Hall mobility μ_H is related to the drift mobility via

$$\mu_H = r_H \cdot \mu \tag{3}$$

where r_H is of the order of unity[2]. The factor r_H represents the influence of the magnetic field on the scattering relaxation time τ.

[1] CMS plans to have a magnetic field of 4 Tesla and ATLAS will have 1.45 Tesla

[2] r_H is also related to the Hall coefficient R_H used for the Hall effect: $R_H = r_H/(n\,e)$, where n is the density of carriers (Hall voltage $V_H^y = R_H I_x B_z/d$).

The Hall factor r_H normally depends on the carrier's energy states and on the scattering mechanisms involved. There are some models for analytical calculations (see e. g. [1]), but in most applications r_H has to be measured or evaluated numerically with Monte Carlo techniques. Some values for r_H for different temperatures and doping concentrations are given in [2]. For electrons in n-type silicon ($N_d = 1.75 \cdot 10^{14}\,\mathrm{cm}^{-3}$) and holes in p-type silicon ($N_a = 3.1 \cdot 10^{14}\,\mathrm{cm}^{-3}$) it is stated that

$$r_H^n = 1.15 \quad \text{and} \quad r_H^p = 0.72 \quad . \tag{4}$$

3 Irradiation Effects

In highly irradiated silicon detectors the drift properties are affected by radiation induced lattice displacements. In particular they are influenced by the change of the effective doping, by the increased depletion voltage and by trapping effects.

The change of the effective doping concentration under irradiation $N_{\text{eff}}(\Phi)$ with the flux Φ was subject to many investigations and is understood quite well. A summary and a description of the important parameters can be found in [6]. A key result is that after type inversion has occurred the effective doping concentration increases linearly with the flux.

Due to the increased doping concentration after type inversion a higher reverse bias voltage is needed in order to maintain a reasonable depletion depth. The resulting high electric field reduces the mobility such that

$$\mu = \frac{\mu_0}{\left(1 + \left(\frac{E}{E_c}\right)^\beta\right)^{1/\beta}} \tag{5}$$

where μ_0 is the mobility at low electric fields; E_c is a normalisation parameter depending on the material and $\beta = 1$ is employed for holes and $\beta = 2$ for electrons [3]. However, these results can not be easily adapted to the the Hall mobility, e. g. it is well known that the dependence of the Hall mobility on the electric field decreases with increasing magnetic field strength. Moreover, the magnitudes of the high field effects depend on the orientation of the fields with respect to the crystal lattice. In [4] and in the references quoted therein some theoretical considerations about the Hall mobility are made. Measurements and numerical calculations dealing with these subjects can be found in [5].

Trapping effects lead to a decrease of the number of charge carriers. But from the electrical point of view trapped charge remains active. Since the preamplifiers are charge sensitive, they are also sensitive on image charge induced by trapped carriers.

Due to the electron accumulation layer on the n-side of the detector the electric field lines between two strips or pixels are repelled from the surface after irradiation. Depending on the design this can lead to a shallow undepleted region.

4 Experimental Principle

In order to avoid a measurement of the Lorentz-angle depending on cluster-formation or an underlying charge carrier dependent model a method was chosen which determines the angle only using trigonometric relations. This grazing angle method [7] was developed at the Paul Scherrer Institute in order to determine the depletion depth profile of irradiated silicon pixel detectors alternatively to the commonly used C-V measurement.

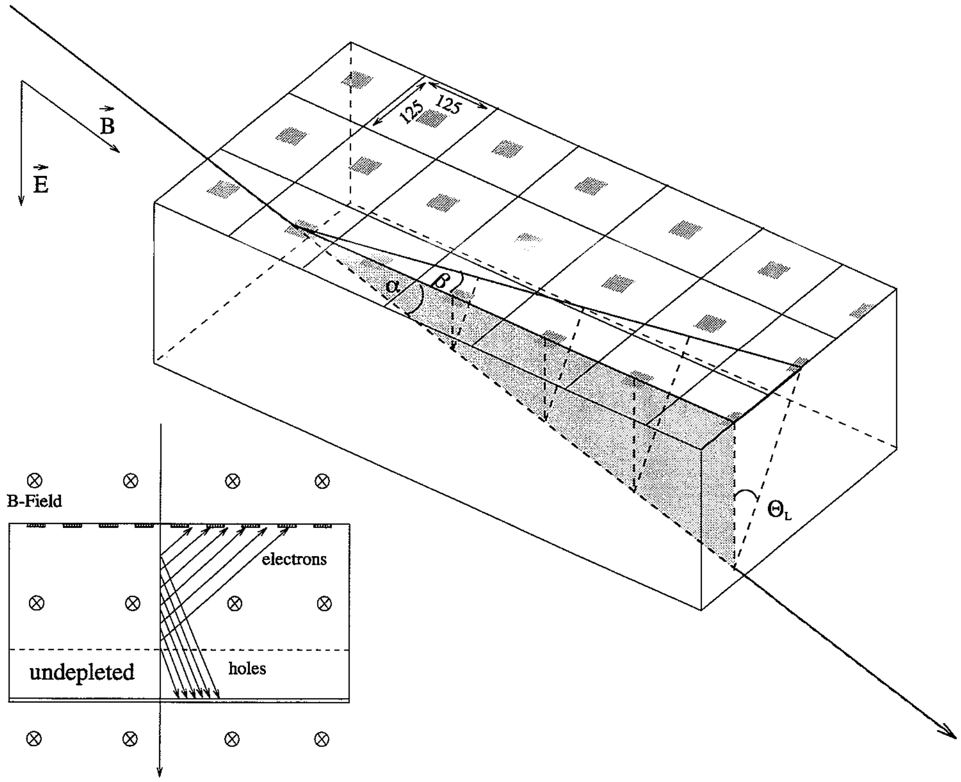

Figure 1: The upper figure shows a three-dimensional section of the pixel detector with a traversing particle. α is the grazing angle and β parametrises the mean arrival position of the electron cloud. Knowing these two angles the Lorentz-angle Θ_L can be calculated. The front view of the detector below shows the drift directions of electrons and holes from different depths of the initial track.

The principle is shown in figure 1. Ionising particles, traversing the detector under a very shallow angle, generate signals which can be seen on a chain of pixels forming a 'signal-street'. Each pixel in the chain collects charge from a given segment of the traversing particle's trajectory and hence from a given depth segment in the bulk. The signal ends at the pixel row under which the particle leaves the detector or enters the undepleted region. The latter is more probable for the irradiated case when the full depletion voltage would exceed the breakdown voltage.

If a magnetic field perpendicular to the electric field is present the drifting charge carriers are deflected by the Lorentz-force. They reach the surface with a displacement proportional to their drift-length. Therefore it is expected that pixels near the end of the chain will loose some charge to the adjacent pixel rows. From the angle of incidence of the traversing particle (α in figure 1) and form the deflection distance y = depth $\cdot \tan\Theta_L$ it is possible to obtain the Lorentz-angle directly. Due to the linear dependence of y on the charge creation depth y can be parametrised by a single angle (β[3] in figure 1). This leads to the simple equation

$$\tan\Theta_L = \frac{\tan\beta}{\tan\alpha} \quad . \tag{6}$$

5 Experimental Setup

For the measurements mentioned above two silicon pixel detectors were available. They consisted of 256 n-type pixels (8 rows à 32 pixels) in a 280 μm thick low resistive n-type bulk. The pixel dimensions were 125 μm×125 μm, isolated with a 8 μm thick p-stop ring. The full depletion voltage was measured to be -123 V, the bias voltage applied for the measurements was -144 V. A more detailed description of the devices can be found in [8]. For the readout the 256 pixels were routed with metal connections to wire bond pads. The readout was done with two APC-128 analogue readout chips [9].

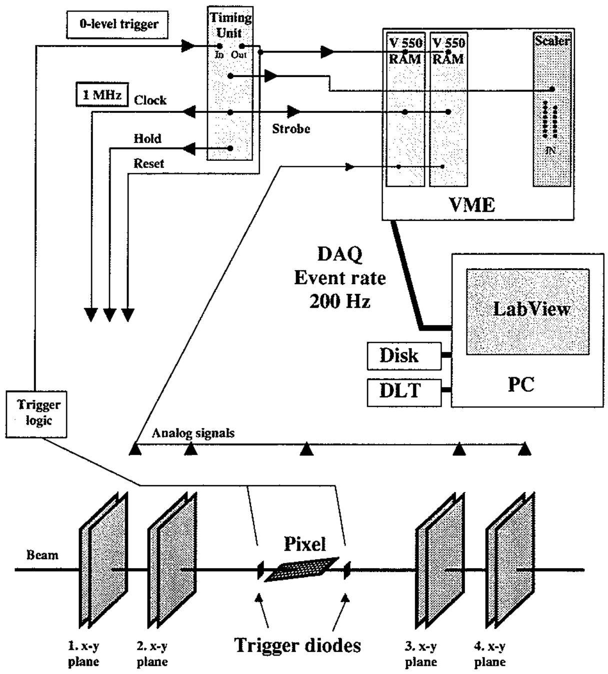

Figure 2: The setup of the beam-test with the pixel detector in the middle of the four x-y planes of the telescope. The overall length was about 60 cm.

One of the detectors was then irradiated with $6 \cdot 10^{14}$ pions per cm^2 and annealed for more than a year in a cooled environment (+ 2° C). This device was also kept cool during

[3]this is not the same parameter as used in equation 5

the measurements. After the irradiation the n-bulk material had converted to p-type which means that the depletion zone was growing from the n-pixel side. Therefore, this detector was still operational after irradiation even when it was only partially depleted. The bias voltage applied was -256 V which led to a depletion zone of 160 μm [10]. The full depletion voltage was around 800 V (calculated).

In order to obtain information about the track positions a beam telescope built by the University of Zürich was used. Four layers consisting of two crossed silicon strip detectors each led to a spatial resolution of less than 1 μm. The strip detectors (32×32 mm^2 of size) had a 50 μm readout pitch. For the readout VA2 chips were used with a shaping time of 2.3 μs. More details about this telescope can be found in [10].

For the grazing angle measurement the pixel detectors were tilted by 8° with respect to the horizontal beam axis. As a trigger two silicon diodes were placed in front of and behind the pixel detectors (see figure 2). A Lab-View controlled VME crate was used for the data acquisition. In order to have good statistics for the alignment the trigger diodes could be switched to logical 'or'. The data taking was done with both in coincidence.

The experiment was performed at the CERN SPS accelerator ring using 225 GeV/c pions. The trigger rate achieved was about 100 Hz. Two superconducting Helmholtz coils provided a longitudinal magnetic field of up to 3 Tesla.

6 Analysis

First the pixel data alone were searched for typical signatures of pixel-streets which were then used to align the pixel detector relatively to the telescope. In a third step the telescope impact information was taken into account and finally the angle β was extracted.

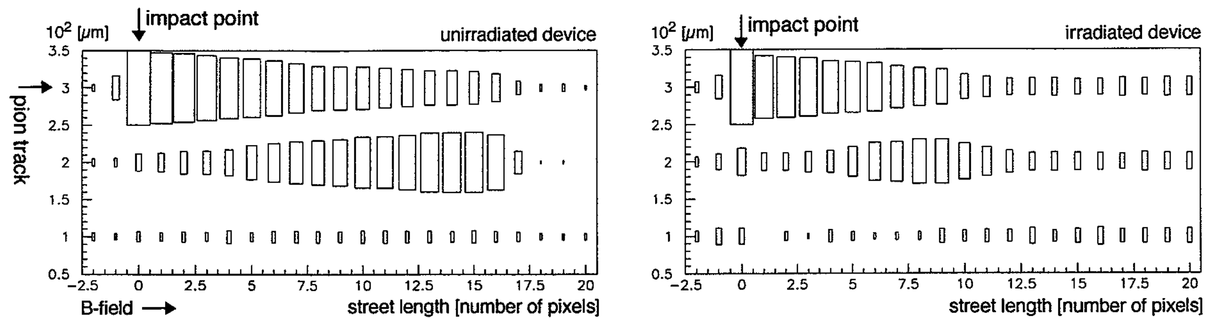

Figure 3: Left: accumulated street signals in the unirradiated detector, one pixel per bin, impact point on the left, magnetic charge deflection downwards; right: the same plot generated with data from the irradiated detector.

Figure 3 shows the pixel-streets. Here a few hundred events were superimposed and aligned according to their impact pixel. The impact point is located on the left. The B-

field vector pointed from left to right, which led to a downward deflection. The pixels on the right of the signal street had the longest drift-path and hence the biggest deflection.

Figure 4 shows the same data as figure 3 but with a finer binning for the impact point. The horizontal axis is the same as in figure 3 whereas the vertical axis only covers two pixels (in units of μm).

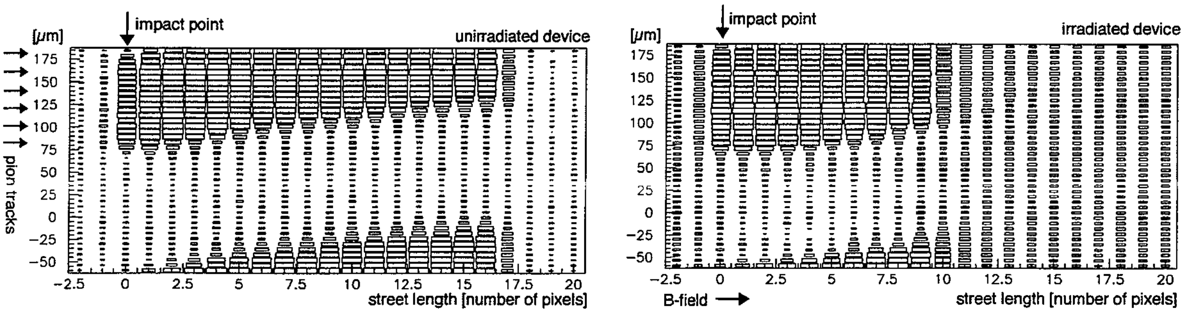

Figure 4: The same picture as in figure 3 but with the telescope impact information included; left: unirradiated detector (V_{bias}=-144V, T=20°,B=3T); right: irradiated detector ($V_{bias} = -256$V, T=-3° C, B=3T).

For the analysis only equation 6 was used. The angle of incidence of the traversing particle (α) was measured using the projection of the pixel detector onto the telescope detector plane. All the telescope entries which had a corresponding pixel entry had been recorded. Knowing the physical dimension of the pixel detector the angle α could be obtained from the the telescope information. Afterwards the angle α was cross-checked with a vertical laser beam reflected from the surface of the pixel detector. The result for α was $(7.63\pm0.03)^\circ$ in the unirradiated case and $(5.93\pm0.07)^\circ$ in the irradiated one.

For the angle β the charge distribution asymmetry

$$A = \frac{Q_n - Q_i}{Q_n + Q_i} \quad \in [-1, 1] \tag{7}$$

was calculated for each pixel of a signal street, where Q_i stands for the charge collected by pixels of the impact pixel street and Q_n for the charge deflected to its neighbour. For $A = -1$ all charge carriers drifted parallel to the $\vec{E}$-field and were collected by the impact pixel row. A value $A = +1$ corresponds to the case where all charge carriers were collected by the neighbouring pixel. Therefore, the interval $A = [-1, 1]$ corresponds to a full pixel pitch of 125 μm. In figure 5 the values for the +3 T data are plotted versus the street length for the unirradiated and the irradiated detector. The angle β of equation 6 was obtained by fitting a straight line to the data. In order to decrease the systematic error the values of β at symmetric $\vec{B}$ fields ±2 T and ±3 T were averaged in the unirradiated case. Due to technical problems only data for +3 T were available for the irradiated device.

Figures 4 and 5 show that for the unirradiated device the charge sharing is almost linear as a function of street length (which in turn is proportional to the depth of the released charge carriers). The results are given in table 1. However, the situation seems

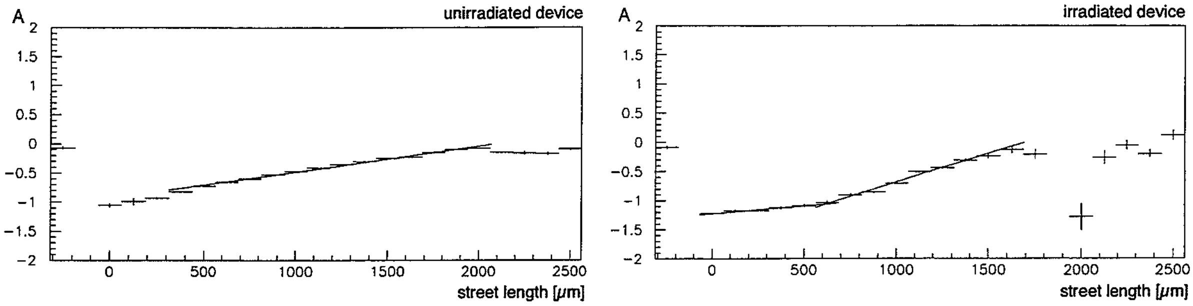

Figure 5: Charge asymmetry A along a pixel street according to equation 7.

more complex in the case of the irradiated device, since the first part of the pixel street indicates a reduced charge sharing compared to the second and therefore deeper part of the track segment. This different behaviour must be attributed to the changes in the device that occur after type inversion, where the effective doping N_{eff} increases and other effects like charge trapping arise. The change of N_{eff} together with a limited bias voltage may also lead to low field regions close to the surface between pixels and therefore modify the detailed charge sharing pattern due to the Lorentz-effect. Less distinctly, such effects may already have been present in the unirradiated sample. This is why the first three data points in figure 5 were not used for the fit.

For the analysis of the irradiated device we have used two straight line fits (figure 5 right) leading to two extreme values for the Lorentz-angle. In table 1 the results are shown. They refer to the conditions prevailing during the run.

unirradiated device	
B-field	Θ_L
2 T	$(12.8 \pm 1.3)^\circ$
3 T	$(18.2 \pm 1.2)^\circ$
($T=20^\circ C$, $V_{\text{bias}}=-144$ V)	

irradiated device	
B-field	Θ_L
3 T	$(6.2 \pm 3.0)^\circ \leq \Theta_L \leq (26.8 \pm 3.6)^\circ$
($T=-3^\circ C$, $V_{\text{bias}}=-256$ V)	

Table 1: Left: Lorentz-angle values for the unirradiated detector for different magnetic fields, right: angles measured in the irradiated device.

7 Discussion

The values for the unirradiated silicon are in good agreement with previous measurements [10]. Moreover, the results for 2 and 3 Tesla are consistent with the $\vec{B}$-field dependence of equation 2.

The interpretation of the situation in the irradiated case is more complex. It can be stated that the charge sharing pattern is not uniform over the depth of the device. The result quoted in table 1 shows a rather large range that is due to the simplified straight line assumption in our analysis. The detailed understanding of this behaviour after irradiation will be the subject of further investigations. Our current understanding is that the reduced Hall mobility in the high $\vec{E}$-field regions of the detector do not sufficiently explain the observed experimental behaviour. Simulations should help to separate the contributions that could not be resolved in this measurements. Therefore a Monte Carlo simulation of the signal formation is under way. It will include time resolved signal formation on the sensing electrodes, trapping effects for electrons and holes as well as undepleted regions.

However, it should be mentioned that in a measurement this behaviour remains concealed if the detector is not probed for various depth segments of the bulk. Hence, the grazing angle method, which acts like a "three dimensional light spot measurement", is an ideal tool for such studies.

The temperatures and bias voltages during the measurement were not the same for the unirradiated and the irradiated device. It is expected that the Lorentz-angle changes with changing conditions. The comparison of the two results would therefore require a correct scaling for the different temperatures and the bias conditions. However, it is important to note that the measurements for the irradiated device have been done under conditions similar to that encountered by the CMS pixel detector at the LHC machine.

Acknowledgement

This work is supported by the Swiss National Science Foundation.

References

[1] K. Seeger, Semiconductor Physics; Springer, Wien 1973

[2] Landolt-Börnstein, Numerical Data and Functional Relationships in Science and Technology, Group III Vol. 17a, Springer, Berlin 1982

[3] D.M. Caughey et al., Proc. IEEE 55(1967)2192

[4] H. Baltes et al., Magnetic Sensors, in: S. M. Sze, Semiconductor Sensors, John Wiley & Sons, New York 1994

[5] M. Kriechbaum et al., J. Phys. Chem. Solids, 33(1972)829

[6] ROSE CERN RD48 Collaboration, 2nd Status Report, 1998, http://www.brunel.ac.uk/research/ROSE

[7] B. Henrich et al., CMS-NOTE/1997-021 http://cmsdoc.cern.ch/tn/all97.html#NOTE1997021

[8] B. Henrich, PhD Thesis; University of Basel (1999); in preparation

[9] R. Horisberger, D. Pitzl, Nucl.Inst.Meth.A 326(1993)92

[10] M. Glättli, Diploma Thesis; University of Zürich, September 1998; paper in preparation

References

[1] Rheinisch Westfählische Technische Hochschule Aachen: K. Lübelsmeyer et al., Investigation of the radiation damage of GaAs detectors by protons, pions and neutrons, *Nucl.Inst.Meth.A*,390(1997)33

[2] Institut für Hochenergiephysik Wien: W. Adam et al., Diamond particle detectors, Preprint *HEPHY-PUB*, 674-97

[3] F. Abe et al. *Phys.Rev.Lett*,73(1994)225
F. Abe et al. *Phys.Rev.D*,50(1994)2966

[4] S. Weinberg, *Rev. Mod. Phys.*,52(1980)515
A. Salam, *Rev.Mod.Phys.*,52(1980)525
S.L. Glashow, *Rev.Mod.Phys.*,52(1980)539

[5] P.W. Anderson, *Phys.Rev.*,130(1963)439

[6] P.W. Higgs, *Phys.Lett.*,12(1964)132
G.S. Guralnik et al., *Phys.Rev.Lett.*,13(1964)585
F. Englest and R. Bront, *Phys.Rev.*,13(1964)321

[7] R. Akers et al., *Phys.Lett.B*,327(1994)397

[8] Large Hadron Collider in the LEP tunnel, Proc. of the ECFA-CERN Workshop, Lausanne, 1984, *CERN*,84-10(1984)

[9] *Proceedings of the general meeting on LHC physics and detectors*, Evian, 5-8 March 1992

[10] B. Hayms et al., *Nuc.Inst.Meth.*,205(1983)99

[11] C.J.S. Damerell et al.,*Nucl.Instr.Meth.A*,253(1987)478

[12] G.D. Agnew et al.,SLAC-400(1992)397

[13] RD 20 status report. *CERN* DRDC/94-39(1994)

[14] The Compact Muon Solenoid, technical proposal, *CERN/LHC*,94-38,1994

[15] The tracker project, technical design report, *CERN/LHCC*98-6, CMS-TDR 5, 1998

[16] CERN Courier, International Journal of High-Energy Physics, Vol.39,Num.2, march 1999

[17] Particle Data Group: Review of Particle Physics
Europ.Phys.Jur.C,3(1998)157

[18] J. Kemmer, Fabrication of low noise silicon radiation detectors by planar process, *Nicl.Inst.Meth.*,196(1980)499

[19] S.M.Sze, Semiconductor devices, physics and technologies, *John Wiley & Sons*,1985

[20] A.S.Grove, Physics and technology of semiconductor devices, *John Wiley & Sons*,1967

[21] Landolt-Börnstein: Numerical Data and Functional Relationships in Science and Technology, Group III Vol. 17a, Springer, Berlin 1982

[22] Handbook on Semiconductors, Volume 1 Band Theory and Transport Properties, W. Paul (Ed.), North-Holland, Amsterdam 1982
- Laura M. Roth: Dynamics of Electrons in Semiconductors in Electric and Magnetic Fields
- E. Conwell: Transport: The Boltzmann Equation
- A.C. Smith: Transport Using the Particle Kinetic Model
- D.K. Ferry: Fundamental Aspects of Hot Electron Phenomena

[23] A. Castoldi et al.: Performance of Silicon Drift Detectors in a Magnetic Field, *Nucl.Inst.Meth.A*,399(1997)227

[24] R.E. Robson et al.: Electron Transport Theory in Gases: Must it be so Difficult?; *Nucl.Inst.Meth.A*,394(1997)74

[25] D.M. Caughey et al.: Carrier Mobilities in Silicon Empirically Related to Doping and Field; *Proc.IEEE*,55(1967)2192

[26] K. Kleiknecht, Detektoren für Teilchenstrahlung Teubner Verlag

[27] W.R.Th. Ten Kate, The influence of the strip width on the performance of a strip detector, *Nucl.Inst.Meth.A*,253(1987)333

[28] R.N. Hall, Electron-hole recombination in Germanium, *Phys.Rev*,87(1952)387
W. Shockley and W.T. Read, Statistics of the recombination of holes and electrones, *phys.Rev.*,87(1952)835

[29] P. Riedler, Radiation damage effects and performance of silicon strip detectors using LHC readout electronics, *PhD Thesis*, CERN, 1998

[30] R. Wunstorf et al.,Damage-induced surface effects in silicon detectors, *Nulcl.Inst.Meth.A* 377(1996)290

[31] G. Hall et al., A microscopic explanation for type inversion and the annealing behaviour of radiation damaged silicon detectors, RD20/TN/95/4

[32] S. Watts, DLTS studies of defect production in various Si substrates, talk held at the 4^{th} Rose Workshop, CERN 1998

[33] R. Wunstorf: Systematische Untersuchungen zur Strahlenresistenz von Silizium-Detektoren für die Verwendung in Hochenergiephysik-Experimenten, *PhD Thesis*, DESY FH1K-92-01

[34] E. Freturst et al., Radiation harrdness of silicon detectors for future colliders, *Nucl.Inst.Meth.A*,326(1993)326

[35] E. Fretwurst et al., Silicon detector for calorimetry; technology and radiation damage, *Nucl.Inst.Meth.A* 288(1990)1

[36] H.W. Kraner et al., The use of signal current pulse shape to study the internal electric field profile and trapping effects in neutron damaged silicon detectors, *Nucl.Inst.Meth.A* 326(1993)350

[37] S.M. Sze, Physics of semiconductor devices, 2nd ed. *Wiley & Sons*, 1981

[38] A. Ruzin et al., Results of radiation hardness of diodes processed from various silicon materials, talk held at the 4^{th} Rose Workshop, CERN 1998

[39] E. Barberis et al., Temperature effects on radiation damage to silicon detectors, *Nucl.Inst.Meth.A*,326(1993)373

[40] K. Seeger, Semiconductor Physics; Springer, Wien 1973

[41] Wafer submission in collaboration with the Instituto Nazionale di Fisica Nucleare (INFN) Pisa

[42] J. Kemmer et al.,Structures for position sensitive semiconductor devices, *Nucl.Inst.Meth.A*,273(1988)588

[43] Technical report, RD20 collaboration 1994

[44] K. Gill and R. Wheadon, Results from ^{60}Co-gamma irradiations of RD20 n-side test-structures with p-stop isolation, *RD20,TN29*,1994

[45] R. Wheadon, private communication

[46] R. Horisberger, private communication

[47] V. Dubacher, Test of a silicon piuxel detector with 50 GeV/c pions, *Diploma Thesis*, Zürich 1996

[48] R. Horisberger, The bipolar silicon micro strip detector: a proposal for a novel precision tracking device, *Nucl.Inst.Meth.A*,288(1990)87

[49] D. Pitzl et al., Type inversion in silicon detectors, *Nucl.Inst.Meth.A*,311(1992)98

[50] B. Henrich et al.,Depth profile of signal charge collected in heavily irradiated silicon pixels CMS, *CMS NOTE*, 1997-021

[51] H. Niggli, Ladungssammlung in doppelseitigen Silizium-Streifendetektoren für H1, *diploma thesis, ETH-IPP* internal report 94-5

[52] R. Horisberger, D. Pitzl, A novel readout chip for silicon strip detectors with analog pipeline and digitally controlled analog signal processing, *Nucl.Inst.Meth.A*,326(1993)92

[53] R. Horisberger, Design requirements and first results of an LHC adequate analogue block for the CMS pixel detector, *Nucl.Inst.Meth.A*,395(1997)310

[54] M. Lechner, Development of a radiation hard pixel analog block for the CMS vertex detector, *PhD Thesis*, Diss. ETH No.12866, 1998

[55] W. Erdmann et al., Optical analog readout and control of the central silicon vertex detector of H1 at HERA, *Nucl.Inst.Meth.A*,372(1996)188

[56] R. Kaufmann, B. Henrich, Lorentz angle measurement in irradiated silicon, to be published in *Nucl.Inst.Meth*
[57] IDE AS Homepage, http://www.ideas.no/
[58] M. Glättli, Untersuchung von Silizium Pixeldetektoren mit einem Silizium Mikrostreifen Strahlteleskop, *Diploma Thesis*, Zürich 1998
[59] RD2: S.Bates et al, Pion induced damage in silicon detectors, *Nucl.Phys.B*, 44(1995)510
[60] A. Chilingarov et al., The electric field in irradiated silicon detectors, *Nucl.Inst.Meth.A*,418(1998)314
[61] K. Gabathuler, private communication
[62] G. Klaiber, Eigenschaften des analogen Verstärker- und Speicherchips APC128 zur Auslese von Siliziumdetektoren, *Diploma Thesis*, ETHZ-IPP Internal Report 95-5
[63] R. Wunstorf, private communication
[64] H. Feick, Radiation tolerance of silicon particle detectors for high-energy physics experiments, *Phd Thesis*, DESY F35D-97-08
[65] H. Feick, private communication
[66] H. Bichsel, Straggling in thin silicon detectors, *Rew.Mod.Phys.*,Vol. 60, No. 3, July 1988
[67] L. Landau,*J.Phys.(Moscow)*,1944,VIII,201
[68] M. Pindo, Simulating charge collection in silicon pixel detectors, *Nucl.Inst.Meth.A*,395(1997)360
[69] M. Lüscher, A portable high-quality number generator for lattice field theory simulations, *Computer Phys. Commun.*,79(1994)100-110
[70] F. James, RANLUX: A Fortran implementation of the high-quality number generator of Lüscher, *Computer Phys. Commun.*,79(1994)111-114
[71] G. Parker, Introductory semiconductor device physics, *Prentice Hall* 1994
[72] J.D. Jackson, Classical Electrodynamics, *Wiley & Sons*, 1962
[73] W. Erdmann: Untersuchung der Photoproduktion von D^*-Mesonen am ep-Speicherring HERA, Diss ETH No.11441
[74] 4th ROSE Workshop on radiation hardening of silicon detectors, CERN 2-4 December 1998
[75] P. Weilhammer et al.,Recent results on CVD diamond radiation sensors, *Nucl.Inst.Meth.A*,409(1998)264
[76] W.J. Xiao et al., High fluence proton irradiation of GaAs detectors at room temperature and at -8 °C, *Nucl.Phys.B*(Proc. Suppl.),61B(1998)427
W.J. Xiao, Investigation of radiation hardness of SI GaAs detectors for their application in the tracking system at the LHC experiments, *PhD Thesis*, RWTH Aachen (1998)
W. Braunschweig et al., Investigation of the radiation damage of GaAs detectors by neutrons and photons, *Nucl.Inst.Meth.A*,372(1996)111
[77] C. Bauer et al., Recent results from the RD43 diamond detector collaboration, *Nucl.Inst.Meth.A*, 383(1996)64
W. Adam et al. (RD42-Collaboration), Development of diamond tracking detectors for high luminosity experiments at the LHC, *Status Report RD42*, CERN, LHCC 97-3, Jan. 1997

ACKNOWLEDGEMENTS

My introduction into the varied field of particle detector technologies has a long history. Nearly as long as this history is the list of persons which have supported or contributed to this work. In particular I wish to express my appreciation and gratitude to:

- Ludwig Tauscher for his liberal and uncomplicated support which established the basis for the realisation of this work.
- Roland Horisberger for entrusting me with the job of designing and testing a silicon prototype sensor for the CMS experiment. From the very beginning of our relationship he shared his personal enthusiasm in particle physics with me and gave me a competent introduction into the world of silicon sensor techniques.
- Kurt Gabathuler who obligingly offered his help during beam test measurements and data analysis.
- Willi Bertl for his valuable contribution to the trigger logic and the readout setup. He also was always a competent address for FORTRAN and related problems.
- Danek Kotlinski for writing the CPG-CMAMAC compiler which was an often used tool during our beam tests.
- Silvan Streuli, our skilled and inventive technician at PSI who practically supplied all mechanical structures for the grazing angle setup.
- The PSI-group: Christian Brönnimann, Wolfram Erdmann, Johannes Gassner, Michael Hilgers, Stefan Lüders, Beat Meier, Hubert Niggli, Daniel Pitzl and Roger Schnyder for the good times at PSI and elsewhere.
- The whole Basel gang which are Daniel Haas, Pablo Garcia-Abia, Urs Gysin, Fabian Leimgruber, Guido Polivka, Rene Rickenbach, Thomas Schietinger, Torsten Strunz, Sotirios Vlachos and Maneesh Wadhwa. Although they worked on completely different experiments I could benefit from various fruitful discussions and their manifold experiences in computation and data analysis.
- The CERN crew: Peppino Giarritta, Michel Glättli, Christian Regenfus, Petra Riedler and Stefan Spanier for their assistance in the Lorentz angle measurement and analysis.
- Michael Steinacher and Daniel Sacker from the electronics group in Basel deserve to be mentioned because of their work on the motherboard electronics.
- Astrit Kalt and Carmen Bücheli for taking care of all the administrative tasks at the Basel Institute and at PSI, respectively.
- Moritz Lechner who started his thesis at the same time and in the same group at PSI for sharing his knowledge in electronics with me and for his friendship.
- Rolf Kaufmann for the gratifying cooperation at the CERN beam test. The valuable discussions about transport phenomenons in silicon sensors and other subjects have been very welcome.
- Markus Meuwly for carefully reading and correcting the manuscript, drawing my attention to some of the fine subtleties of the English language and for his warm and lasting friendship.

Above all though, I am deeply indebted to my parents for their great support throughout the years. And last but not least I wish to thank my wife Katharina for her love, patience and her willingness to step back for my personal career. Last mentioned but on the top of my concerns my daughters Sirkka and Mirja.

CURRICULUM VITAE

Beat Horst Henrich, citizen of **Allschwil, Switzerland**

29 December 1966	born in Basel
30 May 1992	married with Katharina Henrich
	two children: Sirkka (15.11.1993) and Mirja (31.7.1996)
1973-1979	Primarschule Allschwil
1979-1980	Sekundarschule Bettenacker
1980-1984	Realschule Steinen (Germany)
1984-1987	Theodor Heuss Gymnasium Schopfheim (Germany)
1987-1994	Study of physics, mathematics and astronomy at the University of Basel
summer 1990	summer student at the Southern European Observatory (ESO), La Silla, Chile
spring-autumn 1994	sabbatical for daughter Sirkka
autumn 1994	diploma in experimental physics
1994-1999	PhD student in experimental particle physics at the University of Basel, based at the Paul Scherrer Institute (PSI).

The following lecturers have contributed to my academic education: K. Alder, G. Backenstoss, C. Bandle, E. Baumgartner, G. Baur, H. Burkhart, H. Christen, J. Fünfschilling, H.-J. Güntherodt, H. Huber, H. Kraft, P. Oelhafen, H. Rudin, I. Sick, U. Steinlin, P. Talkner, G. A. Tammann, L. Tauscher, H. Thomas, D. Trautmann, C. Trefzger, C. Ullrich, R. Wagner, I. Zschokke.